Université de Montréal

Développement et radiosynthèse de ligands du récepteur tyrosine kinase neurotrophique type 2 (TrkB) marqués aux carbone-11 et fluor-18 pour l'imagerie cérébrale par tomographie d'émission de positons

Par

Vadim Bernard-Gauthier

Département de chimie, Université de Montréal

Faculté des arts et sciences

Mémoire présenté à la Faculté des études supérieures

En vue de l'obtention du grade de

Maître ès sciences (M. Sc.)

En chimie

Août 2013

Université de Montréal

Faculté des études supérieures

Ce mémoire intitulé:

Développement et radiosynthèse de ligands du récepteur tyrosine kinase neurotrophique type 2 (TrkB) marqués aux carbone-11 et fluor-18 pour l'imagerie cérébrale par tomographie d'émission de positons

présenté par :

Vadim Bernard-Gauthier

Travail effectué sous la supervision de :

Prof. Ralf Schirrmacher, directeur de recherche

Prof. Christian Reber, co-directeur

Résumé

Ce mémoire présente mes travaux ayant menés au développement d'une première génération de radioligands marqués au fluor-18 ($t_{1/2}$ = 110 min) et au carbone-11 ($t_{1/2}$ = 20.4 min) destinés à l'imagerie cérébrale *in vivo* du récepteur tyrosine kinase neurotrophique de type 2 (TrkB) en tomographie par émission de positons (TEP). Ces travaux reposent sur l'identification récente de ligands de TrkB non peptidiques à hautes affinités dérivés du 7,8-dihydroxyflavone.

La synthèse d'une série de dérivés du 7,8-dihydroxyflavone non-radioactifs de même que des précuseurs à l'incorporation du fluro-18 et du carbone-11 a d'abord été effectuée. Partant des précurseurs adéquats synthétisés, la radiosynthèse de deux radioligands, l'un marqué au fluor-18 et l'autre au carbone-11, a été développée. Ces radiosynthèses reposent respectivement sur une ^{18}F-radiofluorination nucléophile aromatique nouvelle et hautement efficace et sur une ^{11}C-méthylation *N*-sélective. Les radiotraceurs de TrkB ainsi obtenus ont ensuite été évalués *in vitro* en autoradiographie et *in vivo* en tant que traceurs TEP dans des rats. L'évaluation des propriétés physico-chimique de même que de la stabilité *in vitro* des radiotraceurs sont présentées.

Partant d'une série d'analogues cristallisés de ces flavones synthétiques, une étude de relation structure-activité a été menée. La combinaison de cette étude, de pair avec l'évaluation *in vivo* de la première génération de radiotraceurs de TrkB a aussi permis d'investiguer les pharmacophores nécessaires à l'affinité de ces ligands de même que d'identifier des fragments structurels associés au métabolisme des radiotraceurs. La radiosynthèse d'un troisième radioligand de TrkB et son évaluation TEP *in vivo* de même que la mise en lumière des modifications structurelles utiles au développement d'une seconde génération de radioligands de TrkB avec des propriétés optimisées pour fin d'imagerie TEP sont aussi détaillés.

Mots clés

Imagerie de tomographie par émission de positons, radioligand pour le système nerveux central, radiochimie du fluor-18, radiochimie du carbone-11, récepteur tyrosine kinase neurotrophique type 2, facteur neurotrophique dérivé du cerveau, flavonoïde, 7,8-dihydroxyflavone, ^{18}F-substitution nucléophile aromatique, ^{11}C-méthylation.

Abstract

This thesis describes my contribution leading to the development of the first-generation positron emission tomography (PET) radioligands labeled with fluorine-18 ($t_{1/2}$ = 110 min) or carbon-11 ($t_{1/2}$ = 20.4 min) for the *in vivo* brain imaging of tropomyosin-related kinase B (TrkB). This research follows from the recent discovery of non-peptidic, high-affinity TrkB ligands derived from 7,8-dihydroxyflavone.

The synthesis of non-radioactive 7,8-dihydroxyflavone derivatives and radiolabeling precursors amenable to fluorine-18 and carbon-11 incorporation was performed. Two synthesized compounds have been brought forward as precursors for radiolabeling with either fluorine-18 or carbon-11. Radiosynthesis involved either a novel nucleophilic aromatic subsitution with [^{18}F]fluoride, or *N*-methylation with [^{11}C]methyl iodide or [^{11}C] methyl triflate. The resulting radiotracers were assessed *in vitro* by autoradiography and *in vivo* by PET scans of rats. The physicochemical properties and serum stability of these tracers were also evaluated.

X-ray crystal structures of a series of synthetic flavone analogues were used as basis for structure-activity relationship (SAR) analysis. In combination with the above *in vivo* PET evaluation of these compounds, certain pharmacophores were shown essential for ligand binding affinity. In addition, some structural fragments were associated with *in vivo* ligand metabolism.

The development and radiosynthesis of a third TrkB radiotracer, along with its *in vivo* PET evaluation and structural analysis, is also described here. In all, better understanding of these tracers have led to the design of potential second-generation TrkB ligands with more optimal properties as PET radiotracers.

Keywords

Positron emission tomography imaging, central nervous system radioligand, ^{18}F-radiochemistry, ^{11}C-radiochemistry, tropomyosin-related kinase B receptor, brain-derived neurotrophic factor, flavonoid, 7,8-dihydroxyflavone, nucleophilic aromatic ^{18}F-substitution, ^{11}C-methylation.

Table des matières

Liste des tableaux

Chapitre 1

Chapter 3

Chapter 4

Liste des figures

Chapitre 1

Chapter 2

Chapter 3

Chapter 4

Liste des schémas

Chapitre 1

Chapter 2

Chapter 3

Chapter 4

Listes des abbréviations

β^+	positon
β^-	électron
v	neutrino
5-HT_{1A}	récepteur sérotoninergique sous-type 1A
Aβ	beta-amyloïde
A_S	activité spécifique (massique)
BDNF	facteur neurotrophique dérivé du cerveau
Bn	benzyle
B_{max}	concentration des sites de liaison
Bq	becquerel
Boc	*tert*-butoxycarbonyle
Bz	récepteur benzodiazépine
CCM	chromatographie sur couche mince
CLHP	chromatographie liquide haute performance
Ci	curie
CPG	chromatographie gazeuse
D_2	récepteur dopaminergique sous-type 2
Da	dalton
DBU	1,8-Diazabicycloundec-7-ène
DMF	diméthylformamide
DMSO	diméthylsulfoxide
EtOH	éthanol
eV	électron-volt

f_p	fraction libre
FDG	2-deoxy-2-[^{18}F]fluoro-D-glucose
GEA	groupement électroattracteur
IRM	imagerie par résonance magnétique
K_{222}	Kryptofix® 222
K_d	constante de dissociation
LogP	logarithme du coefficient de partage
Me	méthyle
MeCN	acétonitrile
MEK	butanone
mGluR5	récepteur métabotrope au glutamate type 5
MRC	motif riche en cystéines
MRL	motif riche en leucines
n	neutron
NF	*N*-fluoro
NGF	facteur de croissance du tissu nerveux
NT-3	neurotrophine 3
NT-4	neurotrophine 4
OTf	trifluorométhylsulfonate
PDE4	phosphodiestérase type 4
P-gp	P-glycoprotéine
PLT	potentialisation à long terme
RCY	rendement radiochimique
S_N2	substitution nucléophile aromatique
SNC	système nerveux central

TEP	tomographie par émission de positon
TEMP	tomographie d'émission monophotonique
THF	tétrahydrofurane
TMD	tomodensitométrie
TrkA	récepteur tyrosine kinase neurotrophique type 1
TrkB	récepteur tyrosine kinase neurotrophique type 2
TrkC	récepteur tyrosine kinase neurotrophique type 3

List of abbreviations

β^+	positron
β^-	electron
v	neutrino
Aβ	beta-amyloid
Ac	acetyl
AD	Alzheimer'S disease
aq.	aqueous
Ar	aryl
BBB	blood-brain barrier
BDNF	brain-derived neurotrophic factor
Boc	tert-butoxycarbonyl
Bq	becquerel
br.	broad
BW	body weight
Ci	curie
CGN	cerebellar granule neuron
CHI	chalcone isomerase
CHS	chalcone synthase
CNS	central nervous system
conc.	concentrated
DCM	dichloromethane
DHF	dihydroxyflavone
DMF	dimethylformamide

DMSO	dimethyl sulfoxide
ECD	extracellular domain
EDG	electron-donating group
ERK	extracellular signa-regulated kinase
eV	electron-volt
EWG	electron-withdrawing group
FL	full lenght
FNS	flavoen synthase
h	hour(s)
HD	Hundington's disease
HPLC	High-performance liquid chromatography
HRMS	high resolution mass spectrometry
Hz	hertz
IC_{50}	half maximal inhibitory concentration
J	coupling constant
LG	leaving group
LogD	logaritm of distribution coefficient
LogP	logaritm of partition coefficient
M	molar, mol/L
MAPK	mitogen-activated protein kinase
Me	methyl
MDD	major depressive disorder
PG	protecting group
min	minute(s)
NGF	nerve growth factor

NMR	nuclear magnetic resonance
OTf	trifluorométhylsulfonate
PBS	phosphate buffered saline
PD	Parkinson's disease
PET	positron emission tomography
PI3K	phosphatidylinositide 3-kinases
PLCγ	phospholipase Cγ
Ph	phenyl
Ppm	parts per million
RCY	radiochemical yield
ROI	region of interest
ROS	reactive oxygen species
Rt	room temperature
sat.	saturated
SDS-PAGE	sodium dodecyl sulfate polyacrylamide gel electrophoresis
S_N2	aromatic nucleophilic substitution
SPECT	single-photon emission computed tomography
SUV	Standardized Uptake Value
TAC	time-activity curve
TBI	traumatic brain injury
temp	temperature
THF	tetrahydrofuran
TLC	thin layer chromatography
TMS	tetramethylsilane
TrkA	tropomyosin-related kinase A receptor

TrkB	tropomyosin-related kinase B receptor
TrkC	tropomyosin-related kinase C receptor
xs.	Excess

Remerciements

Je souhaite avant tout remercier mon directeur de recherche, le professeur Ralf Schirrmacher, pour m'avoir offert l'opportunité de joindre son groupe et d'apprendre la radiochimie mais surtout, pour sa confiance et son support constant tout au long de mes travaux. Qui plus est, je souhaite souligner mon appréciation de la grande latitude avec la laquelle j'ai pu développer mes projets sous sa supervision. Je veux de plus remercier mon co-directeur, Christian Reber, pour son assistance et sa disponibilité.

La réalisation de projets de chimie radiopharmaceutique et d'imagerie TEP implique la mise en commun d'un nombre important de ressources matérielles et humaines. En particulier, je souhaite remercier mes collègues du laboratoire du Cyclotron médicale de l'Institut et Hôpital Neurologiques de Montréal, le Dr. Alexey Kosikov, Dean Jolly, Miriam Kovacevic de même que Karen Ross. Aussi, je tiens à remercier Antonio Aliaga et Arturo Aliaga pour leur assistance respectivement pour l'imagerie TEP et l'autoradiographie. Aussi, je suis très reconnaissant envers mon collègue, Joshua Chin, pour les discussions partagées empreintes de sa rigueur scientifique.

Le manuscript présenté dans ce mémoire est le fruit d'une étroite collaboration avec Mehdi Boudjemline, de même qu'avec les professeurs Philip Barker et Alexander Thiel que je tiens à remercier pour leur important apport respectif. Je veux aussi remercier la professeure Esther Schirrmacher pour ses judicieux conseils concernant la radiochimie.

Finalement et sur une note plus personnelle, je souhaite remercier du plus profond du cœur les membres de ma famille pour leur support extraordinaire. En particulier, ma mère qui est à mes yeux un exemple de détermination et de courage et de qui je tiens ma curiosité et persévérance. Je veux aussi remercier la femme merveilleuse avec qui je partage ma vie, Marilyn, qui chaque jour me rend heureux.

Chapitre 1

Introduction

1.1 Imagerie par tomographie d'émission de positons (TEP) et recherche radiopharmaceutique

1.1.1 Principes et instrumentation de l'imagerie par tomographie d'émission de positons

La tomographie par émission de positons (TEP) constitute une technique d'imagerie de médecine nucléaire non-invasive permettant l'évaluation de même que l'analyse quantitative tridimentionnelle de processus biochimiques et physiologiques *in vivo*.[1,2] Cette technologie repose sur la détection de signaux indirects provenant de radiotraceurs exogènes marqués par des radionucléides à courte vie administrés typiquement en concentration picomolaire par voie inhalatoire ou plus communément, de façon intraveineuse. L'obtention de radiotraceurs pour la TEP repose essentiellement sur le développement et l'application de méthodologies de radiosynthèse efficaces répondant aux exigences strictes associées à la manipulation de tels radioisotopes et des molécules auxquelles ils sont greffés.[3] Les radioisotopes émetteurs de positons utilisés en TEP incluent le ^{18}F, le ^{11}C, le ^{13}N, le ^{15}O, le ^{68}Ga et le ^{64}Cu entre autres et sont généralement produit par un cyclotron sur le site même où ils seront incorporés au radiotraceur visé, lequel sera purifié, analysé, formulé et utilisé pour l'imagerie TEP dans un délai restreint de quelques dizaines de minutes dépendemment du radionucléide considéré. Les radiotraceurs ainsi obtenus peuvent s'avérer soit spécifiques à un récepteur protéique, à un tissu ou encore mettre en relief un processus enzymatique donné et offrent ainsi la possibilité d'étudier l'ensemble de ces événements biochimiques au niveau moléculaire.

1.1.1.1 Modalités d'imagerie médicale

A ce titre, la TEP permet l'obtention de données biochimiques uniques et s'inscrit comme une modalité d'imagerie clé parmi l'ensemble des technologies d'imagerie médicale disponible (Figure 1.1).[4] En comparaison, l'échographie (ultrason) ou encore l'imagerie par résonance magnétique (IRM) et la tomodensitométrie (TMD) permettent d'obtenir des informations anatomiques détaillées mais offrent peu ou

aucune information au niveau moléculaire. Ainsi, en dépit de leur résolution spatiale avantageuse (ultrason: 50-500 μm; IRM: 25-100 μm; TMD: 50-200 μm),[5] ces techniques d'imagerie sont souvent limitées à l'évaluation de conditions associées à des anormalités structurelles alors que les approaches d'imagerie nucléaires telles la TEP et

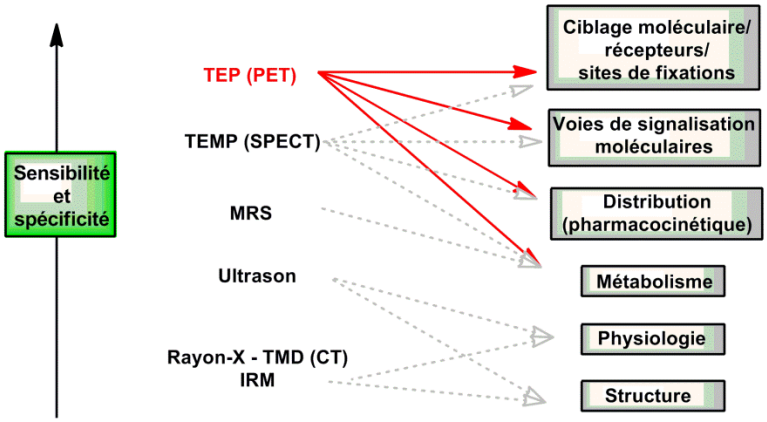

Figure 1.1. Le spectre des techniques d'imagerie médicale et leurs applications. Le spectre couvre une fourchette de sensibilité de 10^9 (millimolaire au bas à picomolaire au haut). IRM, imagerie par resonance magnétique; TEMP, tomographie d'émission monophotonique; TEP, tomographie par emission de positrons; TMD, tomodensitométrie.

la tomographie d'émission monophotonique (TEMP) permettent l'évaluation de changements chimiques potentiellement antécédents, par exemple, aux modifications anatomiques macroscopiques associées à une pathologie donnée.[3] Néanmoins, cette sensibilité accrue se fait au prix d'une résolution spatiale réduite (1-2 mm)[5] laquelle découle en partie de l'instrumentation (dimension des détecteurs) et de restrictions intrinsèques à la méthodologie (*positron range*, non-colinéarité).[6]

1.1.1.2 Désintégration radioactive et principe de la tomographie par émission de positons

Les radionucléides rendus instables par leur composition en neutrons et protons se désintègrent en émettant des radiations sous la forme de particles α, partiules β^-, particules β^+, par capture électronique ou encore par transition isomérique.[7] Les

radionucléides exploités en TEP sont riches en protons et se désintègrent par l'émission d'un positon (β^+) et d'un neutrino v avec conversion d'un proton (p) en neutron (n) suivant l'équation générale (1) suivante.

$$p \rightarrow n + \beta^+ + v \qquad \textbf{(1)}$$

L'énergie ainsi dégagée se trouve partagée entre le noyau fille, le positon et le neutrino. Conséquemment, les positons sont émis dans un évantail d'énergies – propre au radionucléide considéré. Par contre, les positons émis suivant une désintégration β^+ ont une demi-vie très courte au sein d'un milieu riche en électrons. Au sein d'un tissu, les positons perdent d'une part leur énergie cinétique par interactions inélastiques suivies, une fois l'essentiel de leur énergie dissipée après un parcours typiquement de $10^{-2} – 10^{-1}$ cm, par la formation d'un positronium par combinaison à un électron environnant**.**

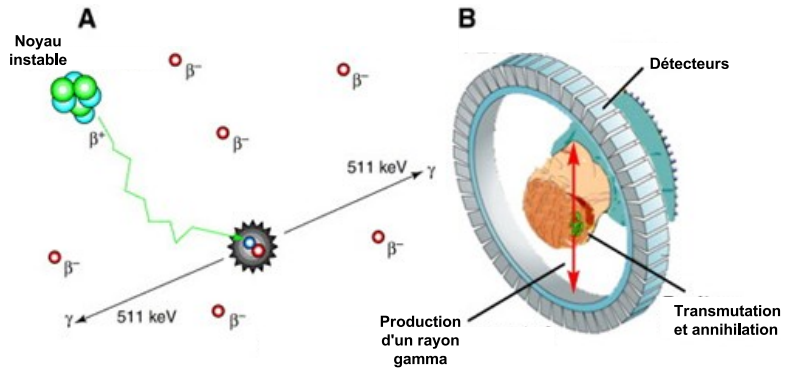

Figure 1.2. Principe de base de la tomographie par émission de positons. (A) Un positon β+ émis par la désintegration radioactive d'un noyau instable parcourt une courte distance ($10^{-2} – 10^{-1}$ cm) avant d'interagir avec un électron environnant β (représenté en rouge) et d'émettre deux photons gamma (γ) de 511 KeV à 180°. (B) Représentation d'un détecteur gamma d'une camera TEP représentant la corégistration des photons gamma produit lors de l'annihilation positon-électron (adapté de Ref. 4 et 8).

La formation d'un positronium ne persiste qu'approximativement 10^{-10} seconde avant qu'une annihilation positon-électron ne génère deux photons de haute énergie émis en direction opposée l'un de l'autre. Attendu l'état de quasi-repos du positon et de l'électron au moment de l'annihilation, l'énergie dégagée découle essentiellement des

masses des particules et correspond à 1.022 MeV (deux photons de 511 KeV). La détection coincidente à 180° de ces rayons gamma constitue le fondement de l'imagerie TEP (Figure 1.2).[8]

1.1.1.3 Sélection et production de radionucléides à courtes vies pour le TEP

En raison de leur courte demie-vie, les radioisotopes les plus couramment utilisés en chimie radiopharmaceutique pour fin d'application en TEP tel que ^{18}F, ^{11}C, ^{13}N et ^{15}O sont généralement produit par un cyclotron sur le site même où ils seront utilisés en radiosynthèse.

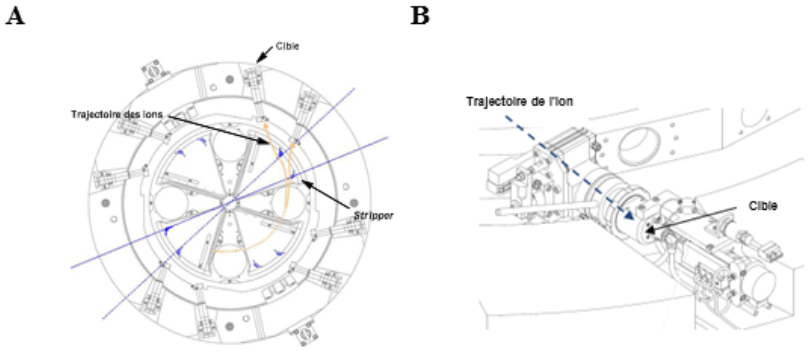

Figure 1.3. Composantes d'un cyclotron (IBA cyclone 18/9 cyclotron). (A) Les ions négatifs sont accélérés jusqu'à atteindre le *stripper*. La formation d'un ion positif par le retrait des électrons fait en sorte de rediriger l'ion en sens opposé. Les ions quittent ainsi le cyclotron pour être redirigés vers une cible. (B) Les ions déviés du cyclotron par le *stripper* entrent en collision avec le matériau cible pour produire les radioisotopes (adapté de la Ref. 9).

Brièvement, un cyclotron consiste en un accélérateur de particules circulaire au sein duquel, des particules chargées telles que H^-, générées par application d'un haut voltage à une source de H_2 au centre du cyclotron, sont accélérées par un champ électrique alternant et évoluent dans un champ magnétique appliqué perpendiculairement. Les particules accélèrent ainsi suivant une trajectoire en spirale vers l'extérieur jusqu'à atteindre une énergie donnée (1-40 MeV) pour être ensuite converties en protons et redirigées au contact d'un *stripper* (feuille de graphite) vers une cible où aura lieu la réaction nucléaire (Figure 1.3).[9]

Tableau 1.1. Propriétés de radionucléides couramment utilisés en TEP produit par cyclotron, demi-vies, réactions nucléaires, cibles, produits et produits de désintégration.

Radionucléides (Désintégration β +, %; E_{max} (β+))	**Demi-vie, $t_{½}$ (min)**	**Réaction nucléaire**	**Cible**	**Produit**	**Produit de désintégration**
^{11}C (100 %, 961 KeV)	20,4	^{14}N $(p,\alpha)^{11}C$	N_2 (+O_2) N_2 (+H_2)	[^{11}C]CO_2 [^{11}C]CH_4	^{11}B
^{13}N (100 %, 1190 KeV)	9,97	^{16}O $(p,\alpha)^{13}N$	H_2O H_2O + EtOH	[^{13}N]NO_x [^{13}N]NH_3	^{13}C
^{15}O (100 %, 1732 KeV)	2,04	^{15}N $(d,n)^{15}O$	N_2 (+O_2)	[^{15}O]O_2	^{15}N
^{18}F (97 %, 634 KeV)	110	^{20}Ne $(d,\alpha)^{18}F$ ^{18}O $(p,n)^{18}F$	Ne (+F_2) [^{18}O]H_2O	[^{18}F]F_2 $^{18}F^-$	^{18}O

Le tableau 1.1 illustre les propriétés des radioisotopes de courte demi-vie produit par un cyclotron exploités pour la TEP.[3] Ces isotopes peuvent être incorporés à de petites molécules ou greffés à une variété de biomolécules. D'autres radionucléides tels que le ^{68}Ga ($t_{1/2}$ = 68 min, $^{68}Ge/^{68}Ga$ - générateur), le ^{64}Cu ($t_{1/2}$ = 12,7 h, $^{64}Ni(p,n)\ ^{64}Cu$ - cyclotron), le ^{86}Y ($t_{1/2}$ = 14.7 h, $^{86}Sr(p,n)\ ^{86}Y$ - cyclotron) et le ^{89}Zr ($t_{1/2}$ = 78.4 h, $^{89}Y(p,n)\ ^{89}Zr$ - cyclotron), sont aussi largement exploités en radiochimie de coordination pour le radiomarquage de peptides, mimes peptidiques et anticorps. Les relatives longues demi-vies associées à différents radiométaux émetteurs β^+ sont avantageuses pour, par exemple, l'imagerie de processus biologiques associés à une lente pharmacocinétique.[10] Cependant, le ^{18}F est, parmi l'ensemble de ces radioisotopes, le plus couramment utilisé en TEP attendu sa demi-vie avantageuse de 110 minutes, sa faible énergie β^+ menant à une résolution particulièrement favorable de même qu'une relative facilité de production. Néanmoins, la relative petite quantité de composés fluoroorganiques parmi l'ensemble des molécules biologiquement actives implique que le design d'un traceur marqué au ^{18}F nécessite la synthèse et l'évaluation biologique d'un équivalent ^{19}F lorsque la molécule cible s'avère originalement non fluorée. Autrement, le ^{11}C est aussi exploité de manière routinière et présente l'avantage de pouvoir, généralement, être introduit sans modification struturelle du composé d'origine

vu l'ubiquité du carbone dans les molécules d'intérêt biologique. Par ailleurs, les courtes demi-vies du ^{15}O et du ^{13}N limitent leur utilisation TEP aux études de flot sanguin et de métabolisme.

1.1.2 Développement et applications de traceurs TEP

1.1.2.1 Les traceurs TEP comme outil diagnostique: l'exemple du 2-deoxy-2-[^{18}F]fluoro-D-glucose ([^{18}F]FDG)

L'intérêt croissant, au cours des trente dernières années, pour le développement et l'application de méthodologies de radiosynthèse pour la TEP et, de manière générale, l'intérêt vis-à-vis l'imagerie TEP elle-même, s'inscrit dans la foulée des travaux pionniers réalisés au Brookhaven National Laboratory sous la direction de Alfred P. Wolf ayant menés au développement du 2-deoxy-2-[^{18}F]fluoro-D-glucose ([^{18}F]FDG) à la fin des années 1970.[11] De nos jours, le [^{18}F]FDG est synthétisé suivant des variations d'une méthodologie mise en place par Hamacher au milieu des années 1980 partant du 1,3,4,6-tétra-*O*-acétyl-2-*O*-trifluormethanesulsonyl-β-$_D$-mannopyranose via S_N2 (*vide infra*) et est de loin le plus courant des traceurs TEP utilisés (Figure 1.4 (A); voir section 1.2.3 pour les détails méthodologiques).[12] Lorsque injecté, le [^{18}F]FDG agit d'abord de manière similaire au glucose et est transporté du plasma aux différents tissus par les transporteurs de glucose puis converti en [^{18}F]FDG-6-phosphate par l'hexokinase. La substitution en position 2 d'un hydroxyle par un atome ^{18}F inhibe plus avant la glycolyse et conduit à une accumulation de [^{18}F]FDG-6-phosphate au niveau cellulaire. Ainsi sont obtenu des données essentielles permettant de visualiser des régions, telles les néoplasmes, présentant un haut métabolisme de glucose relatif au tissu environnant (Figure 1.4 (B)).[13] Le [^{18}F]FDG constitue donc un exemple, relativement rare, de traceur *métabolique*. Par contre, les traceurs TEP sont couramment développés afin de se fixer à un récepteur spécifique sans avoir été au préalable métabolisé.

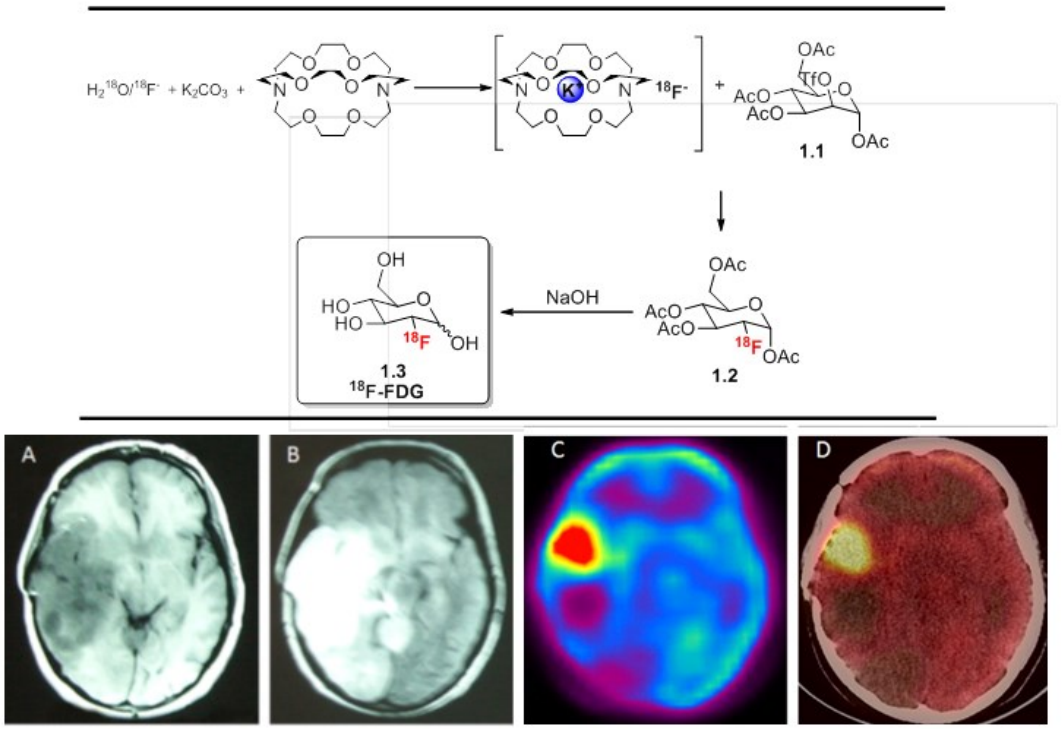

Figure 1.4. Synthèse et application du 2-deoxy-2-[^{18}F]fluoro-D-glucose ([^{18}F]FDG). (Haut) Synthèse du 2-deoxy-2-[^{18}F]fluoro-D-glucose. (Bas) Astrocytome grade II chez une patiente de 35 ans; récidive suivant une intervention chirurgicale et une radiothérapie. (A) et (B) Les images IRM montrent une large lésion temporo-pariétal. La lésion délimitée par l'IRM inclue la tumeur et la zone nécrotique. (C) et (D) [^{18}F]FDG TEP et TEP-TDM montrent une fixation au niveau de la tumeur viable sans fixation au niveau des tissus nécrotiques (Adapté de la Ref. 13).

1.1.2.2 Les traceurs TEP comme outils de recherche et de dévelopement pharmaceutique

De fait, de nombreux traceurs sont développés dans le but d'investiguer l'interaction entre un ligand et sa cible au niveau moléculaire de même que le niveau d'expression d'une cible protéique en corrélation avec une pathologie ou une condition donnée. Ce type d'investigation, fort utile sur le plan fondamental, peut aussi s'appliquer efficacement au développement de nouveaux médicaments – particulièrement au niveau du système nerveux central (SNC).[14] Ainsi, le radiomarquage au ^{18}F ou ^{11}C d'un médicament candidat peut permettre d'obtenir rapidement des informations pharmacocinétiques et pharmacodynamiques de manière non-invasive telles que la biodistribution, la concentration au niveau du cerveau (le passage de la

barrière hémato-encéphalique) de même que le métabolisme. Il est aussi possible de confirmer ou d'infirmer qu'un médicament candidat radiomarqué au ^{18}F ou ^{11}C se lie en effet à sa cible *in vivo* dans des modèles animaux en études précliniques ou chez des sujets humains dans des études cliniques. Différemment, l'administration d'un radioligand connu, se fixant au même site qu'un médicament en développement peut aussi permettre, dans une étude de blocage, de quantifier le niveau d'occupation des récepteurs pour ce médicament en corrélation avec la réponse pharmacodynamique. De plus, la quantification d'un biomarqueur associé à une pathologie peut aussi être suivie au cours de la mise en oeuvre d'un nouveau traitement au niveau pré-clinique.

1.1.3 Imagerie cérébrale par tomographie d'émission de positons; considérations particulières

La structure de certains des radiotraceurs couramment utilisés en neuroimagerie TEP est illustrée à la figure 1.5. Par ailleurs, pour être utiles, les radioligands destinés au SNC doivent satisfaires un ensemble contraignant de critères (Tableau 1.2) rendant leur développement complexe.[15]

1.1.3.1 Haute affinité et sélectivité

Dans un premier temps, l'affinité et la sélectivité d'un traceur pour sa cible représentent des facteurs d'une importance capitale.[16] Les constantes de dissociations (K_d) idéales sont attendues être dans l'ordre du faible nanomolaire.[14b] Évidemment, ce critère d'affinité est aussi dépendant de l'expression du récepteur ou de l'enzyme ciblé. Qui plus est, l'affinité la plus haute doit l'être à l'endroit de la cible d'imagerie et idéalement au moins 100 fois supérieurs aux affinités associées à des interactions avec des sites secondaires. Ici encore, cette sélectivité est dépendante de l'expression régionale des sites d'interaction secondaires potentiels.

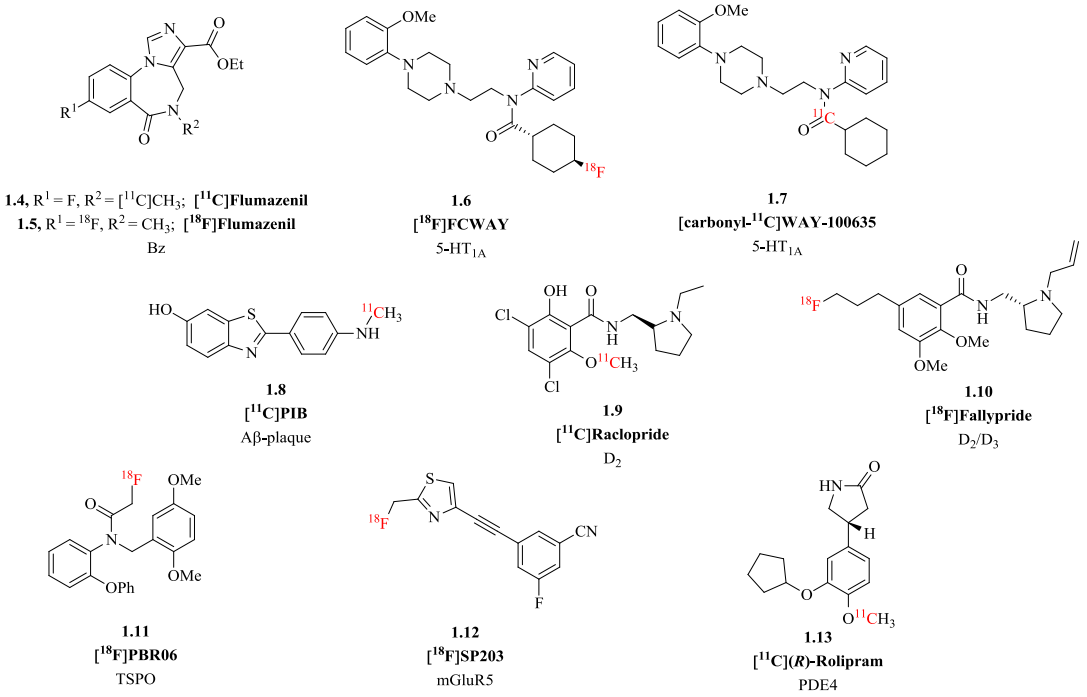

Figure 1.5. Exemples de radiotraceurs TEP et leur cible respective destinés à l'étude du système nerveux central.

Le cas où un radiotraceur présente une affinité considérable pour une protéine autre que celle visée mais qui n'est exprimée que dans une région ou un tissu anatomiquement distant du site du récepteur visé peut évidemment être acceptable.

1.1.3.2 Concentration de la cible

Il est aussi important que la concentration du site de liaison, le neurorécepteur visé, soit considérablement plus importante que la concentration du radioligand.[17] Autrement formulé, la densité du récepteur (B_{max}) doit excéder K_d ($B_{max} > K_d$ ou [LR] > [L] où [LR] et [L] sont respectivement la concentration du radioligand fixé au récepteur et la concentration du radioligand libre).[18]

1.1.3.3 Poids moléculaire, lipophilicité et barrière hémato-encéphalique

Le poids moléculaire et la lipophilicité d'un radiotraceur destiné au SNC sont des éléments cruciaux pour differents facteurs. D'une part, le radiotraceur doit traverser la barrière hémato-encéphalique, laquelle, pour diverses raisons dont une trop faible

lipophilicité, est essentiellement imperméable à plus de 98% des molécules de petits poids moéculaires (M < 400 Da) de même qu'à la totalité des larges molécules exogènes.[19] De fait, à la difference de la perméabilité caractéristique des cellules endothéliales des capillaires sanguins en périphérie, les capillaires du cerveau présentent des jonctions serrées empêchant le transport paracellulaire de molécules circulant dans le sang vers le cerveau (Figure 1.6).[20a]

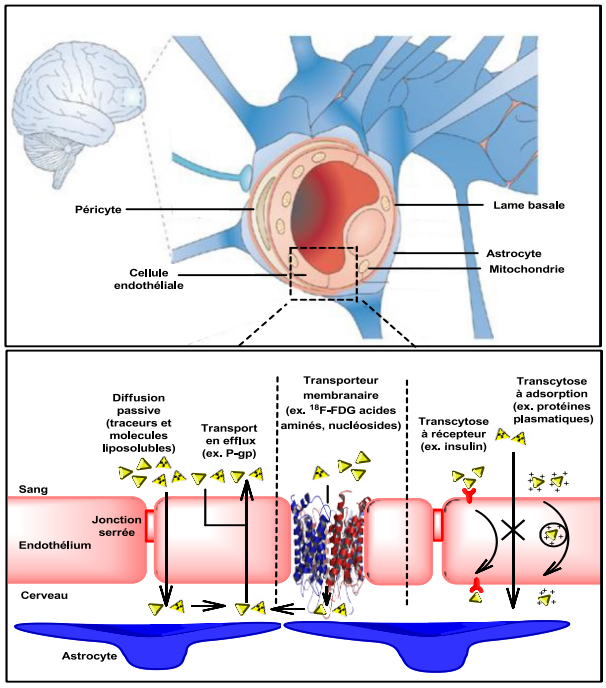

Figure 1.6. Représentation schématique de la barrière hémato-encéphalique. (Haut) Représentation d'un capillaire du cerveau; les cellules endothéliales sont reliées par des jonctions serrées. (Bas) Les différents types de transport: diffusion passive, transport en efflux, transporteur membranaire, trancytose à récepteur, transcytose à adsorption. Les radioligands de type petite molécule exogène peuvent traverser la barrière hémato-encéphalique par diffusion passive et sont potentiellement sujettes aux P-gp. D'autres radioligands comme le [^{18}F]FDG traversent la barrière hémato-encéphalique par le biais de transporteurs membranaires. (Adapté de la Ref. 20b).

Conséquemment, les petites molécules comme les radiotraceurs, à l'exception de certains composés endogènes ou reconnus comme tel (ex. [^{18}F]FDG), ne peuvent traverser la barrière hémato-encéphalique que par diffusion passive et encore, sont sujettes aux transporteurs en efflux tels que les glycoprotéines P – d'où l'influence

négative d'un poids moléculaire trop élevé ou d'une lipophilicité trop faible. A l'opposé, dans le cas de petites molécules organiques, une trop grande lipophilicité peut favoriser la liaison aux protéines plasmatiques et conséquemment, diminuer la fraction de traceur libre (f_p) dans le plasma disponible pour traverser la barrière hémato-encéphalique. Une lipophilicité trop élevée peut aussi entrainer une augmentation de la liaison non-spécifique dans le SNC et diminuer la qualité des images obtenues.[15] Il est estimé qu'un traceur présentant un logP dans une fourchette de +1 à +4 est optimal.[14b]

1.1.3.4 Stabilité in vivo

De plus, un radiotraceur doit être résistant face au métabolisme durant la période nécessaire à l'acquisition des données *in vivo*. D'abord, et cela s'applique à l'ensemble des radiotraceurs qu'ils soient destinés au SNC ou en périphérie, un métabolisme considérable entrainant une élimination rapide du traceur métabolisé ne permet évidemment pas d'aquérir des données sur l'interaction d'un ligand avec sa cible en dépit d'une affinité favorable et de conditions idéales. Aussi, dans le cas d'agents de neuroimagerie, le métabolisme, s'il a lieu, doit être limité idéalement à des processus en périphérie menant à des radiométabolites présentant une faible propention à pénétrer le cerveau ou ayant une faible affinité pour la protéine cible. L'évaluation du métabolisme est donc un facteur décisif au succès d'un radiotraceur mais varie significativement entre les espèces, ce qui implique qu'un traceur avec un faible profil métabolique dans les rats par exemple, peut néanmoins présenter un métabolisme favorable dans d'autres espèces (primates non-humains et humains).[15]

1.1.3.5 Radiosynthèse et activité spécifique

Finalement, la posibilité de radiosynthétiser un traceur de haute activité spécifique (A_S) partant d'un précurseur adéquat dans un délais court de quelques minutes ou dizaines de minutes – étant donné la courte demi-vie des isotopes utilisés – constitue la condition *sine qua none* au développement de l'imagerie TEP. Il s'agit aussi de l'objet central de la chimie radiopharmaceutique qui sera discuté dans la prochaine section.

Table 1.2. Résumé des critères associés au développement de ligands TEP destinés aux neurorécepteurs (adapté de la Ref. 14b).

Propriétés	**Critères clés**
Radiochimie	- Possibilité de radiomarquage avec le carbone-11 ou le fluor-18 - Possibilité de radiomarquage avec haute activité spécifique - Radiomarquage sur une position ne menant pas à la formation de radiométabolites traversant la barrière hémato-encéphalique
Biochimie	- Haute affinité vis-à-vis du récepteur visé (K_d idéalement dans l'ordre des faible nM) - Haute sélectivité: idéalement 100 fois supérieure vis-à-vis d'autres sites de liaisons - Faible liaison non spécifique
Exposition cérébrale favorable	- Lipophilicité: logP entre +1 et +4 - Ne constitue pas un substrat des P-glycoprotéines - Faible liaison aux protéines plasmatiques

L'activité spécifique (A_S) se définie comme le ratio entre l'activité du composé traceur marqué et de l'ensemble des autres versions isotopiques du même composé tel qu'illlustré à l'équation 2 suivante:

$$A_S = A_A / (n_n + n_B + n_c + n_D) \qquad (\mathbf{2})$$

Où A_A correspond à la quantité de radioactivité de l'espèce A et n_A, n_B, n_c et n_D les quantités molaires des espèces A, B, C et D si elles existent (exprimé en GBq/μmol ou Ci/μmol). Dans le cas où les récepteurs visés sont exprimés en faible quantité, comme pour bon nombre de neurorécepteurs, ce paramètre est essentiel.

1.2 Radiochimie pharmaceutique du carbone-11 et du fluor-18

L'adaptation en radiochimie de méthodologies efficaces et éprouvées en chimie organique *traditionelle* constitue une tâche parfois complexe et difficile en raison des limitations de temps de même que des limitations de stoechiométrie inhérentes à la manipulation de radionucléides à courte vie. A l'opposé, dans certains cas, des transformations chimiques ardues en synthèse organique peuvent, lorsque appliquées en chimie radiopharmaceutique, s'avérer fort efficaces précisément en raison de ces mêmes facteurs intrinsèques. De manière générale néanmoins, le développement de méthodes de synthèse impliquant des radioisotopes de courtes vies est loin d'être trivial et requiert une quantité importante d'optimisation. En conséquence, l'éventail de méthodologies synthétiques disponibles ou même possibles en radiochimie pharmaceutique ne constitue qu'une fraction des approches normalement envisageables en chimie *froide*.
Cette section présente un survol, non exhaustif, des méthodes de radiomarquage au carbone-11 et fluor-18 couramment utilisées pour la synthèse de traceurs pour la TEP de même que certaines considérations inhérentes se rattachant à ce type de chimie.

1.2.1 Radiochimie; considérations particulières

1.2.1.1 Temps

En premier lieu et comme mentionné précédemment, les réactions développées doivent répondre à une exigence de temps associée à la demi-vie des radioéléments en jeu. Il est attendu que les produits de radiomarquage doivent approximativement être synthétisés, purifiés, analysés et formulés en l'espace de 2 à 3 demi-vies, c'est-à-dire de quelques minutes à quelques heures.[3] De ce fait, les méthodologies de synthèse de longue durée sont proscrites.

1.2.1.2 Haute dilution et impuretés

Les radioisotopes générés par un cyclotron et utilisés en radiosynthèse ne comptent que pour quelques centaines de picomoles rendant les réactions avec un précurseur donné, même présent dans une quantité de l'ordre du milligrame ou moins, significativement disproportionnées en faveur du précurseur (cinétique de pseudo

premier odre). Il arrive que cette stoechiométrie extraordinaire (excès de précurseur de l'ordre de 10^4) s'avère avantageuse sur le plan cinétique, permettant la complétion, par rapport au radioélément, de réactions autrement impossibles ou difficiles (*vide infra*). Par contre, la manipulation de si petite quantité d'un radioélément réactif peut aussi avoir pour conséquence la formation de réactions secondaires imprévues provenant d'impuretés, présentes parfois qu'à l'état de traces. De plus, ces faibles concentrations de radioisotopes font en sorte que la radioactivité spécifique théorique est nettement supérieure à celle obtenue en pratique en raison de dilutions isotopiques intervenant à différents niveaux de la production du radioélément jusqu'à la réaction de radiochimie. Par exemple, les activités spécifiques obtenuent en pratique pour le ^{11}C et le ^{18}F sont typiquement entre 1 et 10 Ci/µmol et excèdent rarement quelques dizaines de Ci/µmol alors que les activités spécifiques théoriques sont environ 10^3 fois supérieures.

1.2.1.3 Purification

La purification des radiotraceurs s'effectue typiquement par chromatographie liquide haute performance (CLHP) muni d'un détecteur pour la radioactivité. Le suivi des réactions de même que le contrôle de qualité se font soit par CLHP, chromatographie gazeuse (CPG) ou chromatographie sur couche mince (CCM). L'identité chimique du radiotraceur s'effectue par comparaison avec le temps de rétention (t_R) du composé non marqué.

1.2.1.4 Radioactivité: automatisation

De manière générale, les manipulations impliquant la radioactivité sont monitorées, et effectuées avec le souci constant de limiter de façon maximale l'exposition à la radioactivité du personnel avec l'utilisation de mur ou de cellules de plomb et modules de synthèse automatisés. Le type de précautions à mettre en place dépend nécessairement de la quantité de radioactivité manipulée.

1.2.2 Stratégies de radiomarquage pour le carbone-11

L'omniprésence du carbone au sein des molécules bioactives sert avantageusement le marquage isotopique au ^{11}C et permet, suivant une méthodologie de radiosynthèse adéquate, d'obtenir un radiotraceur indiscernable sur le plan physico-chimique – à l'exception d'effets isotopiques cinétiques légers. L'ensemble des ^{11}C-précureurs utilisés en radiosynthèse sont dérivés du $[^{11}C]CO_2$ et du $[^{11}C]CH_4$ mais tous ne sont pas produit routinièrement au sein d'un même laboratoire – puisque la préparation de chacun des ces précuseurs nécessite des transformations spécifiques et automatisées (Schéma 1.1).[21]

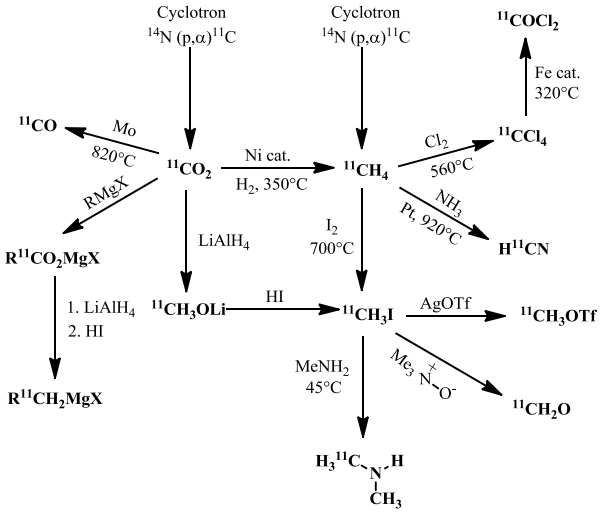

Schéma 1.1 Préparation de ^{11}C-précurseurs communs en radiosynthèse.

Les précuseurs radiomarqués tels que l'iodométhane ($[^{11}C]CH_3I$) et le trifluorométhanesulfonate de méthyle ($[^{11}C]CH_3OTf$) sont de loin les précurseurs les plus couramment utilisés mais s'accompagnent d'une variété d'autres fragments tels que le monoxide de carbone ($[^{11}C]CO$), les réactifs de Grignard ($R[^{11}C]CH_2MgX$), le phosgène ($[^{11}C]COCl_2$), le méthanolate de lithium ($[^{11}C]CH_3OLi$), le formaldéhyde ($[^{11}C]CH_2O$), le cyanure d'hydrogène ($H[^{11}C]CN$) et diméthylamine ($[^{11}C]$diméthylamine) entre autres (Schéma 1.1).

1.2.2.1 Réactions de ^{11}C-méthylations nucléophiles et couplages croisés

Les ^{11}C-méthylations avec le [^{11}C]CH_3I ou le [^{11}C]CH_3OTf représentent la plus courante des méthodes utilisées afin d'incorporer un atome de ^{11}C au sein d'une molécule organique. Ces réaction S_N2 procèdent efficacement, généralement en quelques minutes, partant d'une multitude de nucléophiles (amines, alcools, phénols, amides, thiols).[22] L'utilisation de bases ou de températures élevées dépend à la fois de la nature du substrat et de l'agent d'alkylation utilisé. La radiosynthèse de substrats désactivés, tel que les précuseurs **1.14** et **1.15** utilisés pour la radiosynthèse du traceur [^{11}C]PIB,[23] illustre la différence de réactivité du [^{11}C]CH_3I vis-à-vis du [^{11}C]CH_3OTf et de leur application à la méthylation d'un nucléophile azoté (Schéma 1.2).[24,25]

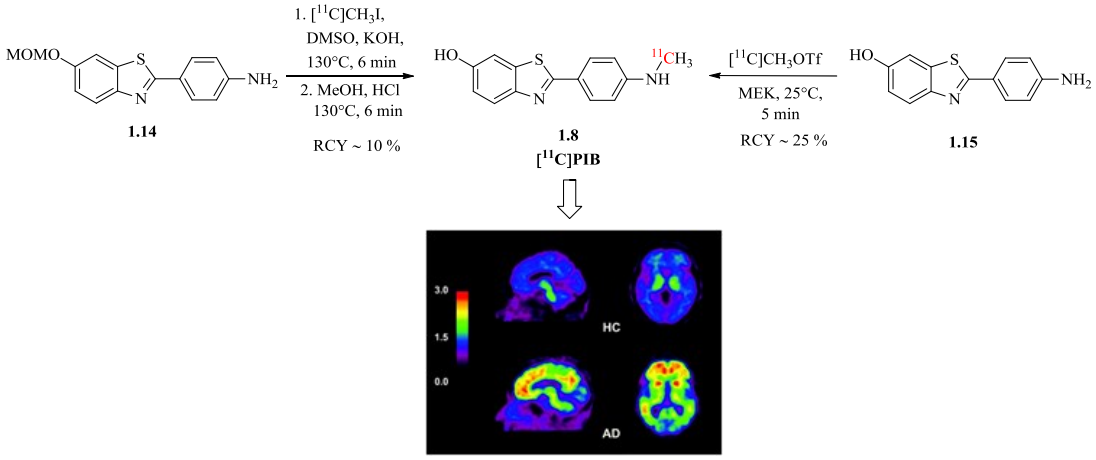

Schéma 1.2. Synthèses et application de [^{11}C]PIB. (*Haut*) Deux radiosynthèses distinctes de [^{11}C]PIB. (*Bas*) Images TEP suivant l'administration de [^{11}C]PIB montrant le cerveau d'un individu en santé (*HC: healthy control*) et d'un patient avec la maladie d'Alzheimer (*AD: Alzheimer disease*). Les couleurs chaudes indiquent une forte accumulation de [^{11}C]PIB et suggèrent la présence de plaques Aβ (Adapté des Ref. 24-25).

Ainsi, [^{11}C]PIB peut être obtenu partant du précuseur *O*-protégé **1.14** en présence de potassium d'hydroxide et de [^{11}C]CH_3I à haute température suivie d'une déprotection du MOM éther. Alternativement, le même traceur peut être obtenu via une méthylation régiosélective partant de **1.15** avec le [^{11}C]CH_3OTf. L'utilisation d'un précurseur déprotégé suivant les conditions utilisées avec le [^{11}C]CH_3I est évidemment proscrite vu

la formation concommitante d'un phénolate, lequel réagirait préférentiellement avec l'agent d'alkylation.

Par ailleurs, le [^{11}C]CH_3I est aussi exploité avec succès dans une multitude de réactions de couplages croisés médiées au palladium.[26] Le Schéma 1.3 suivant illustre quelques exemples typiques tels que le couplage de Suzuki,[27] le couplage de Sonogashira,[28] le couplage de Stille[29] et le couplage de ziroconocènes d'alcényles.[30]

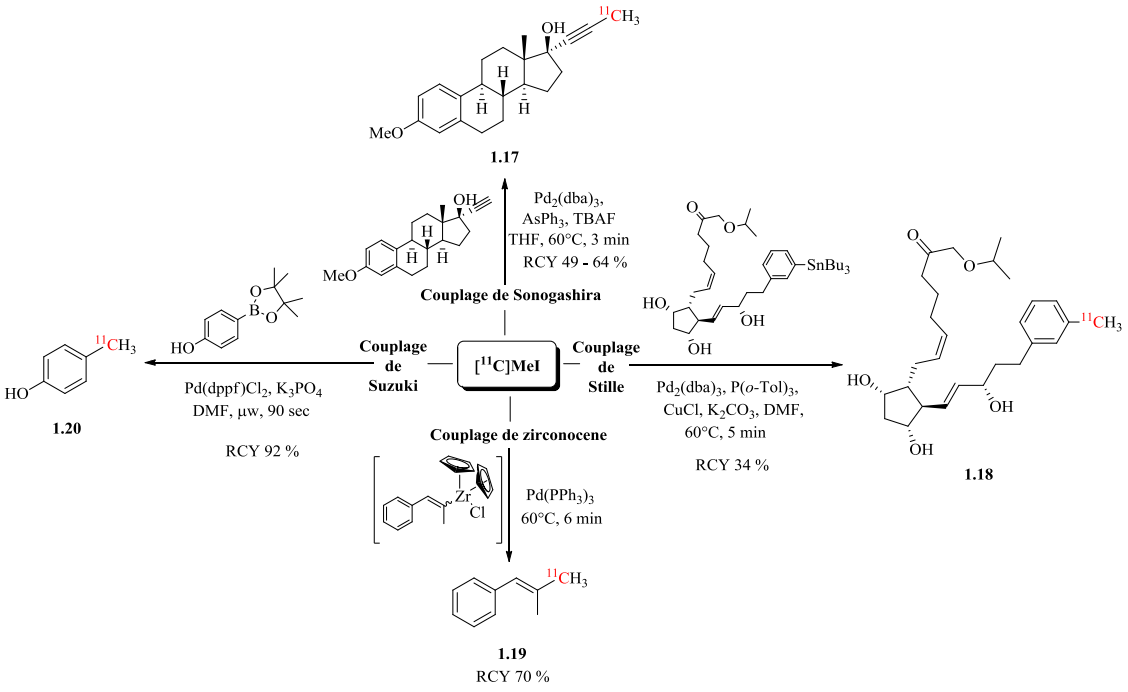

Schéma 1.3. Exemple de réactions de couplages croisés médiées au palladium avec [^{11}C]CH_3I: couplage de Suzuki, couplage de Sonogashira, couplage de Stille et couplage de zirocnocènes d'alcényles. (L'utilisation du terme *médié* plutôt que *catalysé* découle de la stoechiométrie excessive de Pd(0) face à la source de ^{11}C).

1.2.2.2 Réactions impliquant du [^{11}C]dioxide de carbone

Le [^{11}C]CO_2 peut être converti en organomagnésiens ou organolithiens d'halogénures radiomarqués puis être utilisé pour former un lien amide en présence d'un agent de couplage adéquat ou simplement transformé en ^{11}C-chlorure d'acyle pour réagir avec un nucléophile tel que répresenté pour la synthèse du traceur [*carbonyle*-^{11}C]WAY100635, un important ligand des récepteurs $5HT_{1A}$ (Schéma 1.4).[31,32] Une

attention particulière doit être porté au dégazage de même qu'aux conditions inertes lors de la mise en place de telles manipulations afin d'éviter une dilution isotopique provenant du CO_2 atmosphérique lors de la formation du réactif organométallique. Des approches plus douces ont aussi été développées pour l'utilisation du [^{11}C]CO_2 dont quelques unes sont illustrées au schéma 1.6: réaction de triphénylphosphinimines,[33] formation de ^{11}C-carbamates promue au DBU[34] et conversion directe d'ester boronique par carboxylation catalysée au cuivre(I).[35]

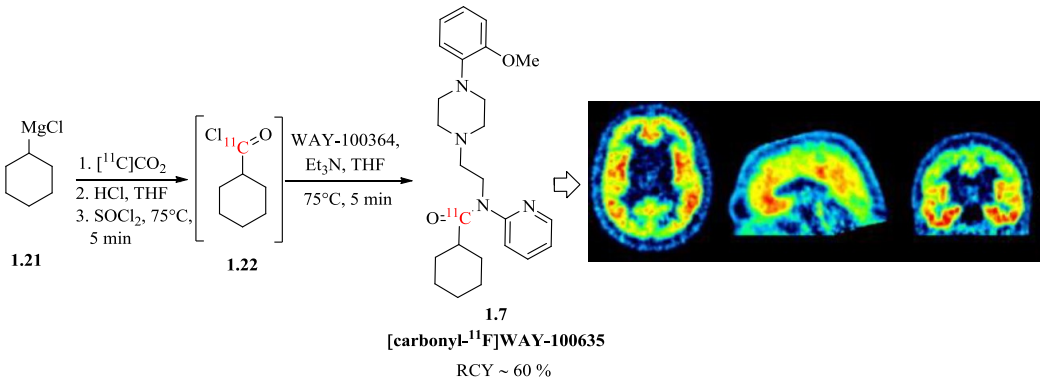

Schéma 1.4. Synthèse et application de [*carbonyle*-^{11}C]WAY100635. (*Gauche*) Radiosynthèse en un pot de [*carbonyle*-^{11}C]WAY100635 par acylation avec le chlorure de [*carbonyle*-^{11}C]cyclohexyloyle (**1.22**) partant du réactif de Grignard **1.21**. (*Droite*) Distribution du traceur [*carbonyle*-^{11}C]WAY100635 fixé au récepteur $5HT_{1A}$ (contrôle).

1.2.2.3 Réactions impliquant du [^{11}C]phosgène

L'utilisation du [^{11}C]$COCl_2$, fragment hautement réactif mais dont la synthèse peut être techniquement complexe, demeure relativement marginale mais peut permettre la synthèse d'urées, de carbamates et d'amides radiomarqués.[36]

1.2.2.4 Réactions de ^{11}C-cyanations

L'utilisation du [^{11}C]HCN peut se faire directement comme avec, par exemple, une réaction de Rosenmund-von Braun[37] illustrée avec la synthèse de **1.28**, en ouverture d'aziridine dans la radiosynthèse d'acides amines[38] tel **1.26** ou encore comme précurseur de carbonyle via une cyanation en présence de palladium[39] (Schéma 1.6).

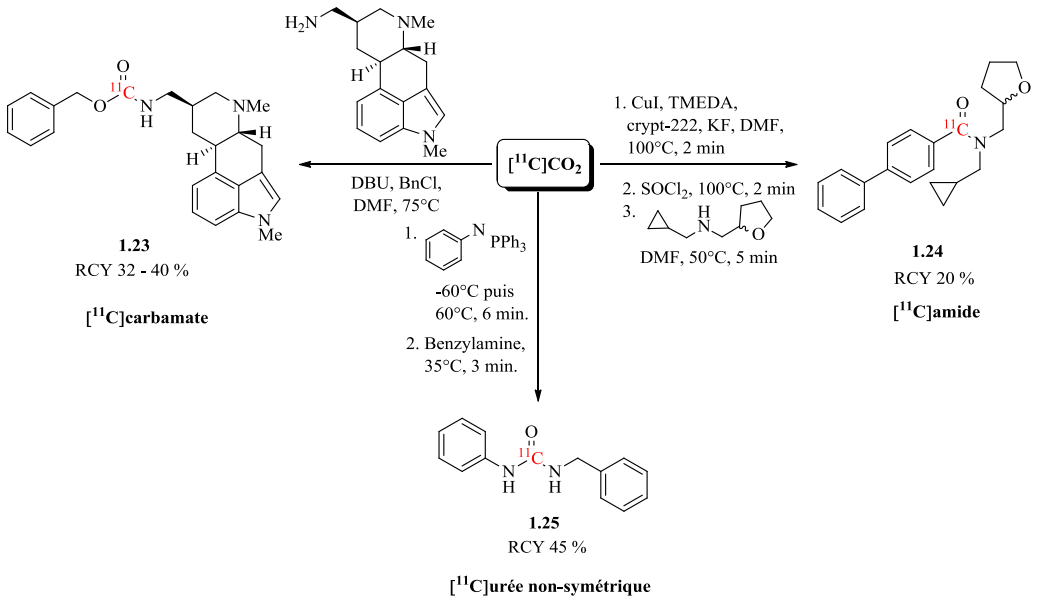

Schéma 1.5. Exemples d'applications pour l'utilisation du précurseur [^{11}C]CO_2 en radiosynthèse pharmaceutique: réaction de triphénylphosphinimines, formation de ^{11}C-carbamates promue par DBU et conversion directe d'ester boronique par carboxylation catalysée au cuivre(I).

1.2.2.5 Réactions de carbonylation avec [^{11}C]monoxide de carbone

Finalement, le [^{11}C]CO constitue un précurseur dont l'application est en croissance même si son utilisation est associée à certaines difficultées pratiques en raison de sa faible solubilité dans les solvents organiques, exacerbée par l'utilisation de traces de réactif, caractéristique de la radiochimie.[40] Néanmoins, diverses méthodes telles que l'utilisation de modules de radiosynthèse opérant en haute pression[41] ont permi de mener à bien une multitude de carbonylations médiées au palladium (Schéma 1.7). Le traceur PK11195 (**1.30**), traditionnellement synthétisé par ^{11}C-méthylation d'un précuseur amide secondaire, peut être alternativement obtenu avec un marquage en position du carbonyle partant du précurseur aryl triflate **1.29** (Schéma 1.7).[42]

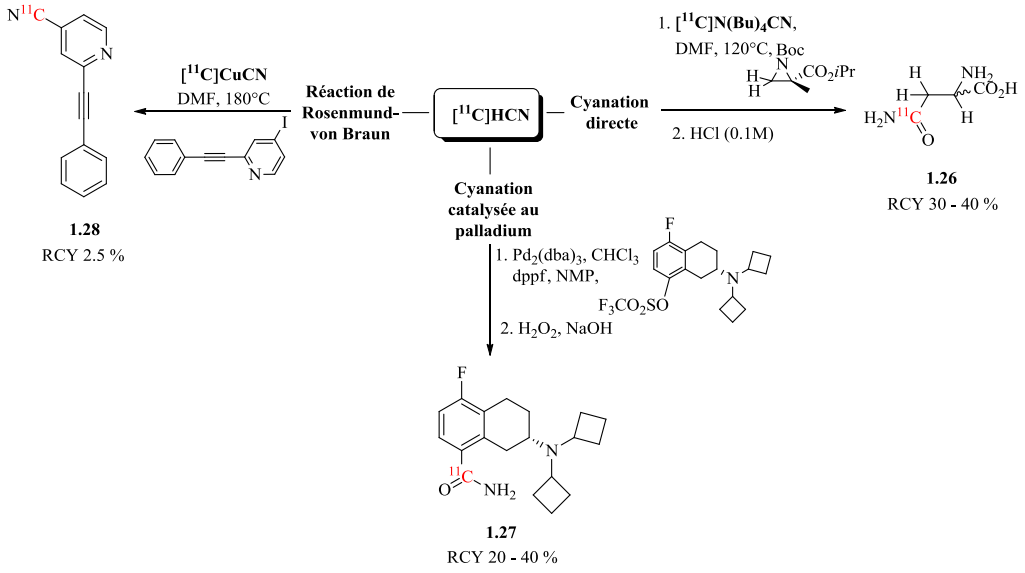

Schéma 1.6. Applications du précurseur [^{11}C]HCN en radiosynthèse; réaction de Rosenmund-von Braun, cyanation directe et cyanation au palladium.

Aussi, les radiomarquages de carbonyle avec le [^{11}C]CO se positionnent avantageusement à bien des égards par rapport aux réactions de carboxylation impliquant le [^{11}C]CO_2 qui sont, d'une part, problématiques en raison de la dilution isotopique lors de la réaction[43] et, limitées aux substrats pouvant généralement tolérer la formation d'un réactif de Grignard ou d'un organolithien.

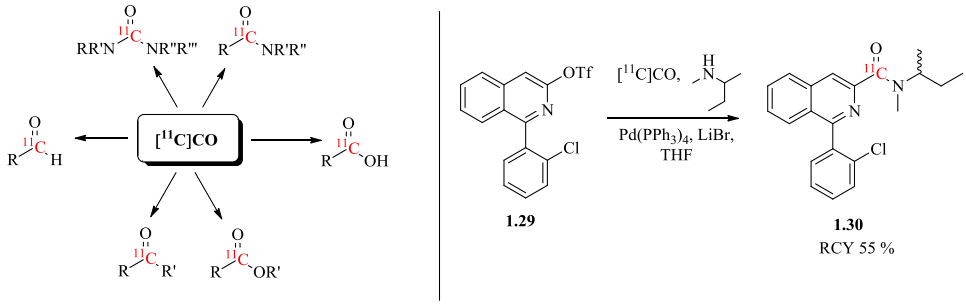

Schéma 1.7. Applications des carbonylations médiées au palladium avec [^{11}C]CO. (*Gauche*) Formation d'aldéhydes, d'urées, d'amides, de cétones, d'esters et d'acides carboxyliques. (*Droite*) Application dans une radiosynthèse alternative de PK11195 (**1.30**).

1.2.3 Stratégies de radiomarquage pour le fluor-18

Comme mentionné précédemment (section *1.1.1.3*), le ^{18}F constitue en chimie radiopharmaceutique le radionucléide de choix en raison de ses propriétés nucléaires. Néanmoins, l'utilisation du ^{18}F plutôt que du ^{11}C présente certains désavantages principalement liés au fait qu'un nombre limité de molécules bioactives contiennent un atome de fluor *per se* – qui plus est, un atome de fluor dans une position susceptible de mener à un radiomarquage efficace et de haute activité spécifique. Conséquemment, ces molécules doivent être structurellement modifiées et leurs profils biologiques évalués pour assurer que l'introduction d'un atome de fluor n'influence pas négativement l'affinité du ligand pour sa cible. Par chance, le remplacement d'un hydroxyle ou d'un hydrogène par un atome de fluor représente l'une des substitutions bioisostériques la plus exploitée en chimie médicinale et est généralament favorable vis-à-vis des propriétés chimiques, physiques et pharmacologiques des composés biologiquement actifs.[44]

Par ailleurs, la forte électronégativité du fluor et la formation d'espèces hautement hydratées font du $^{18}F^-$ obtenu de la réaction ^{18}O $(p,n)^{18}F$ partant de $[^{18}O]H_2O$ un nucléophilile nécesairement médiocre. Typiquement, pour être utile dans des réactions de substitutions nucléophiles, le $^{18}F^-$ est d'une part séché par passage sur une cartouche échangeuse d'ions, puis élué avec une solution de carbonate de potassium dans un mélange d'acétonitrile et d'eau contenant du kryptofix-222 (K_{222}). Les traces d'eau dans la solution sont ensuite retirées par séchage azéotropique libérant le $^{18}F^-$ ''nu'', hautement nucléophile lorsque redissous dans un solvent polaire aprotique (DMF, DMSO, MeCN, sulfolane).

1.2.3.1 Réactions de ^{18}F-substitutions nucléophiles aliphatiques

Lorsque le traceur visé peut être obtenu partant d'un précurseur jouxté d'un groupement partant adéquat sur une position aliphatique, une réaction S_N2 peut permettre l'incorporation efficace d'un atome de ^{18}F en une étape – ou plusieurs dans le cas de déprotections ou de transformations subséquentes à la radiofluorination par

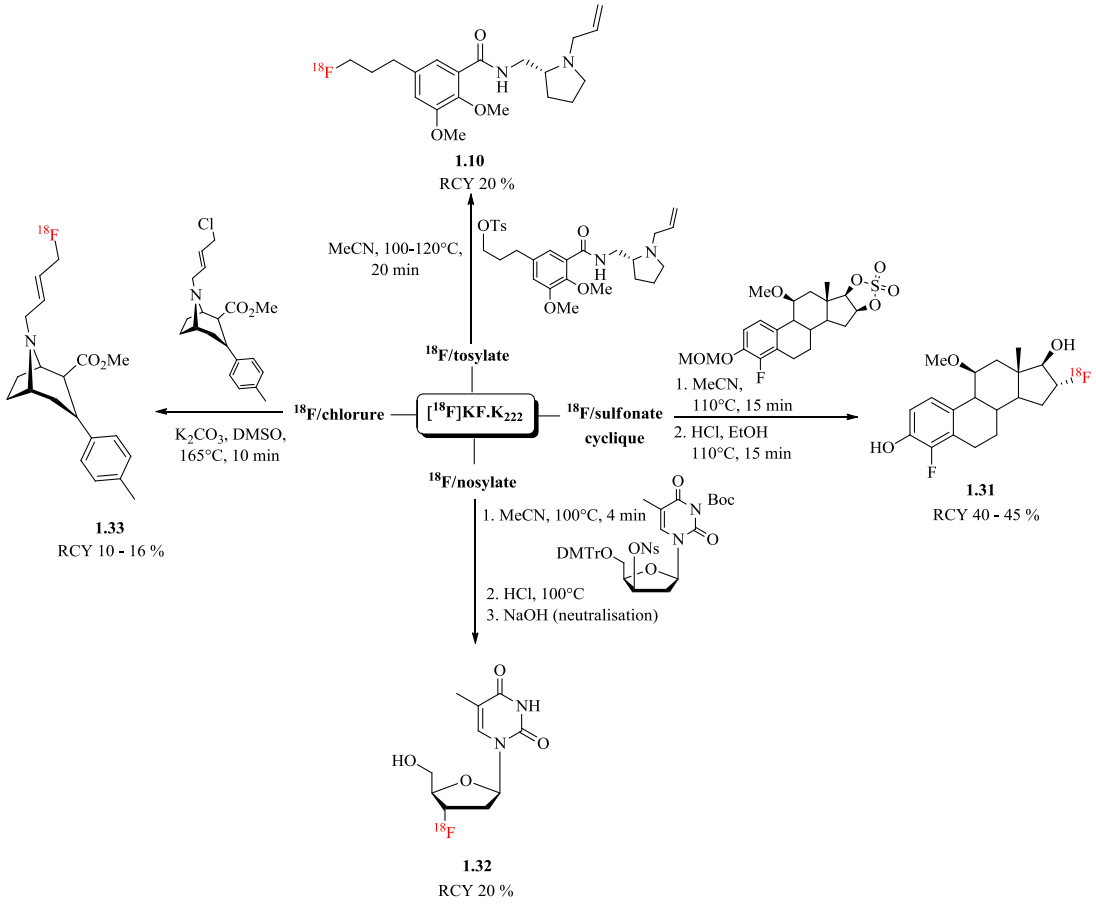

Schéma 1.8. Réactions de substitution nucléophile aliphatique avec le ^{18}F; différents groupements partants adéquats: tosylates, nosylates, sulfonates cycliques et halogénures.

exemple. Le schéma 1.8 illustre la synthèse des traceurs [^{18}F]LBT-999 (**1.33**),[45] [^{18}F]FLT(**1.32**),[46] [^{18}F]fallypride (**1.10**)[47] et d'un dérivé de [^{18}F]estradiol (**1.31**)[48] partant d'un halogénure, d'un nosylate, d'un tosylate et d'une sulfonate cyclique respectivement. Lorsque les radiomarquages directs sont impossibles ou difficiles, la radiosynthèse de groupements prosthétiques marqués suivie par leur introduction au cours d'une seconde étape au sein de la molécule d'intérêt peut être envisagée (Schéma 1.19).

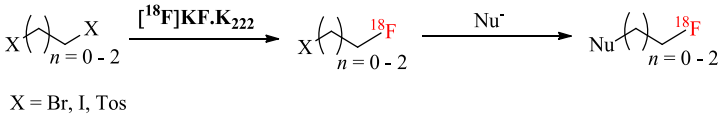

Schéma 1.9. Radiosynthèse de fragments [^{18}F]fluoroaliphatiques.

1.2.3.2 Réactions de ^{18}F-substitutions nucléophiles aromatiques

Les réactions S_NAr directes partant d'un précurseur nitro ou trialkylamonium triflate adéquatement activé par un groupement électron attracteur en position *ortho* ou *para* sont fréquemment exploitées et mènent à une variété de ^{18}F-fluoroaryles fonctionnalisés (Schéma 1.10).[49] Ces réactions sont par contre fréquemment associées à de faibles rendements radiochimiques. A cet égard, les sels de diaryliodonium constitutent une alternative efficace pour la synthèse de ^{18}F-fluoroaryles riches en électrons autrement inaccessibles ou obtenus avec un faible rendement (Schéma 1.11).[50,51]

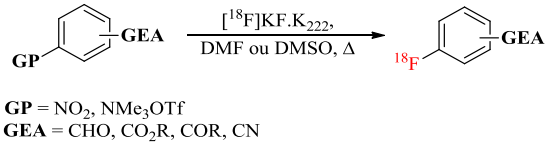

Schéma 1.10. Substitution nucléophile aromatique avec le ^{18}F (GP = groupement partant, GEA = groupement électroattracteur).

De plus, une multitude de fragments prosthétiques ^{18}F-aryles obtenus par S_NAr peut être synthétisée puis greffée dans des conditions douces relativement à la S_NAr proprement dit – dans le cas de biomoécules par exemple.

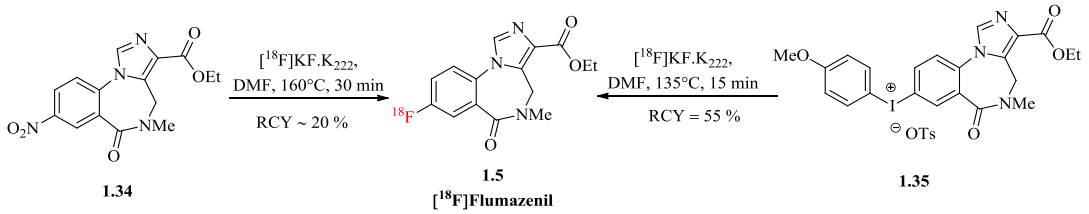

Schéma 1.11. Radiosynthèse du [^{18}F]flumazenil (**1.5**) suivant deux approches distinctes (*meta*-substitué); précurseur de types nitro et sel d'iodonium.

1.2.3.3 Réactions ^{18}F-fluorinations électrophiles

Les réactions de radiofluorinations électrophiles avec $[^{18}F]F_2$ sont, comparativement aux réactions de radiofluorinations nucléophiles, fort moins exploitées en raison des faibles activités spécifiques typiquement obtenues – inhérentes à la méthode de production du $[^{18}F]F_2$ – de même que l'absence fréquente de spécifité de marquage menant à l'obtention de mélanges ^{18}F-fluorés.

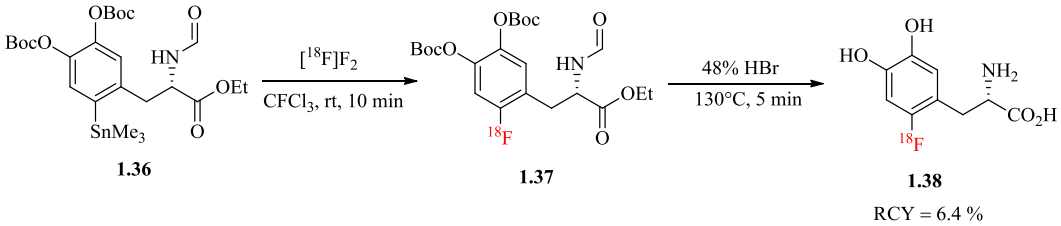

Schéma 1.12. Radiosynthèse de $[^{18}F]$FDOPA (**1.38**) par ^{18}F-fluorodestannylation avec $[^{18}F]F_2$.

Néanmoins, certains subtrats autrement inaccessibles ont été synthétisés suivant cette voie. Par exemple, le $[^{18}F]$FDOPA (**1.38**) est couramment produit par ^{18}F-fluorodestannylation avec $[^{18}F]F_2$ tel qu'illustré au Schéma 1.13.[52] Des réactifs de fluorination électrophile de type NF marqués au ^{18}F, tel que le $[^{18}F]$Selectfluor bis(triflate), ont aussi été récemment développés (Schéma 1.13).[53]

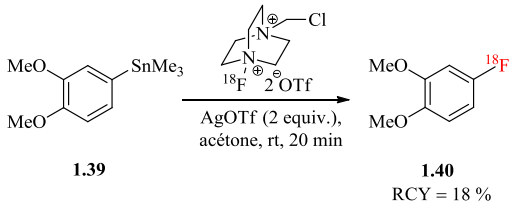

Schéma 1.13. ^{18}F-Fluorodestannylation avec le $[^{18}F]$Selectfluor bis(triflate).

1.2.3.4 Stratégies aryle-umpolung

L'utilisation de réactifs du type [^{18}F]Selectfluor bis(triflate) est prometteuse mais présente le désavantage de nécessiter la manipulation du [^{18}F]F_2 duquel ils découlent. Par ailleurs, la possibilité de générer une espèce radiofluorée électrophile partant du $^{18}F^-$ offrirait une alternative de haute activité spécifique aux applications diverses.

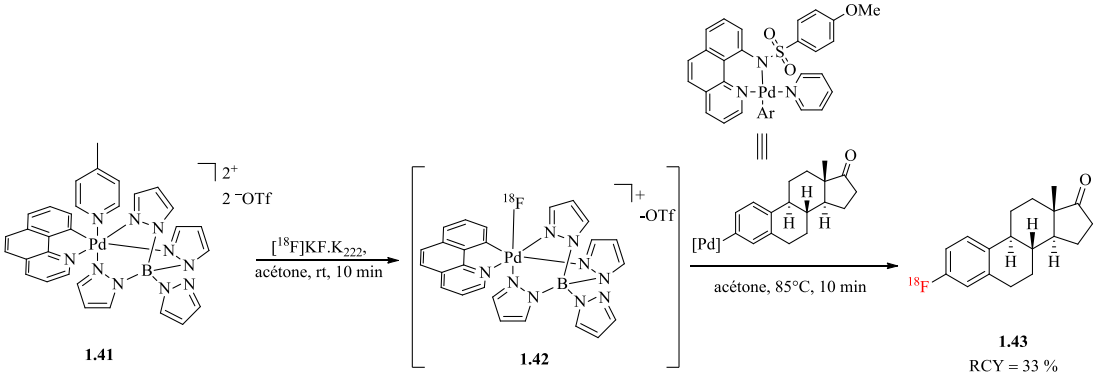

Schéma 1.14. Fluorination *umpolung* médiée au palladium.

Un tel réactif a récemment été reporté et exploite un complexe Pd^{IV} fluorophilique (**1.41**) qui une fois ^{18}F-fluoré, agit comme groupement partant lorsque traité avec un précurseur aryle-Pd^{II}.[54] Aussi, une synthèse originale 4-[^{18}F]fluorophénols a aussi été récemment reportée via une séquence fluorination oxydante.[55] Dans ce cas, le fragment aryle plutôt que le $^{18}F^-$ est oxydé et du fait, converti en espèce électrophile réactive vis-à-vis du $^{18}F^-$. Ces types de stratégies *umpolung* ouvrent la voie à la synthèse de ^{18}F-fluoroayles neutres ou riches en électrons partant du $^{18}F^-$.

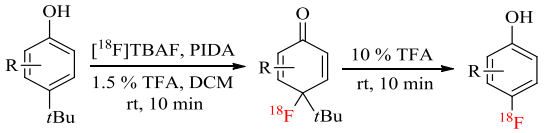

Schéma 1.15. ^{18}F-Fluorination oxydante de 4-*tert*-butyl-phénols.

1.2.3.5 Marquage de biomolécules par formation de liens ^{18}F-Si, ^{18}F-Al et ^{18}F-B

La formation directe de liens C-^{18}F au sein de biomolécules représente une approche généralement impraticable et l'utilisation de groupements prosthétiques aliphatiques ou aromatiques est largement exploitée mais souvent fastidieuse. Autrement, des méthodes douces de marquage direct générant des produits Si-^{18}F, B-^{18}F ou Al-^{18}F ont été développées.

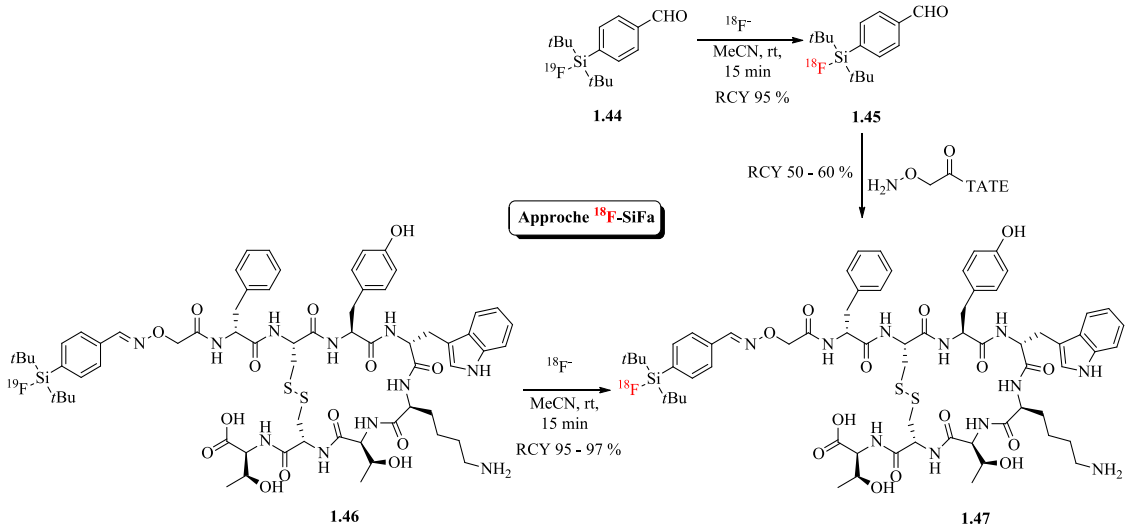

Schéma 1.16. Deux approches SiFA pour la synthèse d'un dérivé aminooxy de Tyr^3-octreotate (**1.46**).

En particulier, une méthodologie mise de l'avant par notre groupe, implique le marquage de biomolécules par échange isotopique d'un groupement de type fluorodi-*tert*-butylphenylsilane (SiFA; *silicon-based fluoride acceptor*) et permet la ^{18}F-fluorination efficace d'une large variété de précurseurs peptidiques complexes à température ambiante (Schéma 1.16).[56] La synthèse de biomolecules utilisant des ^{18}F-aryltrifluoroborates[57] et la complexation aluminium-fluorure (Al^{18}F)[58] constituent des approches alternatives prometteuses et sont illustrées au Schéma 1.17.

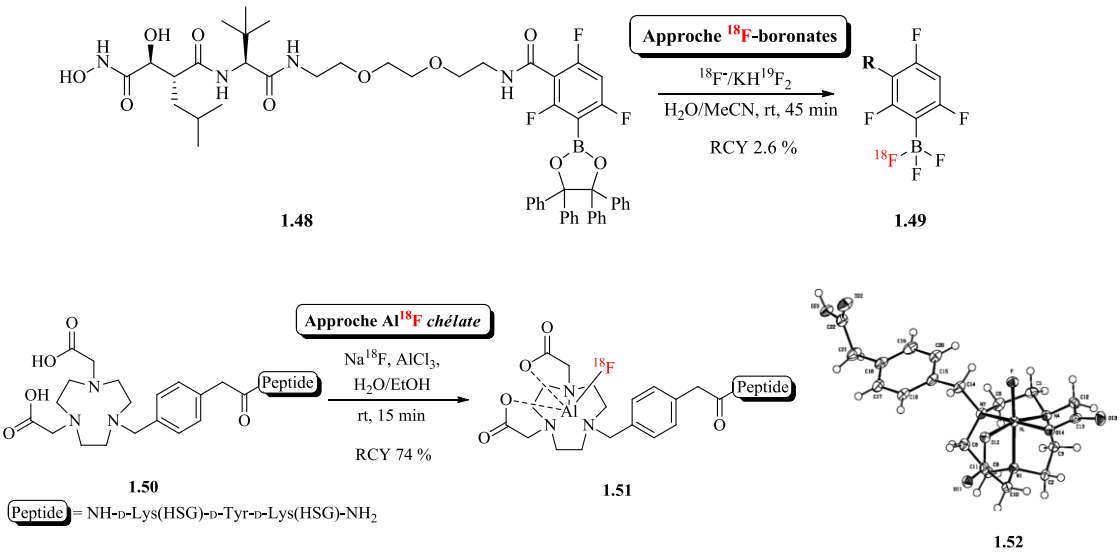

Schéma 1.17. Stratégies ^{18}F-aryltrifluoroborates et complexation Al-^{18}F pour la synthèse de biomolécules radiofluorées.

Parmi l'ensemble des techniques de radiomarquages présentées ici, celles utilisés avec succès dans ce mémoire sont les réactions de radiométhylation avec le [^{11}C]CH_3I et le [^{11}C]CH_3OTf de même que les radiofluorinations S_NAr.

1.3 Récepteurs TrkB tyrosine kinase et neurotrophines

1.3.1 Les neurotrophines

Les neurotrophines sont des facteurs de croissance essentiels régulant le développement, la survie, le fonctionnement de même que la plasticité du système nerveux.[59] A ce jour, quatre neurotrophines distinctes ont été identifiées et caractérisées chez les mamifères: le facteur de croissance du tissu nerveux (NGF, *nerve growth factor*), le facteur neurotrophique dérivé du cerveau (BDNF, *brain derived neurotrophic factor*), la neurotrophine 3 (NT-3) et la neurotrophine 4 (NT-4, aussi connu sous le nom de neurotrophine 5, d'où la nomenclature faisant parfois référence à NT-4/5).[60]

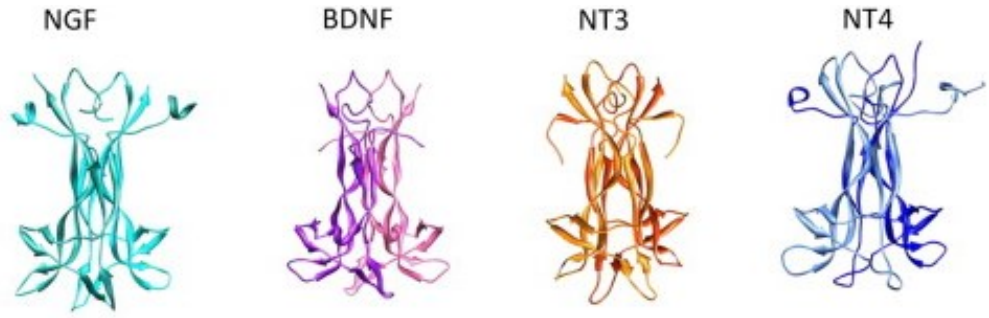

Figure 1.7. Structures cristallines des neurotrophines (homodimères). NGF est illustré en cyan (PDB 1WWW, NGF complexé à TrkA-*d*5); BDNF est illustré en mauve (homodimère issu d'une modélisation de PDB 1BND, BDNF-NT3 hétérodimère); NT-3 est illustré en orange (PDG 3BUK, NT/-p75NTR complexé); NT-4 (NT-4/5) est illustré en bleu (PDB 1HCF, NT4 complexé avec TrkB). (Adapté de Ref. 63).

Structurellement, ces neurotrophines sont des protéines dimériques présentant un haut degré de conservation qui, comme nombre de facteurs de croissance, sont sécrétées sous des formes *immatures* ici dites pro-neurotrophines (30-35 kDa), lesquelles sont clivées intra- ou extracellulairement en des formes plus courtes et matures (12-13 kDa) qui homodimérisent de manière non covalente.[61] Les neurotrophines et leurs récepteurs sont hautement exprimés au sein du système nerveux chez les vertébrés, mais aussi parmi de nombreuses populations cellulaires non neuronales.[62] Les structures cristallines des neurotrophines matures ont toutes été résolues et comprennent des caractéristiques structurelles communes telles que: trois paires de feuillets β antiparallèles reliées à

quatres tours β ainsi que trois ponts cystéines centraux (Figure 1.7). Dans ces structures, les feuillets β sont hautement homologiques et essentiels au maintien de la structure tertiaire de même qu'à la dimérisation. Par ailleurs, les résidus des régions N- et C-terminales de même que les tours sont nettement variables et conséquemmment, distinguent les différentes neurotrophines les unes des autres.[60b, 63]

1.3.2 La famille des récepteurs neurotrophiques et p75^{NTR}

Les neurotrophines et leurs formes pro-matures respectives interagissent avec deux types de récepteurs transmembranaires structurellement distincts: le récepteur p75^{NTR}, membre de la superfamille du facteur de nécrose tumorale, et les récepteurs à activité tyrosine kinase Trk (*tropomyosin receptor kinase*).

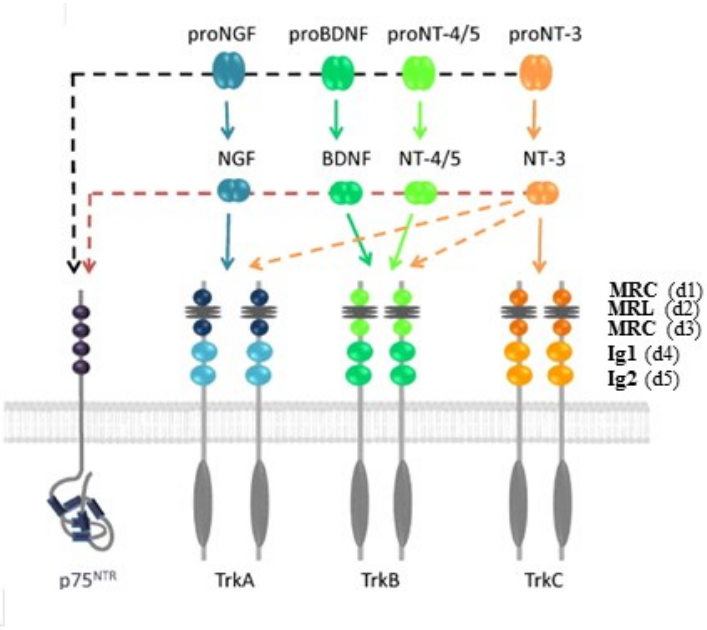

Figure 1.8. Spécificité de liaison des récepteurs neurotrophiques. Le récepteur p75NTR se lie à l'ensemble des neurotrophines (NGF, BDNF, NT-3, NT-4/5) de même que les proneurotrophines (proNGF, proBDNF, proNT-3, proNT-4/5). Les récepteurs Trk se lient avec différente spécificité au diverses neurotrophines. Les domaines extracellulaires des récepteurs Trk sont subdivisés en 5 sous-domaines caractéristiques: deux motifs riches en cystéines (MRC; d1 et d3) intercallés d'un modif riche en leucines (MRL; d2), deux domaines immunoglobulines (Ig1, Ig2; d4 et d5). (Adapté de Ref. 64).

D'une part, les effets neurotrophiques généralement favorables de ce système sont médiés via l'interaction sélective et partiellement spécifique de haute affinité ($K_d \approx 10^{-11}$ M) des formes matures vis-à-vis des récepteurs Trk; NGF se lie à TrkA, BDNF se lie à TrkB, NT-3 se lie à TrkC, mais aussi, NT-4 se lie à TrkB et NT-3 à TrkA quoique dans une moindre mesure (Figure 1.8).[64] L'interaction entre une neurotrophine et son récepteur Trk déclenche la dimerisation dudit récepteur suivi d'une transphosphorylation et de l'activation des cascades cellulaires qui en découlent. D'autre part, les neurotrophines se lient avec une affinité similaire ($K_d \approx 10^{-9}$ M) au récepteur $p75^{NTR}$ lequel est principalement lié à la promotion de l'apoptose.[60b] Le récepteur $p75^{NTR}$ est aussi impliqué dans la régulation des activités de différents récepteurs Trk.[65] Par ailleurs, des études récentes ont démontrées que les formes proneurotrophiques promeuvent aussi l'apoptose via des interactions de hautes affinités, spécifiques au récepteur $p75^{NTR}$.[66] Conséquemment, l'activation de cascades de signalisation aux effets diamétralement opposés découle d'un équilibre étroit dans l'expression des différentes formes de neurotrophines et de leurs récepteurs dans une population cellulaire donnée.

1.3.3 Récepteurs TrkB

Parmi l'ensemble des neurotrophines et de leurs récepteurs, le système BDNF-TrkB a été particulièrement investigué et associé à la survie neuronale, la différentiation cellulaire et la potentialisation à long terme (PLT).[59] Le domaine extracelullaire de TrkB présente cinq sous-domaines caractéristiques de l'ensemble des récepteurs Trk. Ces sous-domaines consistent en un motif riche en leucines (MRL, d2) intercallé entre deux motifs riches en cystéines (MRC, d1 et d3), suivi de deux domains immunoglobulines à plus grande proximité de la membrane cellulaire (Ig1, et Ig2, respectivement d4 et d5) (Figure 1.8).[60b] La structure tridimensionnelle précise du domaine extracellulaire de TrkB étant inconnue, les informations sur celle-ci doivent être dérivées de celle connue pour le récepteur TrkA,[67] dont la structure cristalline a été résolue, de même que le sous-domaine TrkB-d5 aussi connu.[68] D'ailleurs, une modélisation homologique de la partie extracellulaire de TrkB obtenue partant de ces informations est illustrée à la Figure 1.9A.[69]

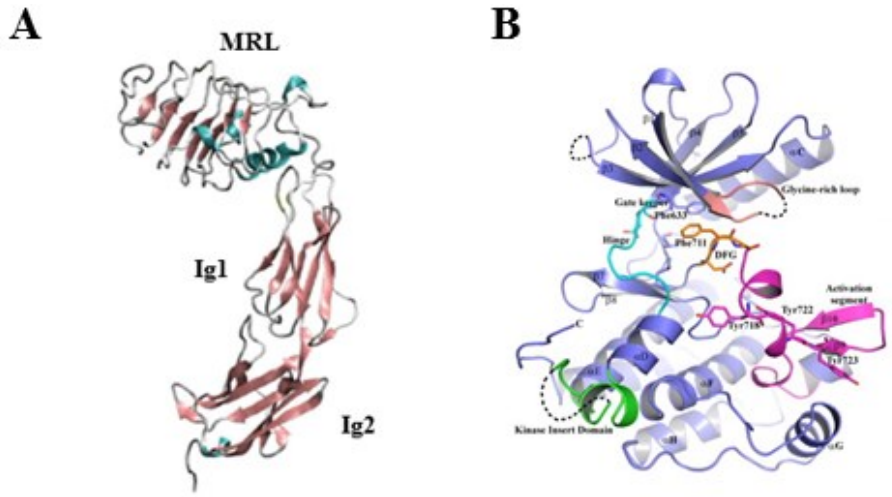

Figure 1.9. Structure du récepteur TrkB (A) Modélisation homologique du domaine extracellulaire de TrkB. La modélisation montre le motif riche en leucines (MRL) intercallé entre deux motifs riches en cystéines de même que les deux domaines immunoglobulines (Ig1 et Ig2). (Adapté de Ref. 68). (B) Structure cristalline du domaine intracellulaire de TrkB (monomère de apo-TrkB humain). Sont illustrés: segment d'activation (magenta), motif DFG (orange), *hinge region* (cyan), boucle riche en cystéines (rose), domaine KID (vert). Les résidus tyrosines pouvant être phosphorylés sont illustrés. (PDB 4ASZ) (Adapté de Ref. 69).

De plus, la structure cristalline du domaine à activité tyrosine kinase (domaine intracellulaire) a été résolue et comporte les éléments constitutifs classiques de ce type de domaine tel qu'un lobe N-terminal avec feuillets β prédominants et un lobe C-terminal avec hélices α prédominantes.[70] Dans l'ensemble, il s'agit d'une structure présentant un haut degré d'homologie avec les autres domaines intracellulaires Trk (*vide infra*). Aussi, en plus du récepteur TrkB entier combinant les domaines intra- et extracellulaires intacts illustrés ci-haut (TrkB-FL), des formes tronquées TrkB-T1 et TrkB-T2, dépourvues du domaine à activité tyrosine kinase cytoplasmique sont aussi exprimées dans une multitude de cellules. En interagissant avec BDNF sans activer de voies de signalisation neurotrophiques, ces récepteurs présentent une activité inhibitoire dominante négative face au TrkB-FL.[71]

1.3.4 Voies de signalisations cellulaires des récepteurs TrkB

L'activation des récepteurs Trk subséquente à la liaison des neurotrophines et à la phosphorylation de différents résidus tyrosines issus du domaine intracellulaire engage l'activation d'un nombre important de voies de signalisations intracellulaires fortement interreliées. En particulier, la phosphorylation de TrkB par BDNF (ou NT-4/5) active (1) la cascade de signalisation de la Ras/MAP kinase (MAPK) associée à la croissance et la différentiation neuronale, (2) la voie de la phosphatidylinositol-3 kinase (PI3-K) associée à la survie neuronale ef finalement, (3) la voie de la phospholipase Cγ (PLCγ) associée à la plasticité synaptique et la neurotransmission.[60a,72]

1.3.5 Implications pathologiques du dérèglement du système BDNF/TrkB

En tant que conséquence directe du rôle prédominant de TrkB et de son ligand endogène, BDNF, dans le développement et le maintien du système nerveux, des dérèglements, même légers, dans l'expression de ces protéines mènent à une multitude de conditions pathologiques. De fait, d'importantes corrélations entre une alteration des niveaux d'expression de BDNF et de son récepteur dans différentes régions cérébrales ont été caractérisées pour la maladie d'Alzheimer,[73] la maladie de Huntington,[74] la maladie de Parkinson,[75] le syndrome de Rett[76] de même que suivant un traumatisme crânien.[77] Une régulation négative du système TrkB/BDNF est aussi observée pour de nombreux désordres psychiatriques dont la schizophrénie[78] et la depression.[79] Par ailleurs, une surexpression de TrkB et BDNF est caractéristique d'autres maladies du SNC tel que l'épilepsie[80] mais plus particulièrement, retrouvée dans une multitude de cancers neuroendrociniens.[81] Le système TrkB/BDNF constitue donc une cible thérapeutique – et d'imagerie – de choix en neurologie et en oncologie.

1.3.6 Natures des interactions TrkB/BDNF et ciblage thérapeutique

Malheureusement, l'exploitation thérapeutique de BDNF s'avère hautement limitée par son faible profil pharmacologique. Ainsi, le développement de petites molécules exogènes se liant sélectivement à TrkB, agonistes ou antagonistes, est

reconnu comme un objectif hautement désirable depuis nombre d'années. Cette modulation est envisageable soit via le domaine intra- ou extracellulaire. La stratégie de modulation des récepteurs à activité tyrosine kinase implique typiquement le ciblage du domaine intracellulaire via le site de liaison de l'ATP soit de manière directe ou par modulation allostérique. Par contre, cette approche souffre de l'inconvénient d'être faiblement sélective en raison du haut degré de conservation de ce domaine dans l'ensemble du kinome.[82] En particulier, la structure cristalline du domaine intracellulaire des récepteurs TrkA, TrkB et TrkC et l'analyse de leur séquence démontrent que parmi les 40 résidus positionnés dans la région clé d'un point de vue thérapeutique, TrkA et TrkB sont identique à 95% alors que TrkB et TrkC sont entièrement identiques (Figure 1.11 (B)).[70] Ces résultats suggèrent que le développement de ligands du domaine kinase sélectif à TrkB risque d'être particulièrement complexe.

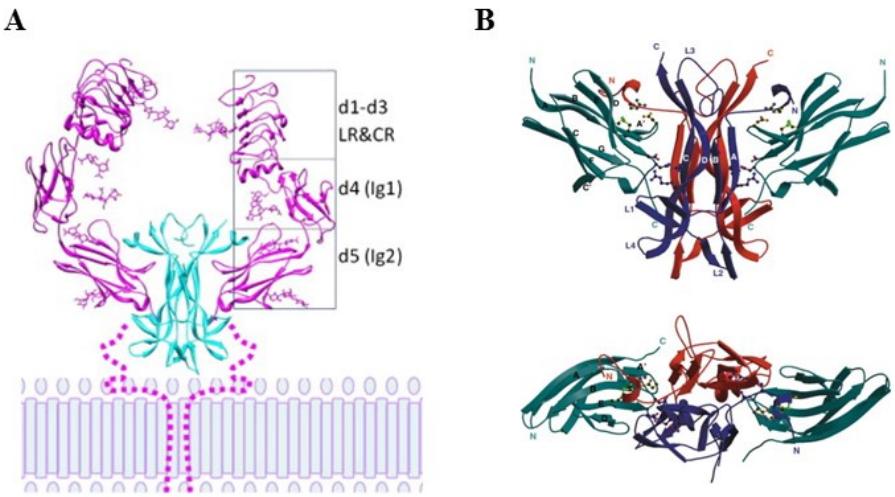

Figure 1.10. Interactions Trk-neurotrophines. (A) Structure crystalline du complexe TrkA (rose) –NGF (cyan) (PDB 2IFG). Le sous-domaine d5 constitue le principal point de liaison entre le récepteur TrkA et NGF. (B) Structure du complexe TrkB-d5 – NT-4/5. Un homodimère NT-4/5 (rouge et bleu) est lié à deux monomères de TrkB-d5 (vert) (PDB 1HCF). (Adapté des Ref. 63 et 68).

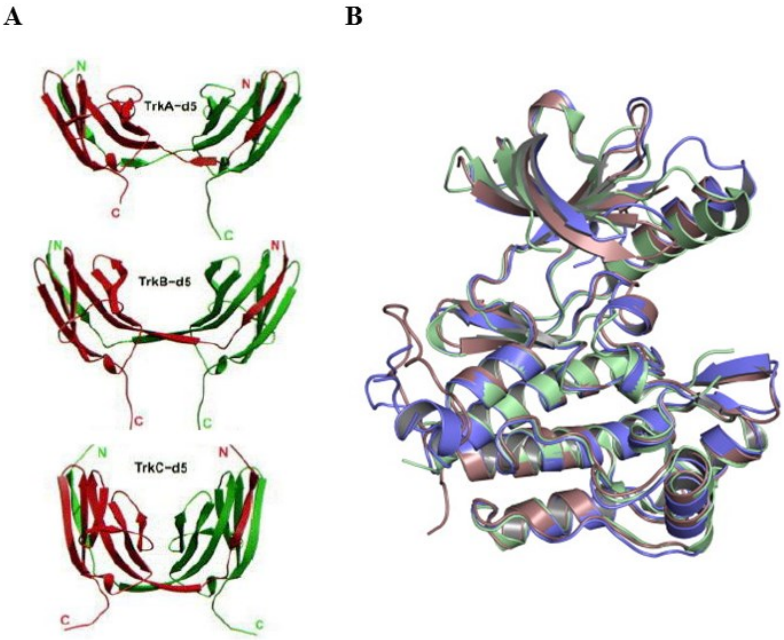

Figure 1.11. (A) Structrure des différents domaines Trk-d5. (B) Superposition de la structure de apo-TrkA (bronze) avec apo-TrkB (bleu) et TrkC (vert; PDB 3V5Q) (Adapté de la Ref. 69).

La stratégie alternative implique le ciblage du domaine extracellulaire dans la mesure où il est possible de déterminer des régions clés impliquées dans l'interaction de TrkB avec ses ligands endogènes. Pendant plusieurs années, le développment de ligands ciblant ce domaine s'est vu limité par l'absence de données cristallographiques du complexe homodimérique entier TrkB-BDNF. Néanmoins, les informations obtenues de la structure cristalline pour TrkA-NGF et TrkB-d5 en complexe avec BDNF (Figure 1.10) ont permis de formuler l'hypothèse voulant que la liaison du sous-domaine d5 de TrkB avec différents résidus issus des tours et de la région N-terminal de BDNF constitue le point d'encrage principal à l'origine de l'interaction et de la spécificité de liaison entre TrkB et BDNF. Aussi, cette hypothèse est supportée par l'évaluation et l'analyse de protéines de fusion et de délétions.[82] De plus, le sous domaine d5 présente une activité auto-inhibitoire vis-à-vis la dimérisation spontannée des récepteurs, ce qui supporte plus avant l'idée voulant que ce sous-domaine soit un point clé dans l'activation de TrkB.[83] Les structures cristallines des domaines d5 de TrkA, TrkB et TrkC suggèrent aussi des differences structurelles suffisantes pour que le design de ligands mimant l'interaction entre BDNF et TrkB-d5 soit sélectif (Figure 1.12 (A)). De fait, le ciblage du domaine

extracellulaire de TrkB a permis récemment l'identification de petits peptides puis de petites molecules non-peptidiques modulatrices de TrkB (Figure 1.12).

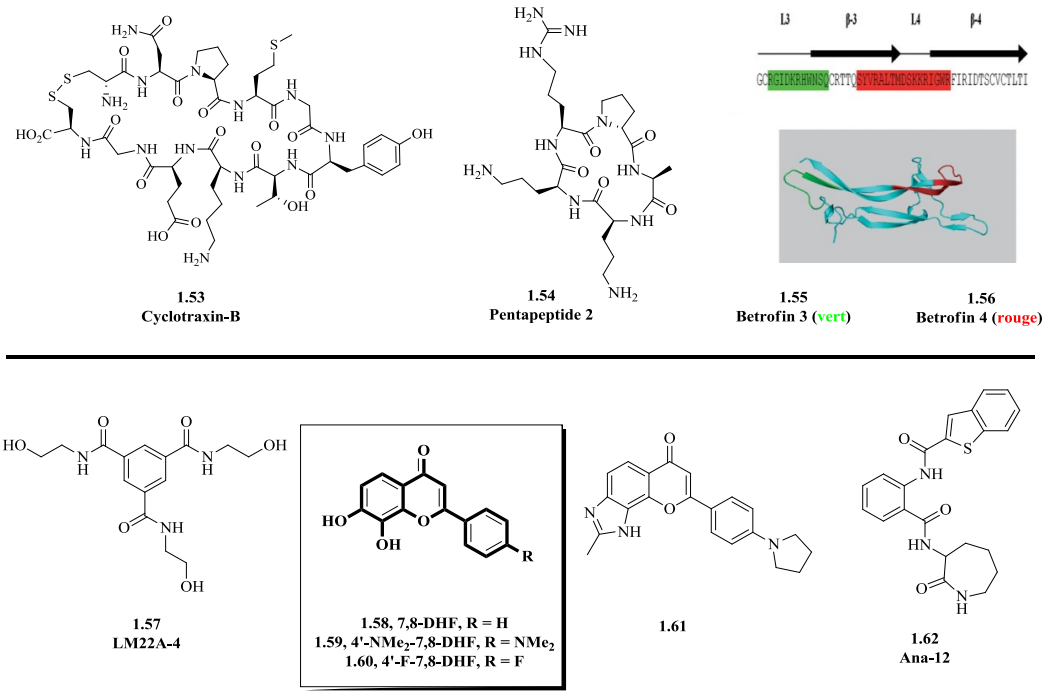

Figure 1.12. Structures des ligands ciblant les récepteurs TrkB.

Par contre, les peptides développés (**1.53-1.56**) en tant que mimes de différentes régions de BDNF sont sensibles à la protéolyse et, malgré leurs activités favorables vis-à-vis TrkB *in vitro*, constituent des agents thérapeutiques dont l'application *in vivo* est limitée.[84] Par ailleurs, des ligands non peptidiques de faible poids moléculaire et de haute affinité face à TrkB (**1.57-1.62**) ont aussi été développés dans les trois dernières années, ouvrant ainsi la voie à des thérapies novatrices pour différents désordres neurologiques et cancers. Les composés LM22A-4[85] (**1.57**) et ANA-12[86] (**1.62**), obtenus par criblage *in silico* de fragments de BDNF ont été caractérisés comme agoniste et antagoniste de TrkB respectivement. Ces composés sont sélectifs à TrkB et présentent des affinités nanomolaires dans différents modèles cellulaires. Par contre, les ligands les plus prometteurs et les mieux caractérisés depuis leur publication initiale sont les dérivés du 7,8-dihydroxyflavone (**1.58-1.61**). Ainsi, le 7,8-dihydroxyflavone (**1.58**), initialement reporté comme agoniste de TrkB ($K_d \approx 300$ nM) dans des modèles cellulaires corticales

et hippocampales, agit comme un mime de BDNF dans des modèles animaux d'excitotoxicité et de maladie de Parkinson, et a été depuis validé dans une multitude d'autres modèles *in vitro* et *in vivo*.[87] De plus, l'optimisation de **1.58** a permis le développement des dérivés **1.59**, **1.60** et **1.61** présentant une affinité et une efficacité supérieure au composé initial.[88]

1.4 Objectif du projet

Ainsi, dans la foulée du développement récent de ligands non peptitiques sélectifs au récepteur TrkB, et attendu le nombre important de pathologies associées à un dérèglement du système BDNF/TrkB, nous avons entrepris un nouveau projet de recherche destiné au développement des premiers radiotraceurs ligands de TrkB pour l'imagerie TEP. Plus spécifiquement, ce mémoire détaille mes travaux ayant menés à la radiosynthèse et l'évaluation d'une première génération de traceurs TEP inspirés du 7,8-dihydroxyflavone, marqués au carbone-11 et au fluor-18, ultimement destinés à l'évaluation *in vivo* des récepteurs TrkB.

1.5 Notes et références

1. Voir par exemple: Saha, G. B. Basics of PET imaging, 2nd ed., Springer, New York, 2010.
2. Jones, T. *Eur. J. Nucl. Med.* **1996**, *23*, 807-813.
3. Miller, P. W.; Long, N. J.; Vilar, R.; Gee, A. D. *Angew. Chem. Int. Ed.* **2008**, *47*, 8998-9033.
4. Price, P. *Trends in Molecular Medicine*. **2001**, *7*, 442-446.
5. Massoud, T. F.; Gambhir, S. S. *Genes Development*. **2003**, *17*, 545-580.
6. Moses, W. W. *Nucl. Instrum. Methods Phys. Res. A*. **2011**,648 Suppl. 1: S236–S240.
7. Pour une introduction sur les aspects physique de l'émission de positon voir: (a) Cherry, S. R.; Dahlbom, M. PET: Physics, instrumentation, and scanners, Springer, New York, 2006. (b) Saha, G. B. Radioactive decay and interaction of radioation with matter, in Ref. 1.
8. Li, Z.; Conti, P. S. *Advanced Drug Delivery Reviews*. **2010**, *62*, 1031-1051.
9. Gómez-Vallejo, V. Development of New Strategies for the Synthesis of Radiotracers Labeled with Short-Lived Isotopes: Application to ^{11}C and ^{13}N. Ph.D. Thesis. Ramon Llull University. http://www.cicbiomagune.es/uploads/doc/phdthesis/Vanessa_Gomez_Vallejo.pdf
10. Wadas, T. J.; Wong, E. H.; Weisman, G. R.; Anderson, C. J. *Chem. Rev*. **2010**, *110*, 2858-2902.
11. (a) Ido, T.; Wan, C.-N.; Casella, V.; Fowler, J. S.; Wolf, A. P. *J. Label. Compd. Radiopharm*. **1978**, *14*, 175-183. (b) Gallagher, B. M.; Fowler, J. S.; Gutterson, N. I.; MacGregor, R. R.; Wan, C.-N.; Wolf, A. P. *J. Nucl. Med*. **1978**, *19*, 1154-1161.
12. Hamacher, K.; Coenen, H. H.; Stocklin, G. *J. Nucl. Med*. **1986**, *27*, 235-238.
13. Santra, A.; Kumar, R.; Sharma, P.; Bal, C.; Kumar, A.; Julka, P. K.; Malhotra, A. *Eur. J. Radiol.* **2012**, *81*, 508-513.

14. Pour des revues, voir: (a) Matthews, P. M.; Rabiner, E. A.; Passchier, J.; Gunn, R. N. *Br. J. Clin. Pharmacol*. **2012**, *73*, 175-186. (b) Lee, C.-M.; Farde, L. *Trends Pharm. Sci.* **2006**, *27*, 310-316. (c) Wong, D. F.; Tauscher, J.; Grunder, G. *Neuropsychopharmacology* **2009**, *34*, 187-203.
15. Pike, V. W. *Trends Pharm. Sci.* **2009**, *30*, 431-440.
16. Laruelle, M.; Slifstein, M.; Huang, Y. *Mol. Imaging Biol*. **2003**, *5*, 363-375.
17. (a) Mintun, M. A.; Raichle, M. E.; Kilbourn, M. R.; Wooten, G. F.; Welch, M. J. *Ann Neurol.* **1984**, *15*, 217-227. (b) Innis, R.B.; Cunningham, V. J.; Delforge, J.; Fujita, M.; Gjedde, A.; Gunn, R. N.; Holden, J.; Houle, S.; Huang, S. C.; Ichise, M.; Iida, H.; Ito, H.; Kimura, Y.; Koeppe, R. A.; Knudsen, G. M.; Knuuti, J.; Lammertsma, A. A.; Laruelle, M.; Logan, J.; Maguire, R. P.; Mintun, M. A.; Morris, E. D.; Parsey, R.; Price J. C.; Slifstein, M.; Sossi, V.; Suhara, T.; Votaw, J. R.; Wong, D. F.; Carson, R. E. *J Cereb Blood Flow Metab.* **2007**, *27*, 1533-1539.
18. Ichise, M.; Meyer, J. H.; Yonekura, Y. *J. Nucl. Med*. **2001**, *42*, 755-763.
19. Pardridge, W. M. *Mol. Interv*. **2003**, *3*, 90-105.
20. (a) Malakoutikhah, M.; Teixido, M.; Giralt, E. *Angew. Chem. Int. Ed.* **2011**, *50*, 2-19; (b) Cecchelli, R.; Berezowski, V.; Lundquist, S.; Culot, M.; Renftel, M.; Dehouck, M.-P.; Fenart, L. *Nature Reviews Drug Discovery* **2007***, 6*, 650-661.
21. Scott, P. J. H. *Angew. Chem. Int. Ed.* **2009**, *48*, 6001-6004.
22. Bolton, R. *J. Labelled Compd. Radiopharm*. **2001**, *44*, 701-736.
23. Klunk, W. E.; Engler, H.; Nordberg, A.; Wang, Y.; Blomqvist, G.; Holt, D. P., Bergstrom, M.; Savitcheval, I.; Huang, G. F.; Estrada, S.; Ausen, B.; Debnath, M. L.; Barletta, J.; Price, J. C.; Sandell, J.; Lopresti, B. J.; Wall, A.; Koivisto, P.; Antoni, G.; Mathis, C. A.; Langstrom, B. *Ann. Neurol*. **2004**, *55*, 306-319.
24. Ng, S.; Villemagne, V. L.; Berlangieri, S.; Lee, S.-T.; Cherk, M.; Gong, S. J.; Ackermann, U.; Saunder, T.; Tochon-Danguy, H.; Jones, G.; Smith, C; O'Keefe, G.; Masters, C. L.; Rowe, C. C. *J. Nucl. Med*. **2007**, *48*, 547-552.
25. Mathis, C. A.; Wang, Y.; Holt, D. P.; Huang, G.-F.; Debnath, M. L.; klunk, W. E. *J. Med. Chem*. **2003**, *46*, 2740-2754.

26. Pour une revue: Pretze, M.; Grobe-Gehling, P.; Mamat, C. *Molecules*, **2011**, *16*, 1129-1165.
27. Hostetler, E. D.; Terry, G. E.; Burns, H. D. *J. Labelled Compd. Radiopharm*. **2005**, *48*, 629-634.
28. Wuest, F.; Zessin, J.; Johannsen, B. *J. Labelled Compd. Radiopharm*. **2003**, *46*, 333-342.
29. Björkman, M.; Doi, H.; Resul, B.; Suzuki, M.; Noyori, R.; Watanabe, Y.; Langstrom, B. *J. Labelled Compd. Radiopharm*. **2000**, *43*, 1327-1334.
30. Wuest, F.; Berndt, M. *J. Labelled Compd. Radiopharm*. **2006**, *49*, 91-100.
31. .McCarron, J. A.; Turton, D. R.; Pike, V. W.; Poole, K. G. *J. Labelled Compd. Radiopharm*. **1996**, *38*, 941-953.
32. Borg, J. *Behavioural Brain Res*. **2008**, *195*, 103-111
33. Van Tilburg, E. W.; Windhorst, A. D.; Va der Mey, M.; Herscheid, J. D. M. *J. Labelled Compd. Radiopharm*. **2006**, *49*, 321-330.
34. Hooker, J. M.; Reibel, S. M. Hill, S. M.; Scueller, M. J.; Fowler, J. S. *Angew. Chem. Int. Ed.* **2009**, *48*, 6482-3485.
35. Riss, P. J.; Lu, S. Telu, S.; Aigbirhio, F. I.; Pike, V. W. *Angew. Chem. Int. Ed.* **2012**, *51*, 2698-2702.
36. Roeda, D.; Dollé, F. *Curr. Topic Med. Chem*. **2010**, *10*, 1680-1700.
37. Ponchant, M.; Hinnen, F.; Demphel, S.; Crouzel, C. *Appl. Radiat. Isot*. **1997**, *48*, 755-762.
38. Gillings, N. M.; Gee, A. D. *J. Labelled Compd. Radiopharm*. **2001**, *44*, 909-920.
39. Sandell, J.; Halldin, C.; Thorberg, S.-O.; Werner, T.; Sohn, D.; Sedvall, G.; Farde, L. *Nucl. Med. Biol*. **1999**, *26*, 159-164.
40. Pour une revue: Langstrom, B.; Itsenko, O.; Rahman, O. *J. Labelled Compd. Radiopharm*. **2007**, *50*, 794-810.
41. Hostetler, E. D. Burns, H. D. *Nucl. Med. Biol*. **2002**, *29*, 845-848.
42. Rahman, O.; Kihlberg, T. Langstrom, B. J. *Chem. Soc. Perkin Trans I* **2002**, 2699-2703.
43. 0.0397% de CO_2 versus 0.00001% de CO dans l'air.

44. (a) Iwao Ojima Ed. Fluorine in Medicinal Chemistry and Chemical Biology, Wiley, Hoboken 2009. (b) Meanwell, N. A. *J. Med. Chem*. **2011**, *54*, 2529-2591.
45. Dollé, F.; Helfenbein, J.; Hinnen, F.; Mavel, S.; Mincheva, Z.; Saba, W.; Schollhorn-Peyronneau, M. A.; Valette, H.; Garreau, L.; Chalon, S.; Halldin, C.; Madelmont, J. C.; Deloye, J. B.; Bottlaender, M.; Le Gailliard, J.; Guilloteau, D.; Emond, P. *J. Labelled Compd. Radiopharm*. **2007**, *50*, 716-723.
46. Yun, M.; Oh, S. J.; Ha, H.-J.; Ryu, J. S.; Moon, D. H. *Nucl. Med. Biol*. **2003**, *30*, 151-157.
47. Lu, S.; Giamis, A.; Matteo, J.; Pike, V. *J. Nucl. Med*. **200**, *49* (Supplement 1), 46.
48. Ahmed, N.; Langlois, R.; Radrigue, F.; Bernard, F.; van Lier, J. E. *Nucl. Med. Biol.* **2007**, *34*, 459-464.
49. Tredwell, M.; Gouverneur, V. *Angew. Chem. Int. Ed*. **2012**, *51*, 2-14.
50. Massaweg, G.; Schirrmacher, E.; la Fougere, C.; Kovacevic, M.; Wangler, C.; Jolly, D.; Gravel, P.; Reader, A. J.; Thiel, A.; Schirrmacher, R. *Nucl. Ed. Biol*. **2009**, *36*, 721-727.
51. Moon, B. S.; Kil, H. S.; Park, J. H.; Kim, J. S.; Park, J.; Chi, D. Y.; Lee, B. C.; Kim, S. E. *Org. Biomol. Chem*. **2011**, *9*, 8346-8355.
52. (a) Forsback, S.; Eskola, M.; Bergman, J.; Haaparanta, M.; Solin, O. *J. Labelled Compd. Radiopharm*. **2009**, *52*, 286-288. (b) Forsback, S.; Eskola, M.; Haaparanta, M.; Bergman, J.; Solin, O. *Radiochim. Acta* **2008**, *96*, 845-848.
53. Teare, H.; Robins, E. G.; Kirjavainen, A.; Forsback, S.; Sandford, G.; Solin, O.; Luthra, S. K.; Gouverneur, V. *Angew. Chem. Int. Ed*. **2010**, *49*, 6821-6824.
54. Lee, E.; Kamlet, A. S.; Pwers, D. C.; Neumann, C. N.; Boursalian, G. B.; Furuya, T.; Choi, D. C.; Hooker, J. M.; Ritter, T. *Science*, **2011**, *334*, 639-642.
55. Gao, Z.; Lim, Y. H.; Tredwell, M.; Li, L.; Verhoog, M.; Hopkinson, M.; Kaluza, W.; Collier, T. L.; Passchier, J.; Huiban, M.; Gouverneur, V. *Angew. Chem. Int. Ed*. **2012**, *51*, 6733-6737.
56. Schirrmacher, R.; Bradtmoller, G.; Schirrmacher, E.; Thews, O.; Tillmanns, J.; Siessmeier, T.; Buchholz, H. G.; Bartenstein, P.; Wangler, B. Niemeyer, C. M.; Jurkschat, K. *Angew. Chem. Int. Ed*. **2006**, *45*, 6047-6050.

57. Perrin, D.; Li, Y.; Ting, R.; auf dem Keller,U.; Bellac, C.; Lange, P.; Schaffer, P.; Benard, F.; Overall, C.; Ruth, T. J. Nucl. Med. 2012, 53, (Suppl. 1), 58, 1140.
58. D'Souza, C. A.; McBride, W. J.; Sharkey, R. M.; Todaro, L. J.; Goldengerg, D. M. *Bioconjugate Chem*. **2011**, *22*, 1793-1803.
59. Huang, E.; Reichardt, L. F. *Annu. Rev. Neurosci*. **2001**, *24*, 677-736.
60. (a) Lee, F. S.; Kim, A. H.; Khursigara, G.; Chao, M. V. *Curr. Opin. Neurobiol*. **2001**, *11*, 281-286. (b) Pattarawaparan, M.; Burgess, K. *J. Med. Chem.* **2003**, *49*, 5277-5291.
61. (a) Seidah, N. G.; Benjannet, S.; Pareek, S.; Chretien, M.; Murphy, R. A. *FEBS Lett*. **1996**, *379*, 247-250. (b) Lu, B.; Pang, P. T.; Woo, N. H. *Nature Rev. Neurosci.* **2005**, *6*, 603-614.
62. Teng, K. K.; Hempstead, B. L. *Cell. Mol. Life Sci*. **2004**, *61*, 35-48.
63. Allen, S. J.; Watson, J. J.; Shoemark, D. K.; Barua, N. U.; Patel, N. K. *Pharmacology and Therapeutics* **2013**, *138*, 155-175.
64. Hondermarck, H. *Cytokine & Growth Factor Rev.* **2012**, *23*, 357–365.
65. Vesa, J.; Kruttgen, A.; Shooter, E.M. *J. Biol. Chem.* **2000**, *275*, 24414-24420.
66. Lee, R.; Kermani, P.; Teng, K. K.; Hempstead, B. L. *Science*, **2001**, *294*, 1945-1948.
67. Wehrman, T.; He, X.; Raab, B.; Dukipatti, A.; Blau, H.; Garcia, K. C. *Neuron* **2007**, *53*, 25-38.
68. Banfield, M. J.; Naylor, R. L.; Robertson, A. G.; Allen, S. J.; Dawbarn, D.; Brady, R. L. *Structure* **2001**, *12*, 1191-1199.
69. Liu, X.; Chan, C.-B.; Qi, Q.; Xiao, G.; Luo, H. R.; He, X.; Ye, K. *J. Med. Chem*. **2012**, *55*, 8524-8537.
70. Bertrand, T.; Kothe, M.; Liu, J.; Dupuy, A.; Rak, A.; Berne, P. F.; Davis, S.; Gladysheva, T.; Valtre, C.; Crenne, J. Y.; Mathieu, M. *J. Mol. Biol*. **2012**, *423*, 439-453.
71. Eide, F. F.; Viing, E. R.; Eide, B. L.; Zang, K.; Wang, X. Y.; Reichardt, L. F. *J. Neurosci*. **1996**, *16*, 3123-3129.
72. Boulle, F.; Kenis, G.; Carzola, M.; Hamon, M.; Steinbush, H. W. M.; Lanfumey, L.; van den Hove, D. L. A. *Prog. Neurobiol*. **2012**, *98*, 197-206.

73. Schindowski, K.; Belarbi, K.; Buee, L. *Genes Brain Behav.* **2008**, *7 (suppl 1)*, 43-56.

74. Zuccato, C.; Cuttaneo, E. *Prog. Neurobiol*. **2007**, *81(5-6)*, 294-330.

75. Fumagalli, F.; Racagni, G.; Riva, M. A. *Pharmacogenomics* **2006**, *6(2)*, 95-104.

76. Deng, V.; Matagne, V.; Banine, F.; Frerking, M.; Ohliger, P.; Budden, S.; Pevsner, J.; Dissen, G. A.; Sherman, L. S.; Ojeda, S. R. *Hum. Mol. Genet*. **2007**, *16*, 640-650.

77. Griesbach, G. S.; Hovda, D. A.; Gomez-Pinilla, F. *Brain Res.* **2009**, *1288*, 105-115.

78. Pillai, A. *Neurosignals*. **2008**, *16*, 183-193.

79. Li, Y.; Luikart, B. W.; Birnbaum, S.; Chen, J. ;l Kwon, C. H.; Kernie, S.; G.; Bassel-Duby, R.; Parada, L. F. *Neuron* **2008**, *59*, 399-412.

80. Wang, Y.; Qi, J. S.; Sun, Y.; Fan, J.; jiang, M.; Chen, G. *Neuropharmacology* **2009**, *57*, 49-59.

81. (a) Brodeur, G. M.; Minturn, J. E.; Ho, R.; Simpson, A. M.; Iyer, R.; Varela, C. R.; Light, J. E.; Kolla, V.; Evans, A. E. *Clin Cancer Res* **2009**, *15*, 3244-3250. (b) Sclabas, G. M.; Fujioka, S.; Schmidt, C.; Li, Z.; Frederick, W. A.; Yang, W.; Yokoi, K.; Evans, D. B.; Abbruzzese, J. L.; Hess, K. R.; Zhang, W.; Fidler, I. J.; Chiao, P.J. *Clin. Cancer Res*. **2005**, *11*, 440–9.

82. Khang, J.; Yang, P. Gray, N. S. *Nat. Rev. Cancer* **2009**, *9*, 28-39.

83. Arevalo, J. C.; Conde, B.; Hempstead, B. I.; Chao, M. V.; Martin-Zanca, D.; Perez, P. *Oncogene*, **2001**, *20*, 1229-1234.

84. (a) Carzola, M.; Jouvenceau, A.; Rose, C.; Guilloux, J. P.; Pilon, C.; Dranovszy, A.; Premont, J. *PLos One*, **2010**, e9777. (b) Fletcher, J. M.; Morton, C. J.; Zwar, R. A.; Murray, S. S.; O'Leary, P. D.; Hughes, R. A. *J. Biol. Chem*. **2008**, *283*, 33375-33383. (c) Fobian, K.; Owczarek, S.; Budtz, C.; Bock, E.; Berezin, V.; Pederse, M. V. *J. Neurosci. Res*. **2009**, *88*, 1170-1181.

85. Massa, S. M.; Yang, T.; Xie, Y.; Shi, J.; Bilgen,M.; Joyce, J. N.; Nehama, D.; Rajadas, J.; Longo, F. M. *J. Clin. Invest*. **2010**, *120*, 1774-1785.

86. Carzola, M.; Premont, J.; Mann, A.; Girard, N.; Kellendonk, C.; Rognan, D. *J. Clin. Invest*. **2011**, *121*, 1846-1857.

87. Par exemple: (a) Andero, R.; Daviu, N.; Escorihuela, R. M.; Nadal, M.; Armario, A. *Hippocampus*, **2010**, *23*, 399-408. (b) Andero, R.; Heldt, S. A. Ye, K.; Liu, X.; Armario, A.; Ressler, K. J. *Am. J. Psychiatry*, **2011**, *168*, 163-172. (c) Devi, L.; Ohno, M. *Neuropsychopharmacology*, **2012**, *37*, 434-444.

88. Liu, X.; Chan, C.-B.; Qi, Q.; Xiao, G.; Luo, H. R.; He, X.; Ye, K. *J. Med. Chem*. **2012**, *55*, 8524-8537.

Chapter 2

Introduction to ^{18}F- and ^{11}C-Labeled 7,8-Dihydroxyflavones as Tropomyosin-Related Kinase B (TrkB) Receptor Antagonists for Brain Imaging with Positron Emission Tomography

2.1 Introduction

Flavonoids are phenylpropanoids ubiquitous in nature and are associated with beneficial effects for a range of pathologies such as cancer, numerous infectious conditions and neurodegenrerative diseases.[1-3] Health benefits and biological actitivites of flavonoids have traditionally been viewed in the light of their generally well-characterized capacity to scavenge reactive oxygen species (ROS – antioxidant properties) despite limited understanding of the precise redox mechanism involved at the cellular level. However, multiple natural and synthetic flavonoids, including various flavone-type compounds, have also been investigated for their signaling properties and chemically derivatized in a therapeutic-oriented perspective (see Chapter 4).[1,4]

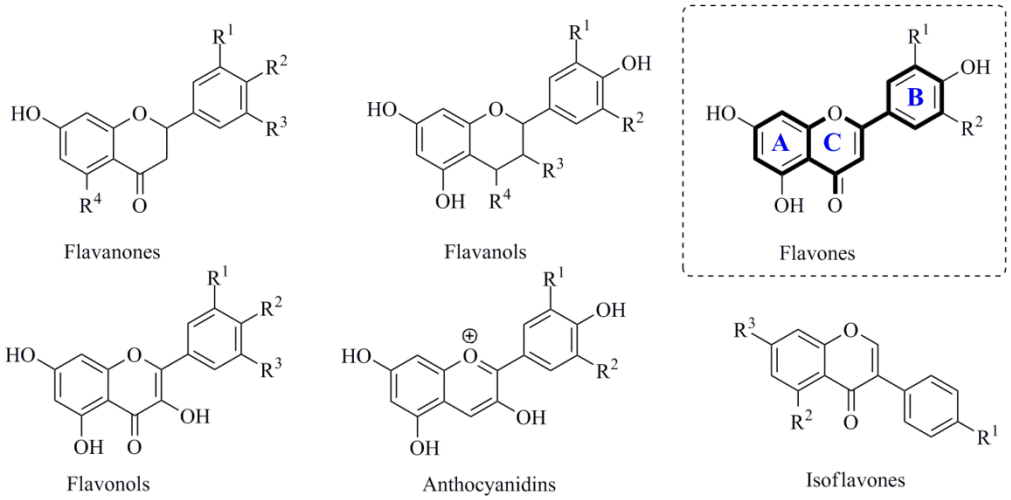

Figure 2.1. Representative structures of selected classes of naturally occurring flavonoids: flavanones, flavanols, flavones, flavonols, anthocyanidins and isoflavones (R group are OH or OMe).

This class of plant secondary metabolites encompass significant structural diversity and is usually associated with the C_6-C_3-C_6 carbon scaffold – phenylbenzopyran – with different hydroxy and methoxy substitutions. With respect to the position of the benzopyran (ring A and C) relative to the phenyl (ring B) and the oxidation level and hydroxylation of the C ring, flavonoids are divided in major subclasses – few of which are depicted in figure 2.1. Flavonoids also comprise compounds lacking the flavan core with either an open or compressed C ring such as chalcones or aurones respectively. To

date, more than 8000 natural derivatives of the polyphenolic flavonoid type have been identified and it is estimated that the daily uptake from dietary sources in the United States is about 1g per day mostly from vegetables, fruits, nuts and beverages such as tea.[5,6] Most flavonoids from dietary sources exist as β-glycosides and must undergo deglycosylation prior to absorption *in vivo*.[7] Plasma concentrations of those flavonoid aglycones are, under normal circumstances, very low owing to extensive phase II metabolism. This aspect will be discussed in detail in the next two chapters.

2.2 Flavone synthesis

2.2.1 Biosynthetic pathway of flavones derivatives

Irrespective of their carbon skeleton and substituent differences, all classes of dietary flavonoids share a general chalcone precursor biosynthetically derived from phenylalanine via phenylpropanoid metabolism and chalcone synthase (CHS) catalysis. More specifically, flavones are obtained via the subsequent conversion of chalcones intermediates to flavanones catalyzed by chalcone isomeraze (CHI) and to flavones through by flavone synthase (FNS) catalyzed dehydration.[8]

2.2.2 Synthetic approaches towards the flavone scaffold

Several approaches have been devised toward the synthesis of the flavone carbon framework (Scheme 2.1). Classical reactions sequences such as the Baker-Venkataraman rearrangement/acid-promoted cylization[9] and the Allan-Robinson reaction[10] involving the cyclization of β-diketone intermediates obtained via base-promoted acyl transfert from α-acyloxyketones and from acylation with functionalyzed anhydrides, have been exploited from nearly a century in flavone synthesis. Of those two reactions, the former is still widely utilized with numerous variations despite requiring harsh reaction conditions such as strong bases and acids, high temperatures.[11]

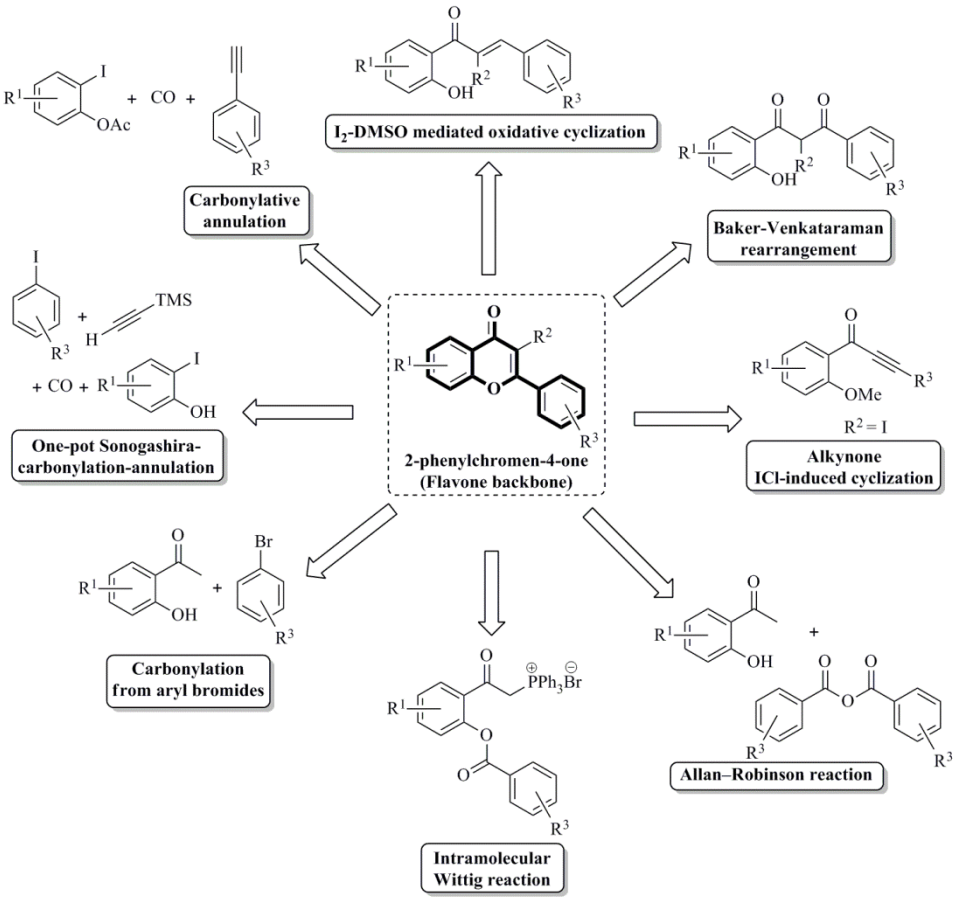

Scheme 2.1. Major strategies for the synthesis of 2-phenylchromen-4-one derivatives (flavone carbon framework).

Various milder reactions have also been developed. ICl-induced cyclization from alkynone precursors was demonstrated to be efficient but limited to the synthesis of 3-iodoflavones.[12] One-pot syntheses converting 2-hydroxyacetophenone to flavone promoted with mild bases[13] and intramolecular Wittig reactions from acylphosphoranes[14], either thermally or photochemically, were also shown to be efficient for a limited number of substrates. In addition, palladium-catalyzed carbonylation/cyclization reactions represent an attractive alternative toward the flavone ring system. Carbonylation procedures reacting 2-iodophenols with terminal acetylenes,[15] aryl bromides with 2-hydroxyacetophenones[16] or one-pot Sonogashira-carbonylation-annulation reactions[17] have been developed but, notwithstanding being relatively mild, suffer from the necessity of pressurized carbon monoxide in

combination with high temperature. Moreover, those reactions often require expensive phosphine ligands. The use of Claisen condensation/iodine catalyzed oxidative cylisation in DMSO has found broad applicability.[18] Synthetically, this reaction sequence finds advantage in using simple substituted benzaldehydes – largely available from commercial sources – and is normally a high yield reaction. A plausible mechanism for this iodine catalyzed oxidative cyclization is illustrated in Scheme 2.2.

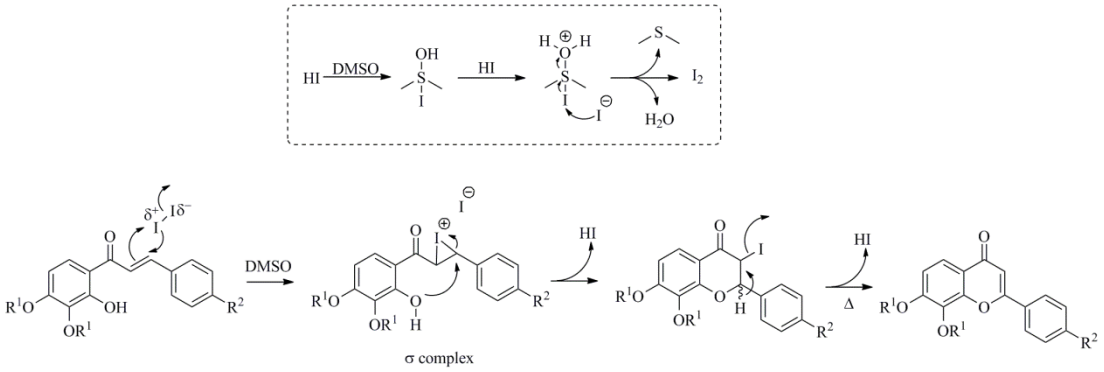

Scheme 2.2. Proposed mechanism for the I_2-catalyzed oxidative cyclization of chalcones to flavones with DMSO.

The intramolecular attack of a cyclic iodonium generated with catalytic iodine initially forms the 3-iodoflavonone intermediate. This is followed by the thermally promoted dehydroiodination leading to the flavone skeleton. Far from being accessory, the use of DMSO in this reaction is crucial. Correspondingly, DMSO oxidizes hydroiodic acid in a two steps sequence which regenerates the catalytic amount of iodine.[19]

2.3 Radiolabeling strategies of flavonoid-based PET imaging probes

Common radiolabeling strategies devised for flavonoid-type compounds – which have been essentially dedicated to Aβ peptide imaging – comprises: (1) complexation (^{99m}Tc; SPECT),[20] radioiodination (^{125}I; binding studies),[21] methylation (^{11}C; PET) [22] and S_N2 radiofluorination (^{18}F; PET. Figure 2.2).[22,23] Radiomethylation with $^{11}CH_3OTf$ or $^{11}CH_3I$ has been efficiently carried out from appropriate *des*-methyl precursors (**2.3**, figure 2.2).[22]

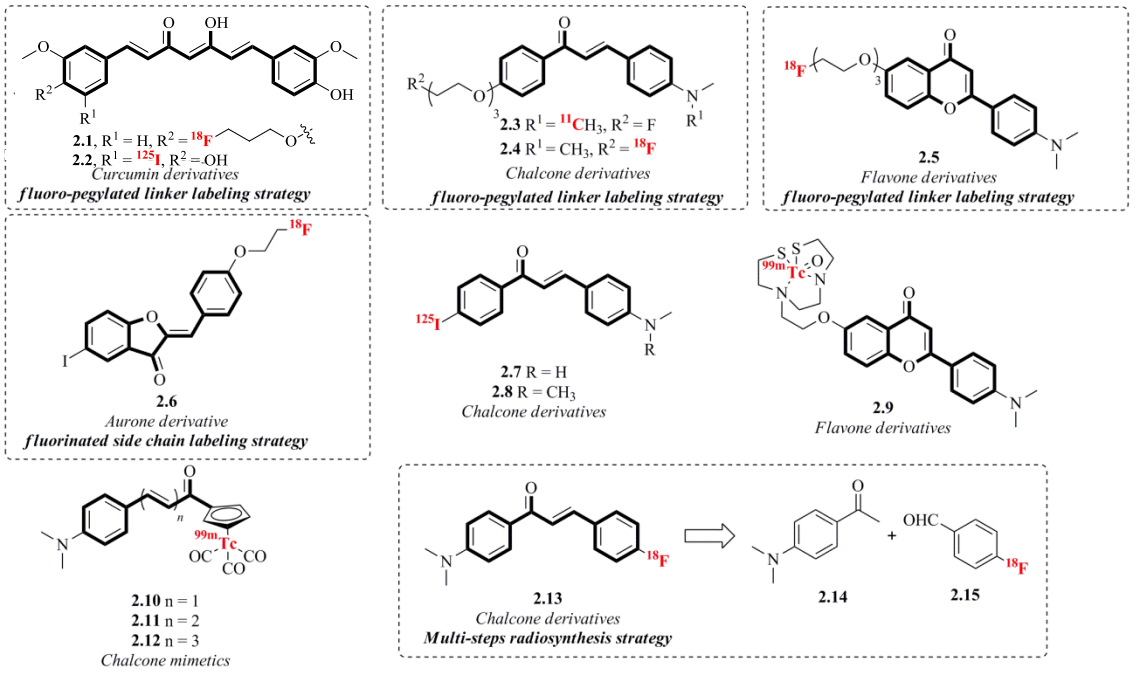

Figure 2.2. Radiolabeling strategies for reported radiolabeled flavonoids for SPECT (^{99m}Tc) and PET (^{11}C, ^{18}F) imaging or binding studies (^{125}I). The radiotracers depicted were developed for Aβ plaques imaging.

Interestingly, studies directed at ^{18}F-labeled PET flavonoid imaging agents development have, to the best of our knowledge, never address the possibility of direct radiofluorination on a susceptible position for S_NAr reaction on *para*-substituated benzylideneacetone precursors. Almost all agents evaluated append the [^{18}F]-fluorine label via S_N2 displacement of a tosylate or mesylate on a linker fragment.[24] Those strategies involving fluoroethyl, fluoropropyl or fluoro-pegylated side chains often derive from an original fluoroaryl lead. Although biological activity may be enhanced following this type of radiolabeling strategy, the outcome of such structural modification remain unpredictable and may negatively impact binding and physico-chemical properties such as lipophilicity and consequently non-specific binding – especially in the case of short fluoroalkyl chains. In a recent report, a two steps radiosynthesis involving the Claisen condensation of 4-[^{18}F]fluorobenzaldehyde was applied to synthesize the chalcone imaging agent **2.13** (Figure 2.2).[25]

2.4 Retrosynthesis of the candidate ^{11}C- and ^{18}F-labeled TrkB radiotracers

The efficient introduction of an ^{18}F-radiolabel from a suitable precursor as a way to generate a radioactive version of a fluorinated bioactive small molecule constitutes a central problem in ^{18}F-radiopharmaceutical chemistry. Considering the special case of flavonoids and flavones, the linker strategy presented above, provides a general approach for radiolabeling a target molecule but suffers from being potentially associated with complex structure-activity relationship studies and tedious chemistry – since multiple analogues with various chain types and lengths need to be synthesized and evaluated. On the other hand, a multi-step radiosynthesis with readily synthesized ^{18}F-aryl building block is often associated with extensive optimization and purifications. But, Aryl-H replacement with aryl-F is an almost ideal bioisosteric modification, which often results in enhanced potency, adsorption, metabolic stability and pharmacokinetics from the lead compound.[26]

With this in mind, the retro-radiosynthesis of multiple 7,8-dihydroxyflavone radiolabeled analogues is presented in the Scheme 2.3. The preferred radiotracers, [*N*-methyl-^{11}C]**1.59** and [^{18}F]**1.60,** are envisioned from direct B ring radiolabeling from suitable precursors. The ^{11}C-labeled tracer can be synthesized from the *des*-methyl precursor either regioselectively at the free catechol fragment or protected if the regioselectivity is problematic. The retrosynthesis of tracer [^{18}F]**1.60** addresses the question of the feasibility of simple direct radiofluorination on a *para*-subsituted aryl ring system with α,β-unsaturated carbonyl moiety. This approach constitutes a direct radiofluorination route and necessitates a suitable 4'-nitro or 4'-trimethylammonium trifluoromethanesulfonate precursor. Alternatively, the same tracer could be envisioned via multi-step radiosynthesis via a ^{18}F-aryl fragment.

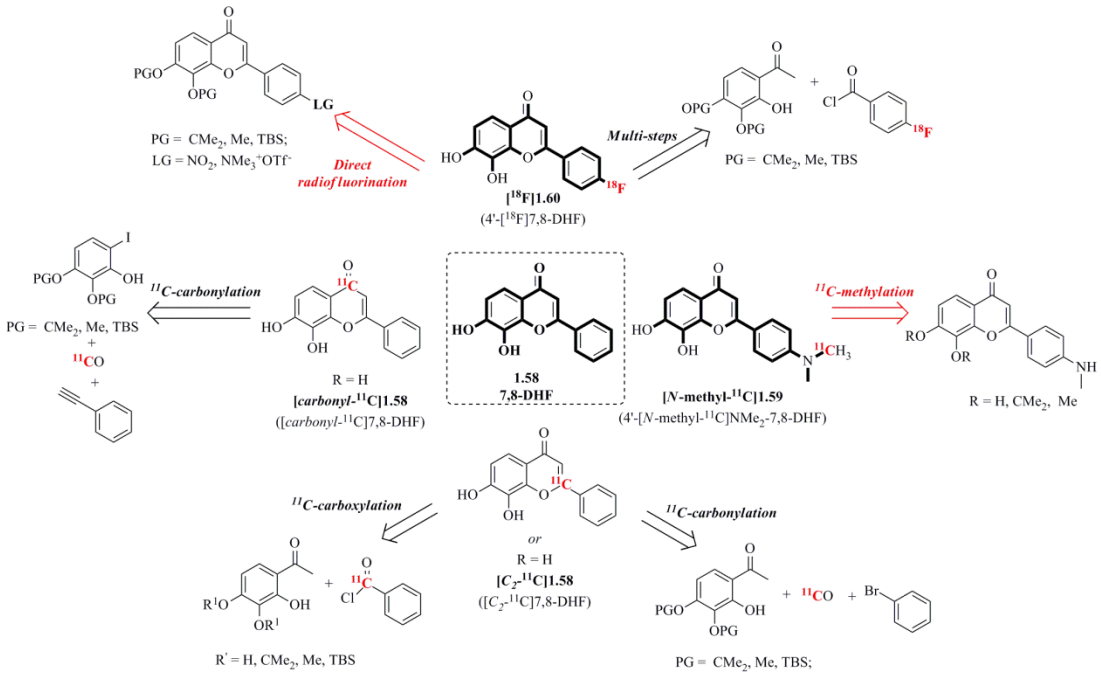

Scheme 2.3. Retro-radiosynthesis of envisioned ^{11}C- and ^{18}F-radiolabled 7,8-dihydroxyflavone probes for TrkB PET imaging from the radiolabeling precusors.

The ensemble of the other core-structures being labeled with ^{11}C involve ^{11}C-carbonylation or ^{11}C-carboxylation procedures, either multi-steps radiochemistry with ^{11}C ($t_{1/2}$ =20.3 min) which would be difficult to accomplish or complex synthetic apparatus (^{11}C-carbonylation, see section *1.2.1.5*). These options, albeit being possible, should be kept as secondary alternatives.

2.5 Synthesis of starting materials

The previous synthesis by Liu and colleagues[27] of compound **1.60** and the hydrobomic salt of **1.59** via the Baker-Venkataraman rearrangement/acid-promoted cyclization followed by hydrobromic acid methoxy deprotection prompted us to first select this route for the synthesis of the different analogues needed for this project. We also optimized the synthesis of the target precursors and standards via application of the Claisen condensation/iodine-catalyzed oxidative cylisation in DMSO in combination with boron tribromide methoxy deprotection (Chapter 3). Variations of three-steps one-

pot procedures promoted with mild base similar to the work done by Chee and colleagues[13a] and Riva and colleagues[13b] for the synthesis of flavones all failed to efficiently deliver the desired compounds.

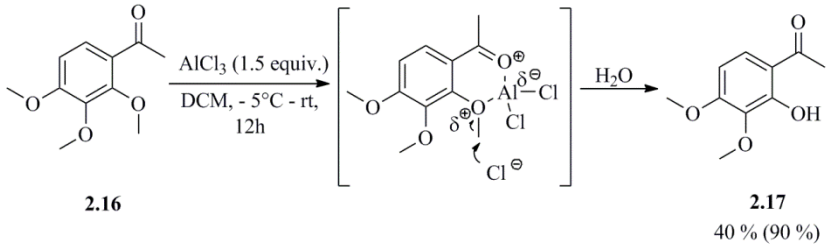

Scheme 2.4. Synthesis of gallacetophenone 3',4'-dimethyl ether via regioselective demethylation of 2'-3'-4'-trimethoxyacetophenone. The yields reported: our yield (yield of Ref. 28).

The starting material for our synthesis was the gallacetophenone 3′,4′-dimethyl ether (**2.17**) which is commercially available but expensive. We were interested in the possibility of synthesizing this compound from the cheaper 2'-3'-4'-trimethoxyacetophenone (**2.16**) via aluminium chloride-promoted regioselective demethylation as reported by Du and colleages.[28] Unfortunately, the yields obtained following this procedure and multiple variations thereof were moderate to low (<40%) in comparison to the reported yield (90%; Scheme 2.4).

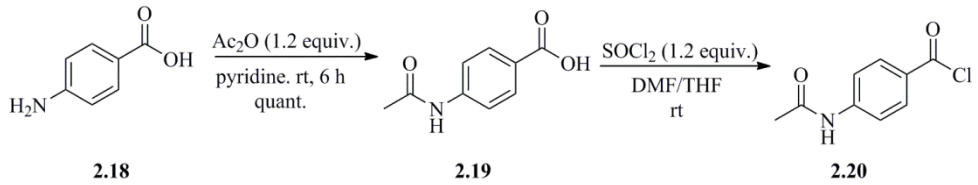

Scheme 2.5. Synthesis of *N*-acetyl acid chloride precursor **2.20**.

Using **2.17** from commercial source revealed to be more advantageous. Other necessary starting building blocks used in the next chapter, were the 4-substituted acyl chlorides for the Baker-Venkataraman rearrangement sequence. Those acyl chlorides were synthesized following the general method used for the conversion of **2.19** to **2.20** with thionyl chloride when not used from commercial source (Scheme 2.5). Compound **2.19**

was obtained quantitatively via the *N*-acetylation of the para-aminobenzoic acid **2.18** with acetic anhydride in pyridine following a reported procedure.[29]

2.6 Experimental section

General Remarks. See experimental section of chapter 3.

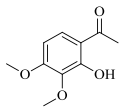

1-(2-hydroxy-3,4-dimethoxyphenyl)ethanone (gallacetophenone 3′,4′-dimethyl ether) (2.17). The title compound as obtain following a procedure reported in Ref. 28.

^{1}H NMR (300 MHz, $CDCl_3$) δ 12.57 (s, 1H), 7.50 (d, J = 9.0 Hz, 1H), 6.48 (d, J = 9.0 Hz, 1H), 3.93 (s, 3H), 3.88 (s, 3H), 2.57 (s, 3H) ppm. ^{13}C NMR (75 MHz, $CDCl_3$) δ 203.2, 158.5, 157.0, 136.5, 127.0, 115.3, 102.8, 60.7, 56.1, 26.4 ppm HRMS (ESI) calcd for $C_{10}H_{13}O_4Na$ $(M+Na)^+$ 219.0627, found 219.0627.

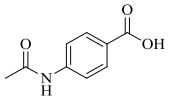

4-acetamidobenzoic acid (2.19). The title compound as obtain following a procedure reported in Ref. 29.

^{1}H NMR (300 MHz, DMSO-d_6) δ 12.65 (bs, 1H), 10.25 (s, 1H), 7.86 (dt, J_2 = 9.0 Hz, J_1 = 1.8 Hz, 2H), 7.67 (dt, J_2 = 9.0 Hz, J_1 = 1.8 Hz, 2H), 2.06 (s, 3H) ppm. ^{13}C NMR (75 MHz, DMSO-d_6) δ 169.3, 167.4, 143.8, 130.8, 125.3, 118.6, 24.6 ppm HRMS (ESI) calcd for $C_9H_8NO_3$ $(M-H)^-$ 178.0509, found 178.0511.

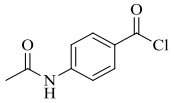

4-acetamidobenzoyl chloride (2.20). To a solution of the carboxylic acid **2.19** (179.2 mg, 1 mmol) in a mixture of THF (1.0 mL) and DMF (1.0 mL) at room temperature was added thionyl chloride (87 μL, 1.2 mmol, 1.2 equiv.). The reaction was stirred at this temperature and followed by TLC until completion. The volatiles were then removed under reduce pressure and the crude acyl chloride was used in the acylation without further purification.

2.7 References

1. Williams, R. J.; Spencer, J. P. E.; Rice-Evans, C. *Radical Biol. Med*. **2004**, *36*, 838-849.
2. Hwang, S.-L.; Shih, P.-H.; Yen, G.-C. *J. Agric. Food. Chem*. **2012**, *60*, 877-885.
3. Kanadaswami, C.; Lee, L.-T.; Lee, P.-P. H.; Hwand, J.-J.; Ke, F.-C.; Huang, Y.-T.; Lee, M.-T. *In vivo*, **2005**, *19*, 895-910.
4. Larsen, Dashwood, R. H.; Bisson, W. H. *Pharma. Res*. **2010**, *62*, 457-464.
5. Chahar, M. K.; Sharma, N.; Dobhal, M. P.; Joshi, Y. C.*Pharmacogn. Rev*. **2011**, *5*, 1-12.
6. Kuhnau J. *World Rev Nutr Diet.* **1976**, *24*, 117-191.
7. Nemeth, K.; Plumb, G. W.; Berrin, J. G.; Juge, N.; Jacob, R.; Naim, H. Y.; Williamson, G.; Swallow, D. M.; Kroom, P. A. *Eur. J. Nutr*. **2003**, *42*, 29-42.
8. Forkmann, G.; Heller, W. In *Comprehensive Natural Products Chemistry*; Barton, D., Nakanishi, K., Ed.; Elsevier: Oxford, 1999; Vol. 1, Chapter 26, pp 713-748.
9. (a) Baker, W. *J. Chem. Soc*. **1933**, 1381. (b) Mahal, H. S.; Venkatamaran, K. *J. Chem. Soc*. **1934**, 1767.
10. Allan, J.; Robinson, R. J. *J. Chem. Soc*. **1924**, *125*, 2192. (b) Horie, T.; Tsukayama, M.; Kawamura, Y.; Sen, M. *J. Org. Chem*. **1987**, *52*, 4702-4709.
11. For examples: (a) Jung, J. C.; Min, J. P.; Park, O. S. *Synth. Commun.* **2001**, *31*, 1837. (b) Tsukayama, M.; Kawamura, Y.; Ishizuka, T.; Hayas, S.; Torii, F. *Heterocycles*, **2003**, *60*, 2775. (c) Ghani, S. B. A.; Weaver, L.; Zidan, Z. H.; Ali, H. M.; Keevil, C. W.; Brown, R. C. D. *Bioorg. Med. Chem. Lett.* **2008**, *18*, 519-522.
12. Zhou, C.; Dubrovsky, A. V.; Larock, R. C. *J. Org. Chem.* **2006**, *71*, 1626-1632.
13. (a) Chee, C. F.; Buckle, M. J. C.; Rahman, N. A. *Tetrahedron Lett.* ***2011****, 52*, 3120-3123. (b) Riva, C.; DeToma, C.; Donadd, L.; Boi, C.; Pennini, R.; Motta, G.; Leonardi, A. *Synthesis*, **1997**, 195.

14. (a) Hercouet, A.; Corre, M. L. *Synthesis* **1982**, 597–598; (b) Kumar, P.; Bodas, M. S. *Org. Lett*. **2000**, *2*, 3821–3823. (c) Das, J.; Ghosh, S. *Tetrahedron Lett. 2011*, *52*, 7189–7194.
15. (a) Wang, Y.; Liu, J.; Xia, C. *Tetrahedron Lett.* **2011**, *52*, 1587–1591. (b) Yang, Q.; Alper, H. *J. Org. Chem*. **2010**, *75*, 948–950. (c) Okuro, K.; Alper, H. *J. Org. Chem.* **1997**, *62*, 1566–1567. (d) Miao, H.; Yang, Z. *Org. Lett.* **2000**, *2*, 1765–1768. (e) Awuah, E.; Capretta, A. *Org. Lett*. **2009**, *11*, 3210–3213. (f) Ciattini, P. G.; Morera, E.; Ortar, G.; Possi, S. S. *Tetrahedron* **1991**, *47*, 6449–6456.
16. Wu, X.-F.; Neumann, H.; Beller, M. *Chem. Eur. J.* **2012**, *18*, 12595–12598.
17. Awuah, E.; Capretta, A. *Org. Lett.* **2009**, *11*, 3210-3213.
18. See for exampels: (a) Chiruta, C.; Schubert, D.; Dargusch, R.; Maher, P. *J. Med. Chem.* **2012**, *55*, 378-389. (b) Cabreara, M.; Simoens, M.; Falchi, G.; Lavaggi, M. L.; Piro, O. E.; Castellano, E. E.; Vidal, A.; Azqueta, A.; Monge, A.; Lopez de Cerain, A.; Sagrare, G.; Seoane, G.; Cerecettoa, H.; Gonzaleza, M. *Bioorg. Med. Chem*. **2007**, *15*, 3356-3367. (c) Chavan, H. V.; Bandgar, B. P.; Adsul, L. K.; Dhakane, V. D.; Bhale, P. S.; Thakare, V. N.; Masand, V. *Bioorg. Med. Chem*. **2013**, *23*, 1315-1321.
19. For an example of iodine catalyzed oxidative reactions with DMSO, see: (a) Ge, W.; Zhu, X.; Wei, Y. *RSC Adv.*, **2013**, *3*, 10817-10822. (b) Ge, W. Wei, Y. *Green Chem*. **2012**, *14*, 2066-2070.
20. (a) Ono, M.; Ikeoka, R.; Watanabe, H.; Kimura, H.; Fuchigami, T.; Haratake, M.; Saji, H.; Nakayama, M. *Bioorg. Med. Chem. Lett*. **2010**, *20*, 5743-5748. (b) Li, Z.; Cui, M.; Dai, J.; Wang, X.; Yu, P. Yang, Y.; Jia, J.; Fu, H.; Ono, M.; Jia, H. ;Saji, H.; Liu, B. *J. Med. Chem*. **2013**, *56*, 471-482.
21. Ono, M.; Haratake, M.; Mori, H.; Nakayama, M. *Bioorg. Med. Chem*. **2007**, *15*, 6802-6809.
22. Ono, M.; Watanabe, R.; Kawashima, H.; Cheng, Y.; Kimura, H.; Watanabe, H.; Haratake, M.; Saji, H.; Nakayama, M. *J. Med. Chem*. **2009**, *52*, 6394-6401.
23. (a) Ono, M. Watanabe, R.; Kawashima, H.; Kawai, T.; Watanabe, H.; Haratake, M.; Saji, H.; Nakayama, M. *Bioorg. Med. Chem*. **2009**, *17*, 2069-2076. (b) Watanabe, H.; Ono, M.; Kimura, H.; Kagawa, S.; Nishii, R.; Fuchigami, T.;

Haratake, M.; Nakayama, M.; Saji, H. *Bioorg. Med. Chem. Lett*. **2011**, *21*, 6519-6522. (c) Cui, M.; Ono, M.; Kimura, H.; Liu, B.; Saji, H. *J. Med. Chem*. **2011**, *54*, 2225-2240. (d) Ryu, E. K.; Choe, Y. S.; Lee, K. H.; Choi, Y.; Kim, B. T. *J. Med. Chem*. **2006**, *49*, 6111-6119.

24. Stephenson, K. A.; Chandra, R.; Zhuang, Z. P.; Hou, C.; Oya, S.; Kung, M. P.; Kung, H. F.; *Bioconjugate Chem*. **2007**, *18*, 238-246.
25. These results were reported at the 20th International Conference on Radiopharmaceutical Sciences (ISRS) in Jeju, Korea, May 12-17 2013.
26. Muller, K.; Faeh, C.; Diederich, F. *Science* **2007**, *317*, 1881-1886.
27. Liu, X.; Chan, C.-B.; Jang, S.-W.; Pradoldej, S.; Hang, J.; He, K.; Phun, L. H.; France, S.; Xiao, G.; Jia, Y.; Luo, H. R.; Ye, K. *J. Med. Chem*. **2010**, *53*, 8274-8286.
28. Du, Z.-T.; Lu, J.; Yu, H.-R.; Xu, Y.; Li, A.-P. *J. Chem. Res*. **2010**, 222-227.
29. Qiu, J.; Xu, B.; Huang, Z.; Pan, W.; Cao, P.; Liu, C.; Hao, X.; Song, B. Liang, G. *Bioorg. Med. Chem*. **2011**, *19*, 5352-5360.

Chapter 3

Article:

Bernard-Gauthier, V; Gaub, P.; Boudjemeline, M.; Rosa-Neto, P.; Barker, P. A.; Thiel, A. and Schirrmacher, R. **Radiosynthesis and Evaluation of ^{18}F- and ^{11}C-Labeled 7,8-Dihydroxyflavones as Tropomyosin-Related Kinase B (TrkB) Receptor Ligands for Brain Imaging with Positron Emission Tomography**

*Journal of Medicinal Chemistry, **2013**, submitted*

Radiosynthesis and Evaluation of ^{18}F- and ^{11}C-Labeled 7,8-Dihydroxyflavones as Tropomyosin-Related Kinase B (TrkB) Receptor Antagonists for Brain Imaging with Positron Emission Tomography

Bernard-Gauthier, Vadim[1,2]; Gaub, Perrine[3]; Boudjemeline, Mehdi[1]; Rosa-Neto, Pedro[4]; Barker, Philip A.[3]; Thiel, Alexander[5] and Schirrmacher, Ralf[1,2]*

1. Département de Chimie, Université de Montréal, P.O. Box 6128, Station Downtown, QC, Canada H3C 3J7
2. McConnell Brain Imaging Centre, Montreal Neurological Institute, McGill University, 3801 University Street, Montreal, QC, Canada, H3A 2B4,
3. Department of Neurology and Neurosurgery, Montreal Neurological Institute, McGill University, 3801 University St., Montreal, QC, Canada, H3A 2B4
4. Translational Neuroimaging Laboratory, McGill Centre for studies in Aging, Douglas Mental Health University Institute, Canada
5. Department of Neurology and Neurosurgery, McGill University, Jewish General Hospital, 3755 Cote St. Catherine Rd., Montreal, QC, Canada, H2T 1E2

3.1 Graphical Abstract

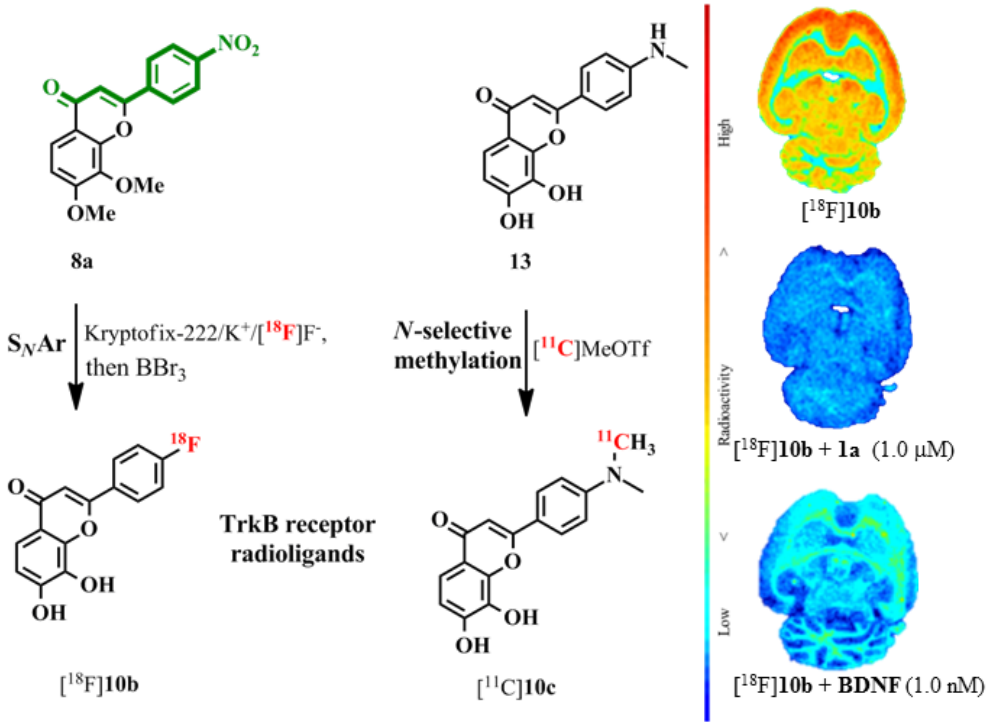

3.2 Abstract

The interaction of tropomyosin-related kinase B (TrkB) with the cognate ligand BDNF mediates fundamental pathways in the development of the nervous system. TrkB signaling alterations are linked to numerous neurodegenerative diseases and conditions. Herein we report the synthesis, biological evaluation and radiosynthesis of the first TrkB radioligands based on the recently identified 7,8-dihydroxyflavone chemotype. 2-(4-[^{18}F]fluorophenyl)-7,8-dihydroxy-4H-chromen-4-one ([^{18}F]**10b**) was synthesized in high radiochemical yields via an unprecedented S_NAr radiofluorination involving a *para*-Michael acceptor substituted aryl followed by BBr_3-promoted double demethylation. Selective *N*-[^{11}C]methylation afforded 2-(4-([*N*-methyl-^{11}C]-dimethylamino)phenyl)-7,8- dihydroxy -4H-chromen-4-one ([^{11}C]**10c**) from the fully deprotected catechol-bearing normethyl precursor **13** with [^{11}C]MeOTf . *In vitro* autoradiography of [^{18}F]**10b** with transverse rat brain sections revealed high specific binding in the cortex, striatum, hippocampus and thalamus in accordance with expected TrkB distribution. Blockade experiments with both 7,8-dihydroxyflavone (**1a**) and TrkB cognate ligand, BDNF, led to decreases of 80% and 85% of radioligand binding strongly supporting the hypothesis that 7,8-dihydroxyflavones exert their effect on TrkB phosphorylation via direct TrkB ECD binding. Positron emission tomography (PET) studies revealed that [^{18}F]**10b** and [^{11}C]**10c** brain uptake is minimal and that they are rapidly eliminated from the plasma (effective plasma half-life 5-10 minutes) via hepatic secretion. Nevertheless, the high specific binding and TrkB specificity derived from *in vitro* experiments suggests that the 7,8-disubsituted flavone chemotype represents a promising scaffold for the development of TrkB radiotracers for PET.

3.3 Introduction

Neurotrophins constitute a family of dimeric small secretory proteins that regulate neuronal development and survival while promoting synaptogenesis and synaptic function by interacting with their cognate tropomyosin-related kinases (Trk) receptors both in the central (CNS) and peripheral nervous system (PNS).[1-3] Members of this class of proteins include brain-derived neurotrophic factor (BDNF), neurotrophin-3 (NT-3), neurotrophin-4 (NT-4/5) and nerve growth factor (NGF). Neurotrophic activity is exerted through selective and high affinity binding to Trk receptors (e.g. $K_d = 9.9\times10^{-10}$ M for BDNF toward TrkB; NGF binds to TrkA, BDNF and NT-4 bind to TrkB and NT-3 binds to TrkC) while non-selective binding of all neurotrophins to the structurally unrelated $p75^{NTR}$ receptor ($K_d \approx 10^{-9}$ M) leads to apoptosis in the absence of Trk receptors.[4,5] More specifically, BDNF binding to TrkB elicits receptor dimerization and autophosphorylation of the tyrosine kinase domain, in turn leading to the activation of the primary growth factor signaling pathways: Ras/MAPK, PI3K and PLCγ.[1,6] Neurotrophin-independent TrkB activation mechanisms have also been described but their physiological significance has not been elucidated to date.[7-9] In addition to the full length *trkB* isoform (TrkB.FL), two truncated isoforms lacking the catalytic tyrosine kinase domain (TrkB.T1 and TrkB.T2) acting as a dominant/negative inhibitor of TrkB.FL have been characterized.[10] Moreover, $p75^{NTR}$ can directly interact with the extracellular and intracellular domain of Trk receptors and has been shown to negatively modulate TrkB-BDNF or -NT-4/5-mediated activation.[11]

The full length TrkB receptor, its truncated isoforms and BDNF are abundantly present in the adult mammalian brain, particularly in the cerebral cortex, hippocampus, striatum and brainstem.[12,13] Increasing evidence suggests a correlation between changes in BDNF/TrkB signaling and numerous neurodegenerative and psychiatric disorders, such as Alzheimer's disease (AD),[14] Rett syndrome,[15] Parkinson's disease (PD),[16] Huntington's disease (HD),[17] schizophrenia,[18] traumatic brain injury (TBI)[19] and major depressive disorder (MDD).[20] While these findings generally link TrkB activation with favorable biological effects, expression and upregulation of TrkB signaling was also found to be associated with cellular modifications leading to tumorigenesis in

neuroblastomas,[21] pancreatic cancer[22] and non-small-cell lung cancer.[23,24] Altogether, these studies suggest that the TrkB/BDNF system is of great interest as a therapeutic target for neurology and oncology. However, clinical trials involving BDNF-based treatments have afforded limited therapeutic benefits, mainly due to the suboptimal pharmacological properties of neurotrophins (e,g, poor blood-brain barrier (BBB) penetration, poor serum stability, and limited oral bioavailability).[25] In addition, BDNF interaction with $p75^{NTR}$ is thought to be associated with the promotion of pain.[26] For these reasons, the development of non-peptidic small molecule TrkB-specific ligands has been actively pursued.

In 2010, Jang and colleagues have identified 7,8-dihydroxyflavone (7,8-DHF, **1a**) as a high affinity extracellular domain (ECD) TrkB selective ligand with agonistic activity in hippocampal neurons via random screening (K_d = 320 nM).[27] This compound was subsequently refined, yielding 4'-dimethylamino-7,8-dihydroxyflavone (**1b**) and 8-(4-(pyrrolidin-1-yl)phenyl)chromeno[7,8-*d*]imidazol-6(1*H*)-one (**2a-b**) ligands with increased potencies and improved pharmacokinetic profile.[28,29] Concurrently, structurally unrelated small molecule TrkB ligands with nanomolar antagonistic or agonistic activity were independently reported and characterized both *in vitro* and *in vivo* (**3**, **4**; Figure 1).[30,31] Altogether, these findings represent a promising tool for the investigation of the BDNF-TrkB system.

Flavones, and flavonoids in general, are traditionally known to exert various biological effects including anti-oncogenic, anti-oxidant, anti-inflammatory and anti-bacterial.[32] In the present case, the observed neurotrophic activity of 7,8-DHF and optimized 7,8-DHF derivatives (**1b** , **2a-b**) was mostly evaluated *in vitro* but their systemic administration in rodents was found to induce various BDNF-associated behavioural phenotypes.[27-29, 33-37] However, direct biochemical evidence for the interaction of 7,8-DHF derivatives with TrkB at the cellular level has not been thoroughly assessed – most studies following the original discovery of those compounds were directed towards behavioural phenotypes and *ex vivo* immunoblotting analysis subsequent to 7,8-DHF treatment. In addition, evidence of BBB penetration by 7,8-DHF derivatives has only been indirectly assessed and remains to be fully addressed. Moreover, attempts to visualize TrkB receptor

distribution non-invasively *in vivo* with imaging modalities such as positron emission tomography (PET) has not been previously reported due to the lack of suitable radiolabeled TrkB receptor ligands.

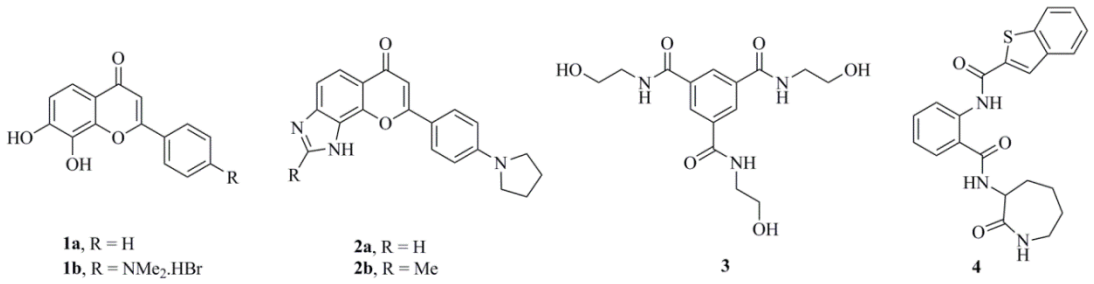

Figure 1. Chemical structures of previously reported non-peptidic small molecules TrkB-specific ligands.

PET is an imaging modality using radionuclides which decay via positron emission that are attached to biologically active compounds such as receptor ligands for brain imaging. Once injected, the biodistribution of the labelled compound can be conveniently followed by the detection of the positron-electron annihilation that occurs shortly after the positronium formation. This annihilation process yields two gamma rays of 511 keV that are emitted simultaneously at an angle of 180°. These rays can be detected concurrently in a ring shaped arrangement of gamma detectors (PET camera), revealing the origin of the radioactive decay dynamically in the living body.

The development of TrkB radioligands for positron emission tomography (PET) imaging could provide a non-invasive tool towards the study of the distribution and concentration of TrkB receptors and the pathophysiology of TrkB-related diseases. As a starting point in our efforts towards the development of the first radiolabelled TrkB ligand for PET imaging, we selected the previously reported 7,8-dihydroxyflavone scaffold, which displays high affinity and selectivity for ECD TrkB receptors and would lead to a pan-TrkB isoform radiotracer.[27-29] This motif is particularly attractive as it bears a readily functionalizable 4'- position amenable for ^{11}C- and ^{18}F-labeling. Herein

we present the radiosynthesis and preliminary PET evaluation in rat of 2-(4-[^{18}F]fluorophenyl)-7,8-dihydroxy-4*H*-chromen-4-one ([^{18}F]**10b** and 2-(4-([*N*-methyl-^{11}C]-dimethylamino)phenyl)-7,8-dihydroxy-4*H*-chromen-4-one ([^{11}C]**10c**) for TrkB imaging. We furthermore report the biological evalution of the corresponding non-radioactive standards **1a**, **10b**, **10c** and **15** towards TrkB receptors in cerebellar granule neuron (CGN), *in vitro* autoradiography of [^{18}F]**10b** and radiometabolite studies of both tracers.

3.4 Result and discussion

3.4.1 Chemistry

In order to obtain the radiolabelled hydroxyflavones [^{18}F]**10b** and [^{11}C]**10c**, the labeling precursors as well as the non-radioactive standard compounds for the establishment of a fast HPLC separation and quality control have to be synthesized. The two approaches devised for the synthesis of the 7,8-dihydroxyflavones **10a-c** are outlined in Scheme 1. The first route involved the well-known Baker–Venkataraman rearrangement of 2-acetoxyacetophenones **6a-d** to the corresponding 1-(2-hydroxyphenyl)-3-phenylpropane-1,3-diones (**7a-d**) followed by acid-catalyzed dehydrative cyclization.[38,39] Liu and colleagues[28] previously prepared **1b** and **8b** using this approach combined with refluxing HBr for the deprotection of the aromatic methoxy groups but the characterisation of the intermediates was not reported. Here, the 7,8-dimethoxyflavones **8a-d** were obtained in 11-38% overall yields from the corresponding 4'-sustituted benzoyl chlorides and thoroughly characterized with the exception of **7c** and **7d** which were used without further characterization in a two-step procedure (Scheme 1). This approach delivered the 4'-nitro precursor (**8a**, Scheme1) required for one-step aromatic nucleophilic radiofluorination of [^{18}F]**8b** as

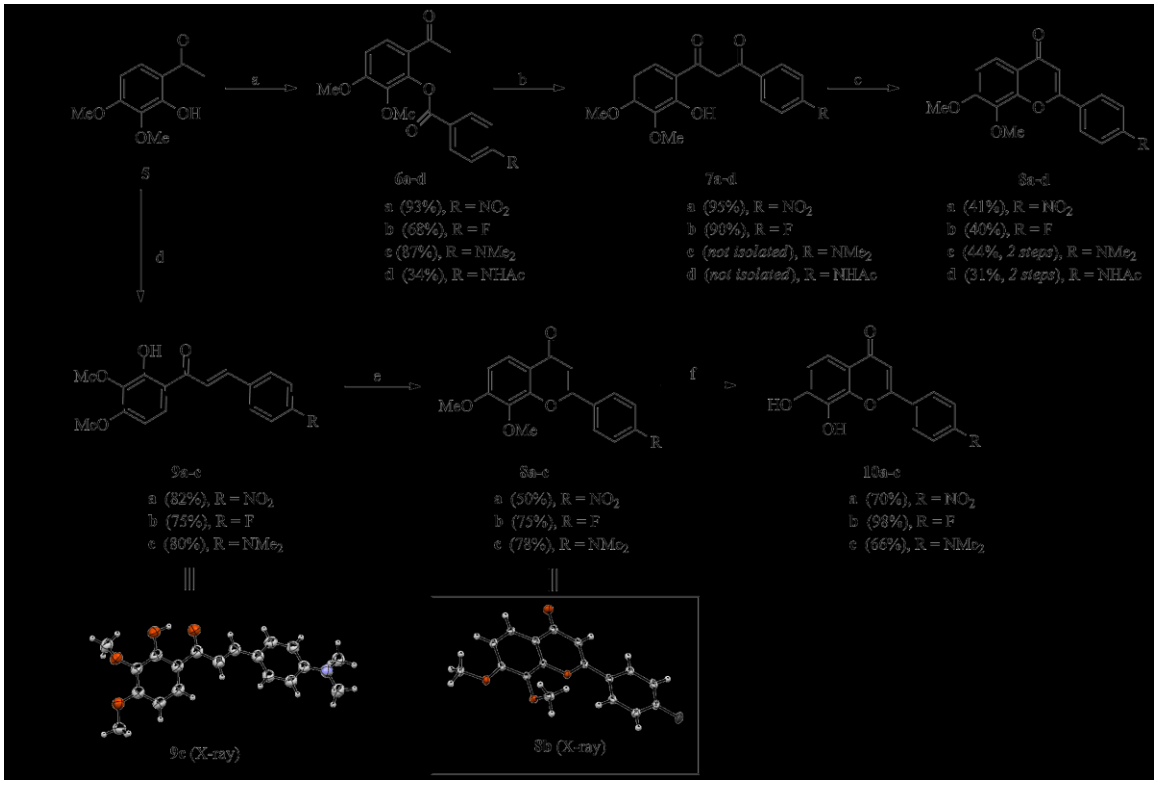

Scheme 1. Synthesis of **8a-d** and **10a-c** via the Baker–Venkataraman rearrangement and Claisen-Schmidt condensation/ I_2-DMSO mediated oxidative cyclization approaches. Reagents and conditions: (a) *p*-R-PhCOCl, CH_2Cl_2 / pyridine, rt, 2-4 h; (b) pyridine, KOH, 50°C, 12 h; (c) H_2SO_4, AcOH, reflux, 1-3 h; (d) *p*-R-PhCHO, $Ba(OH)_2$, MeOH, 40°C, 24 h; (e) I_2, DMSO, 130°C, 5-6 h; (f) BBr_3, CH_2Cl_2, rt, 12h. Single-Crystal X-Ray structure of **8b** and **9c**; ellipsoids drawn at 50% probability.

well as the non-radioactive standards **8b** and **8c**. The acetylanilide intermediate **8d** first envisioned for the synthesis of [^{11}C]**10c** (*vide infra*) (Figure 4C) could be obtained, albeit in low yield. This approach, although capable of delivering the targeted 7,8-dimethoxyflavones **8a-d**, was associated with the formation of significant side products and troublesome purification by flash chromatography.

In order to ensure the availability of these crucial intermediates, the compounds **8a-c** (Scheme 1) were alternatively synthesized in two steps with higher yields (41-62% overall yields) employing Claisen-Schmidt condensations followed by I_2-DMSO mediated oxidative cyclization.[40] The 4'-sustituted chalcones **9a-c** (Scheme 1) were obtained in good yields (75-82%) and easily recrystallized after reacting **5** with the

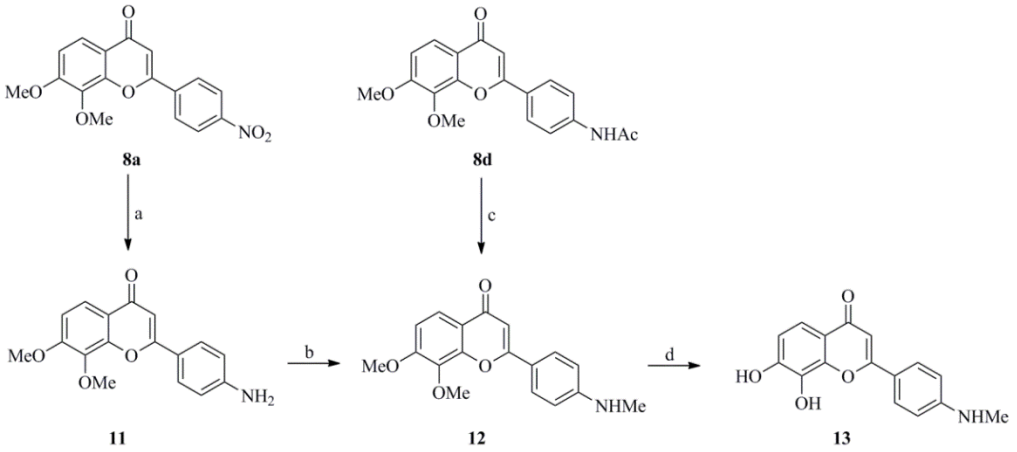

Scheme 2. Synthesis of Precursors **12** and **13**. Reagents and Conditions: (a) $SnCl_2.2H_2O$, EtOH, reflux, 8h, 47%; (b) i. paraformaldehyde, MeONa, MeOH, rt then reflux, 1h; ii. $NaBH_4$, reflux, 2h, 86% (2 steps); (c) i. NaH, THF, 0°C, 15 min, then rt, MeI, 4h; ii. Ethylene glycol, HCl conc., reflux, 2h, 81% (2 steps); (d) BBr_3, CH_2Cl_2, rt, 12h, 92%.

corresponding 4-substituted benzaldehydes in the presence of $Ba(OH)_2$ in methanol (representative molecular structure exemplified for **9c** obtained from X-ray analysis is shown in Scheme 1). Chalcone iodine-mediated cyclization proceeded in moderate to good yields and afforded flavones **8a-c** (41-62% overall yields) which were subsequently deprotected yielding **10a-c**. Refluxing HBr for the methoxy deprotection, as previously reported, [28] was inefficient in our hand whereas BBr_3-mediated demethylation proceeded both effectively and cleanly. Overall, this approach was more efficient and delivered the desired compounds **10a-c** in higher yields than did the Baker–Venkataraman rearrangement/HBr route.

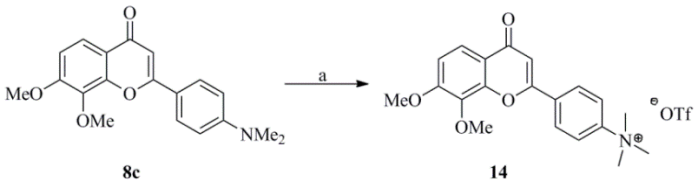

Scheme 3. Synthesis of Precursor **14**. Reagents and Conditions: (a) MeOTf, CH_2Cl_2, rt, 4h, 84%.

The structure of **8b** was elucidated by X-ray crystallographic analysis and the ORTEPs are represented in Scheme 1. We obtained the ^{11}C-methylation precursor **13** (Scheme 2) for the synthesis of TrkB radioligand [^{11}C]**10c** via two different routes starting from either **8a** or **8d** (Scheme 2). The initially projected pathway involved the methylation and acid- catalyzed deacetylation of compound **8d**.[41] Although this procedure afforded the *N*-methylaniline **12** in good yield (81%), the synthesis of **8d** itself was problematic (*vide supra*). Alternatively, the Stephen reduction from the nitro precursor **8a** followed by reductive monomethylation was synthetically superior and afforded compound **12** in higher yields. [42] Precursor **12** was converted to **13** following BBr_3-mediated demethylation in CH_2Cl_2. The reactive aryltrimethylammonium triflate labeling precursor **14** for direct radiofluorination was obtained in 84% yield when reacting **8c** with methyl triflate at room temperature (Scheme 3) offering an alternative way to obtain the projected radiofluorinated tracers [^{18}F]**10b**. [43] 7,8-Dimethoxyflavone (**15**) was synthesized by treating **1a** with methyl iodide and K_2CO_3 and was structurally elucidated by X-ray crystallographic analysis (Scheme 4).

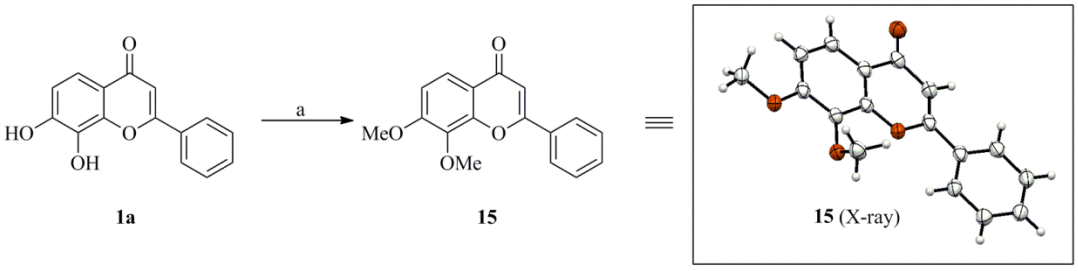

Scheme 4. Synthesis and Single-Crystal X-Ray structure of **15**. Reagents and Conditions: (a) MeI, K_2CO_3, DMF, rt, 2h, 94%. Single-Crystal X-Ray structure of **15**; ellipsoids drawn at 50% probability.

3.4.2 Biological Evaluation

7,8-DHF (**1a**) and 4'-sustituted analogs have been previously shown to upregulate TrkB signaling in primary rat cortical and hippocampal neurons (K_d = 320 nM) as well as in retinal ganglion cells (RGCs).[27-29, 44] These studies have also indicated upregulation of the downstream MAPK/ERK and PI3K/AKT pathways in correlation with TrkB activation. Interestingly, recent findings established that the ERK signaling pathway was either unaffected or downregulated in motoneurons[45] and macrophages[46], respectively, in response to 7,8-DHF treatment, indicating that 7,8-DHF activity may be cell-type specific.

Consequently, in order to develop ^{18}F- and ^{11}C-labeled TrkB receptor PET ligands based on the 7,8-DHF scaffold we initially re-evaluated the agonistic effect of 7,8-DHF (**1a**), **10b** and **10c** towards TrkB using CGN primary culture, a classic TrkB-expressing model. [47-49] Notably, Western blotting following CGN treatment with 7,8-DHF (**1a**), **10b** and **10c** did not reveal TrkB phosphorylation compared to control and BDNF treatment alone up to 500 μM. The tested compounds also failed to trigger ERK activation (Figure 2A).

Remarkably, at higher concentrations, co-incubation of cultured CGN with 7,8-DHF (**1a**), **10b** or **10c** in combination with BDNF (1.8 nM) led to a significant down-regulation of phosphorylation of both TrkB and ERK (Figure 2B). Each of the three compounds demonstrated strong concentration-dependent inhibition (50 μM, 250 μM, 500 μM) of BDNF-induced TrkB phosphorylation (Figure 2C). This inhibitory effect on phosphorylated -TrkB (p-TrkB) was observed as early as 10 min after addition and was maintained at least over 2 h. All three catechol-bearing compounds **1a**, **10b** and **10c** were potent inhibitors, leading to complete concentration-dependent inhibition of the BDNF-induced TrkB phosphorylation. IC_{50} values of 74.4 μM (**1a**), 64.7 μM (**10b**) and 8.8 μM (**10c**) were determined in CGN (Figure 2D).

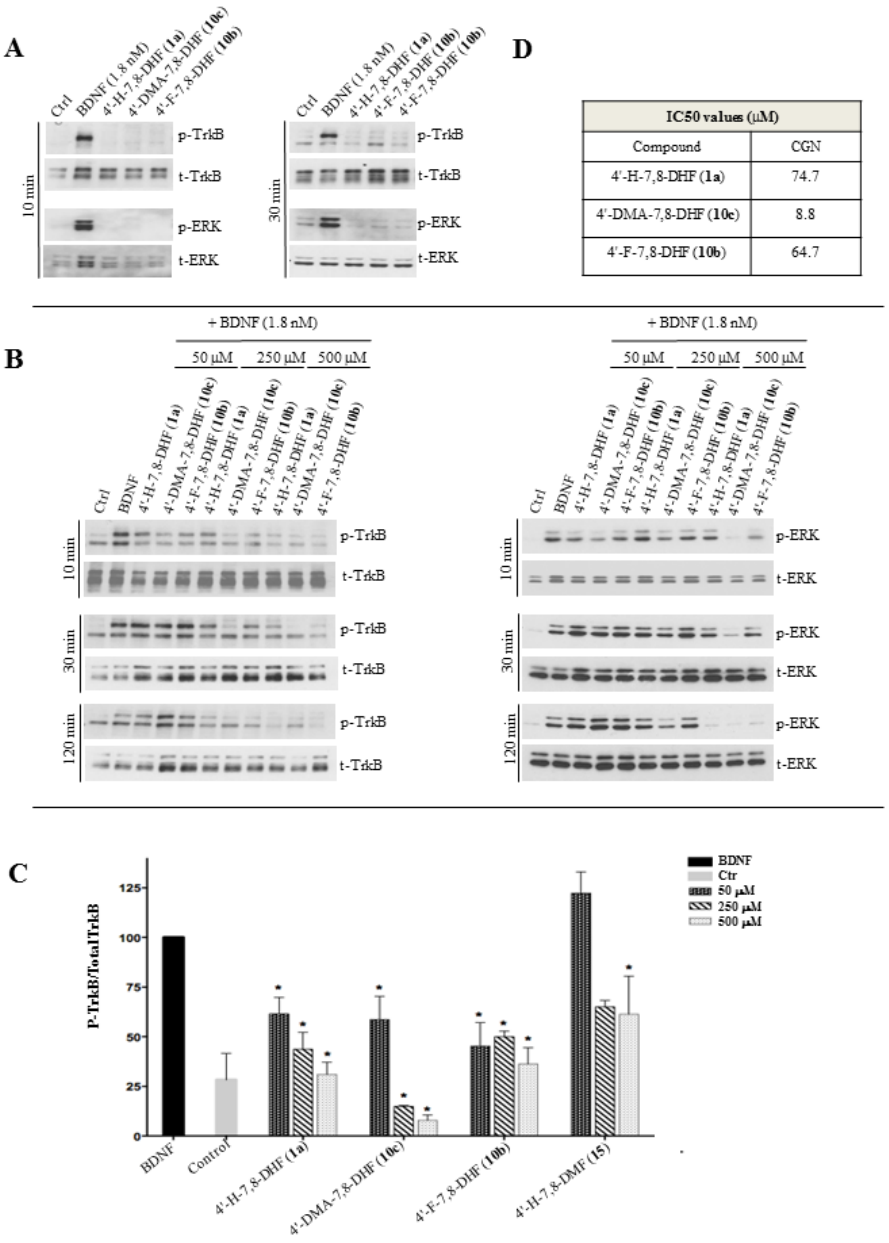

Figure 2. 7,8-DHF (**1a**), 4'-F-7,8-DHF (**10b**) and 4'-DMA-7,8-DHF (**10c**) inhibits BDNF-induced TrkB activity with high potency in cereballar granule neuron (CGN) while not demonstrating agonistic activity. (A) Immunoblotting experiments demonstrate that 7,8-DHF derivatives **1a**, **10b** and **10c** do not induce TrkB tyrosine phosphorylation in CGN upon 10 min (*left panel*) and 30 min (*right panel*) treatments (BDNF; 1.8 nM). Similarly, 7,8-DHF derivatives **1a**, **10b** and **10c** do not induce ERK phosphorylation. (B) (*left panel*) Representative western blots for different times of total TrkB (t-TrkB) and phosphorylated TrkB (p-TrkB) upon treatment of different concentrations of 7,8-DHF derivatives in the presence of BDNF (1.8 nM). 7,8-DHF derivatives **1a**, **10b** and **10c** acts as strong TrkB antagonist in CGN. (*right panel*) 7,8-DHF derivatives **1a**, **10b** and **10c** also inhibits ERK phosphorylation. (C) Quantification of p-TrkB concentrations from a densitometry analysis of the western blots for 7,8-DHF (**1a**, **10b** and **10c** **)** and 7,8-DMF (**15**, **8b** and **8c**) derivatives on BDNF-induced TrkB phosphorylation normalized to the maximum BDNF response at different antagonist concentrations. Primary

Cerebellar granule neurons were treated with BDNF (1.8 nM) and different antagonists concentrations (50 μM, 250 μM, 500 μM) for 30 min. Control corresponds to TrkB basal activity. Data are mean ± s.d. (n = 3) of ratio of p-TrkB/Total TrkB. *P < 0.01 compared to BDNF-induced TrkB phosphorylation by ANOVA followed by Dunnett't *post-hoc* analysis. 7,8-DHF derivatives **1a**, **10b** and **10c** act has strong and highly potent TrkB inhibitors. Compound **10c** abolishes basal TrkB activity. (D) 4'-H-7,8-DHF (**1a**), 4'-F-7,8-DHF (**10b**) and 4'-DMA-7,8-DHF (**10c**) half maximal inhibitory concentration (IC_{50}) values in CGN.

Moreover, compound **10c** was found to strongly inhibit both BDNF-induced TrkB activity along with TrkB basal activity at concentrations of 250-500 μM (-25.5±8.7% and -74.5±11.7% from basal activity, respectively). Those decreases in p-TrkB levels were similar to the ones obtained with K252a in the presence of the same concentration of BDNF (data not shown). Furthermore, the methylated analog **15** was tested for antagonistic activity in CGN (Figure 2C). The presence of the dimethoxy fragment instead of the catechol moiety was detrimental regarding inhibition of p-TrkB and downstream signaling deactivation such as ERK. Compound **15**, the dimethylated version of 7,8-DHF, did indeed reveal antagonistic activity, albeit at lower levels than its corresponding dihydroxy ligand and was also negative towards TrkB agonistic effects in the absence of BDNF in CGN (see *Supporting Information*). The results presented here with CGN support observations that cellular response regarding 7,8-DHF treatment may be cell specific and also suggest a concentration specific response. [45,46]

Given the results presented here, further investigation will be required to determine the precise outcome on TrkB phosphorylation and downstream signaling upon treatment with 7,8-DHF in different cell types and at different concentrations. Mechanisms, such as the implication of $p75^{NTR}$, known to directly interact with TrkB.T1[50] and TrkB.FL [51], may explain the cell specific response to 7,8-DHF treatment but will need to be evaluated thoroughly.

3.4.3 Radiochemistry

The initial radiosynthesis of [^{18}F]**8b** was achieved with Kryptofix-222/K^+/[^{18}F]F^- from the nitro precursor **8a** in DMF at 150°C for 20 minutes and proceeded with 80.9 ± 5.6% (*n* =5) radiochemical yield (incorporation RCYs determined by HPLC, non-decay corrected (n.d.c.), Figure 3A). Comparing the nitro precursor **8a** to the aryltrimethylammonium triflate **14** in various solvents at 150 - 160°C for 30 min demonstrated that **8a** was superior in terms of RCY and reproducibility of radiolabeling (Figure 3B, *left pannel*). Time optimization revealed that the radiofluorination reaches a plateau between 20 and 25 minutes at 150 ° C (*t* = 25 min; 82.7 ± 3.4% RCY (*n* =5), Figure 3B, *central pannel*). Reactions conducted below or above 150°C were either associated with a significant decrease in yields or degradation of the labeling precursor and the formation of radioactive side products.

The synthesis of [^{18}F]**8b** represents, to the best of our knowledge, the very first example of a S_NAr radiofluorination involving a *para*-Michael acceptor substituted aryl system. The efficient ^{18}F incorporation is somewhat surprising considering the deactivational character of the ring oxygen atom from the benzopyranone and the 7-methoxy fragment disfavouring the formation of the sigma complex upon reaction with ^{18}F. These results suggest that several bioactive flavones and aurones, or linear systems such as chalcones, dibenzylideneacetones or curcumins investigated for imaging purposes, could potentially be readily radiofluorinated through direct S_NAr following this strategy. [52]

The final ^{18}F-labelled TrkB ligand, 7,8-dihydroxyflavone [^{18}F]**10b** for animal PET imaging was subsequently synthesized via double methoxy deprotection of [^{18}F]**8b**. Initial attempts to deprotect [^{18}F]**8b** with refluxing HBr or sodium ethanethiolate gave erratic results, including degradation and defluorination (Figure 3B). BBr_3 in CH_2Cl_2 was found to efficiently dealkylate [^{18}F]**8b**, in agreement with the non-radioactive chemistry, and delivered [^{18}F]**10b** in good yield after 15 minutes at 70°C (77.1±7.4% RCY (*n* = 5), n.d.c. Figure 3B, *right pannel*).

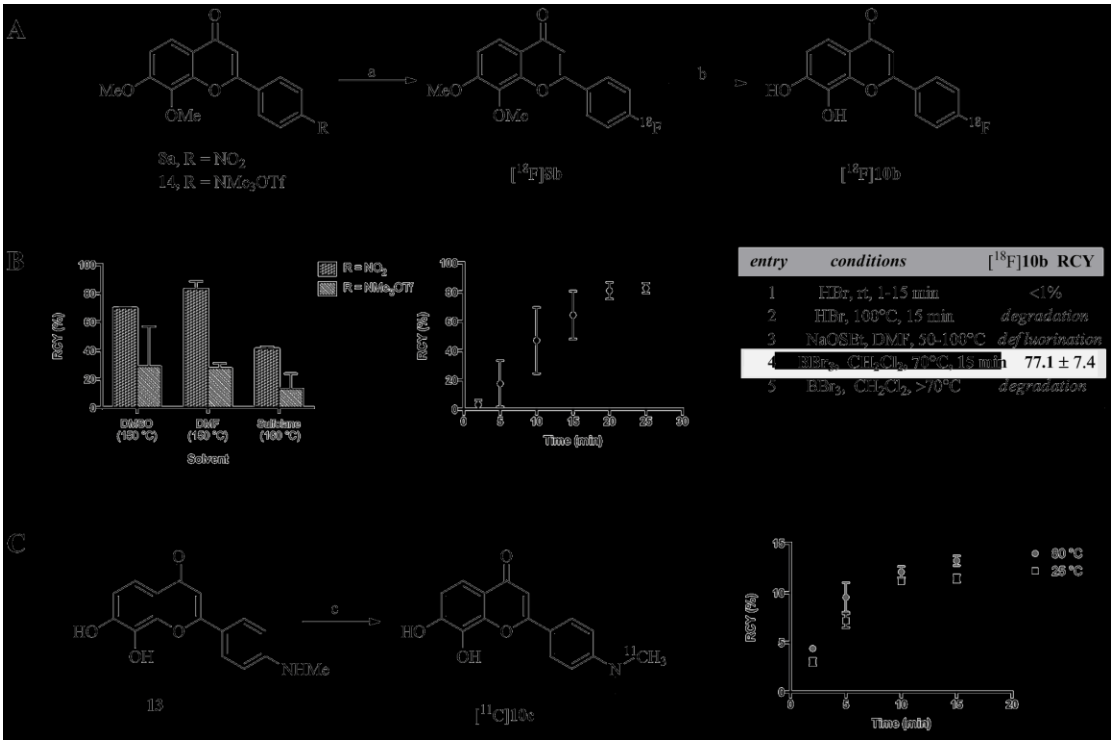

Figure 3. Radiosynthesis and optimization of [^{18}F]**8b**, [^{18}F]**10b**, and [^{11}C]**10c**. The RCY are calculated by radio-HPLC (n.d.c.). (A) Radiofluorination of precursors **8a** or **14**; Reagents and conditions (optimized, from **8a**): (a) Kryptofix-222/K^+/[^{18}F]F^-, DMF, 150°C, 25 min, 82.7 ± 3.4% RCY, (n = 5); (b) BBr_3/CH_2Cl_2, 70°C, 15 min, 77.1±7.4% RCY (n = 5). (B) (*left*) Solvent and precursors optimization for the synthesis of [^{18}F]**8b** (n = 2) for 30 min reactions. The 4'-nitro precursor **8a** is more efficiently radiofluorinated in all conditions; [^{18}F]**8b** is obtained in high RCY in DMF. (*center*) Optimization of the time of reaction for the conversion of **8a** to [^{18}F]**8b** in DMF at 150°C (n = 5). RCY reaches a plateau over 25 min. (*right*) Methoxy groups deprotection under various conditions. BBr_3-mediated deprotection in CH_2Cl_2 in a sealed vial at 70°C gives [^{18}F]**10b**. (C) (*left*) Optimization of the ^{11}C-methylation of **13**. Reagents and conditions: (c) [^{11}C]MeOTf, butanone, 80°C, 5 min, 9.6±1.0% RCY (n = 3). (*right*) Effect of the temperature on the ^{11}C-methylation of **13**.

Purification of the crude reaction mixture was performed by RP-HPLC following C-18 cartridge purification affording [^{18}F]**10b** in 37±4 % RCY (n =3) isolated yield from **8a** (n.d.c., relative to starting radioactivity of [^{18}F]F^-) after approximately 90 minutes with specific activities of 1.25-5.65 Ci/μmol and >99% radiochemical purity. This two-step procedure was highly efficient and cleanly afforded [^{18}F]**10b** for further PET applications (Figure 4).

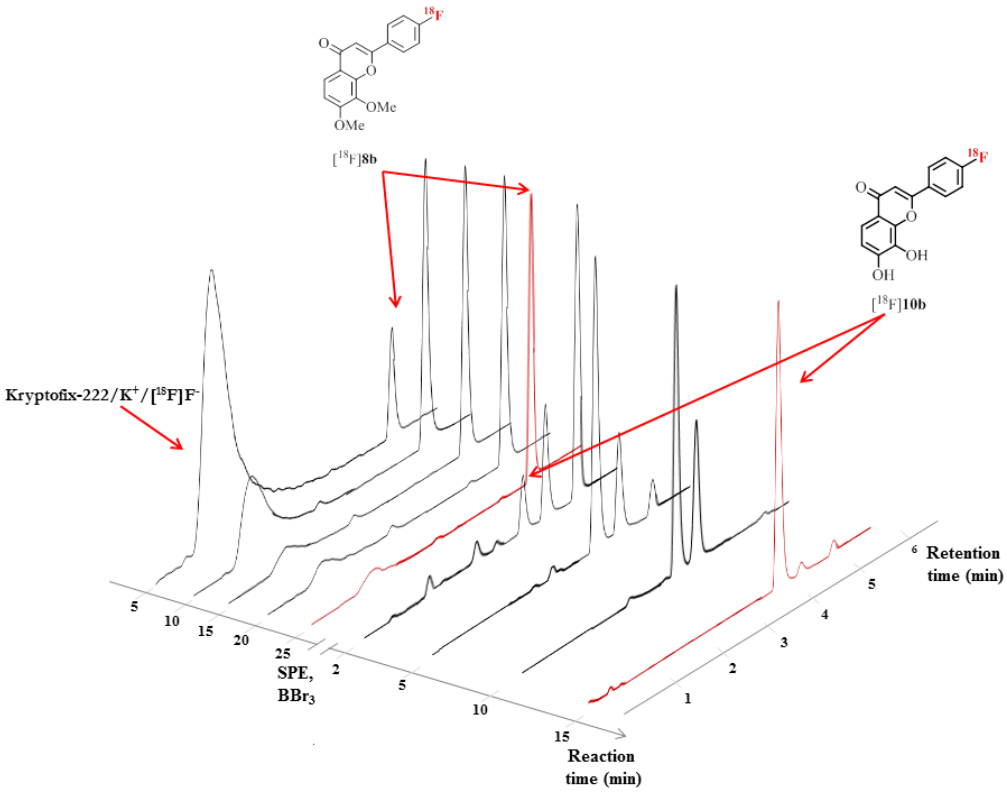

Figure 4. Analytical radiochromatograms for the advancement of the radiofluorination and BBr_3-promoted *bis*-deprotection reactions. See Experimental Section for the chromatographic conditions.

Radiolabeling of [^{11}C]**10c** for animal PET investigations was accomplished through selective *N*-[^{11}C]methylation with [^{11}C]MeOTf from diol *N*-normethyl precursor **13** in absence of base (Figure 3C). Attempts to methylate **13** with either [^{11}C]MeI or [^{11}C]MeOTf with different bases were all associated with the formation of a major side product, presumably an *O*-[^{11}C]methylated product. The optimized condition involved reacting **13** with [^{11}C]MeOTf, in butanone at 80°C for 5 minutes (9.6±1.0% RCY (*n* = 3), n.d.c.). The low RCY of this reaction is expected due to the deactivated character of *N*-methylanilines.[63d] Moreover, a two-step approach similar to the one used for the radiosynthesis of [^{18}F]**10b** was not possible owing to the incompatibility of the short carbon-11 half life and the time consuming steps associated with the manipulation of BBr_3 (e.g. solvent change, C-18 purification and the reaction itself). Purification of the crude reaction mixture was performed by RP-HPLC and afforded [^{11}C]**10c** in 5±2%

isolated yield (*n* =3, non-decay corrected), >98% radiochemical purity and a specific activity of 0.7-1.0 Ci/μmol.

3.4.4 In vitro plasma stabilities of [^{18}F]10b and [^{11}C]10c

The metabolic stabilities of the potential radiotracers were assessed by HPLC analysis of rat plasma incubated with [^{18}F]**10b** and [^{11}C]**10c**. Figure 5A illustrates the percentage of intact tracer during incubation in rat plasma at 37°C . Stability experiments for compound [^{18}F]**10b** demonstrated almost no degradation (10%) or defluorination after 90 min (Figure 5A). Along with the autoradiographic evaluation (*vide infra*), these results suggest that the specific binding in the brain during TrkB PET imaging correspond to the distribution of intact radioligand [^{18}F]**10b**. On the other hand, the radiotracer or [^{11}C]**10c** was significantly less stable in rat plasma and was associated with major metabolite formation with an half-life of approximately 10 min (Figure 5A-B). Interestingly, these results suggest that the catechol moiety, known to be susceptible to metabolic modifications such as methylation, sulfonation and glucuridination[53], has a limited influence on the immediate *in vitro* metabolic stability of the two compounds. In contrast, the presence of a dimethylamino fragment is highly detrimental toward plasma stability.

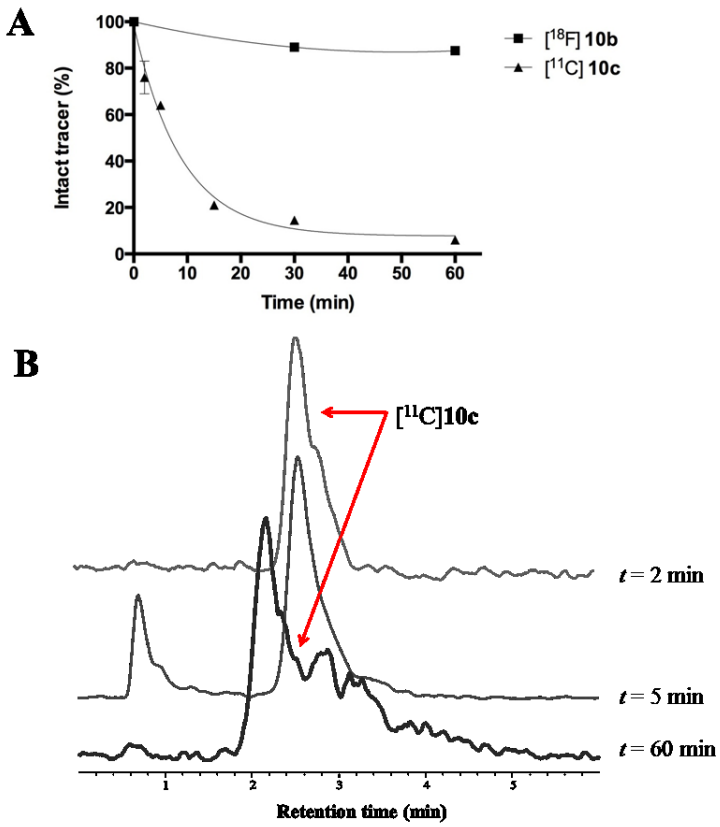

Figure 5. *In vitro* plasma stability. (A) Percentage of intact [^{18}F]**10b** and [^{11}C]**10c** in rat plasma at 37°C over time. Measures were made in duplicata (B) Radiochromatograms representing [^{11}C]**10c** metabolites formation from [^{11}C]**10c** over time.

3.4.5 Computation and Measurement of Ligands Lipophilicities

The computational lipophilicities (cLogD$_{7.4}$) for the radioligand [^{18}F]**10b** was 3.28 and 3.09 for [^{11}C]**10c** (Table 1). The experimentally determined values (LogD$_{7.4}$) for [^{18}F]**10b** and [^{11}C]**10c** were 2.2±0.2 and 2.8±0.1 respectively. The 4'-fluoro derivative was slightly less lipophilic than the 4'-dimethylamino derivative and slightly under the computed value. Since the incorporation of fluorine on an aryl fragment is normally associated with an increase in lipophilicity, it is possible that the observed differences arise from the overall effect of the introduction of fluorine on the conjugated system which is significantly different than the effect of the electro-donating dimethylamino moiety. Nevertheless, both tracers displayed lipophilicities in the favourable range of LogD 1.5-3.5 for BBB penetration. Also,

Table 1. Experimental and computed lipophilicities

Compound	[^{18}F]**10b**	[^{11}C]**10c**	**1a**	**15**
cLogP[a]	2.88	2.90	2.73	3.27
cLog*D*[b]	3.28	3.09	3.22	3.32
Log*D*[c]	2.2±0.2	2.8±0.1	- [d]	- [d]
PPB	24%	19%	- [d]	- [d]

[a,b] Values were computed with the program Pallas 3.7 for Windows (CompuDrug; SanFrancisco, CA) pH = 7.4 [c] Measurements made in triplicates. [d] Not measured

plasma protein binding was low for both radioligands with values of 24% and 19% for [^{18}F]**10b** and [^{11}C]**10c,** respectively.

3.4.6 In vitro Autoradiography

Figure 6 illustrates representative *in vitro* autoradiograms for compound [^{18}F]**10b** on horizontal rat brain sections with blocking either with **1b** or BDNF. The regional distribution pattern for the binding of [^{18}F]**10b** reveals a heterogeneous distribution with the most important radioactivity accumulation in the cerebral cortex. Radioligand binding was also observable in other TrkB-rich brain regions such as the caudate putamen, hippocampus and thalamus, and less significantly in the cerebellum. The autoradiography results obtained correlates well with the known TrkB distribution in rodent brain. [54] Co-incubation with **1b** (1.0 μM) resulted in overall dramatic reduction of [^{18}F]**10b** binding with low nonspecific binding for all regions of interest (ROI) concerned (17% in cortex, 21% in the striatum, 18% in the hippocampus, 19% in the thalamus and 23% in the cerebellum compared to the control experiment). In order to further evaluate if the ligand-specific binding derived from the co-incubation of [^{18}F]**10b** with the homologous ligand **1b** could be ascribed to a direct [^{18}F]**10b**-TrkB binding, co-incubation experiments with the high affinity TrkB cognate ligand, BDNF, were performed.

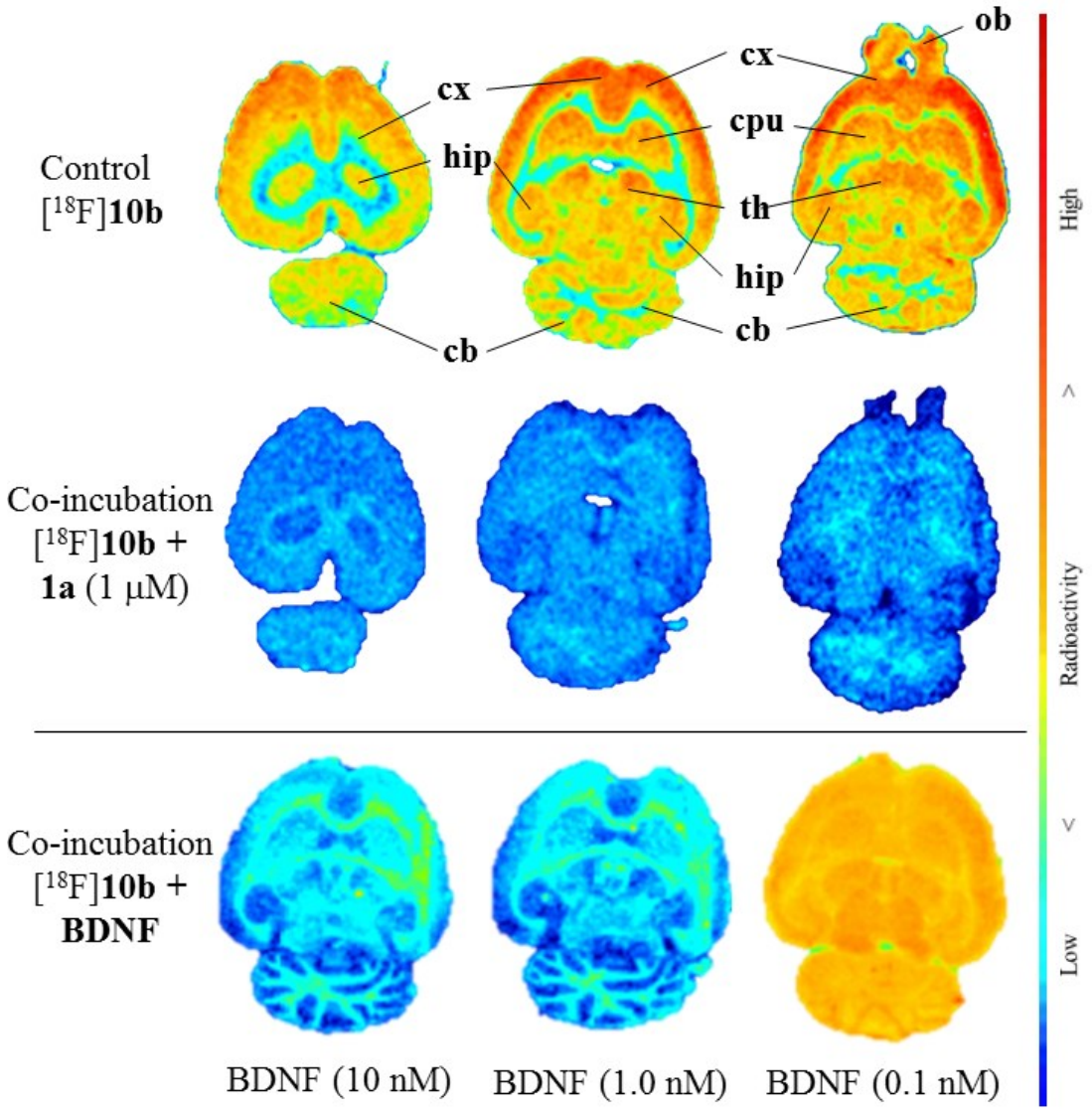

Figure 6. Representative *in vitro* autoradiograms of horizontal sections of rat brains (20 μm) illustrating the distribution of [^{18}F]**10b** accumulation and co-incubation with blocking agents. Binding of [^{18}F]**10b** cx = frontal cortex, cpu = caudate putamen, th = thalamus, , hip = hippocampus, cb = cerebellum, ob = olfactory bulb. (*top panel*). Co-incubation of [^{18}F]**10b** with **1a (**1.0 μM; *central panel*). Co-incubation of [^{18}F]**10b** with BDNF at various concentrations **(**10 nM, 1.0 nM and 0.1 nM; *low panel*).

Remarkably, [^{18}F]**10b** binding was displaceable in both 10 nM and 1.0 nM BDNF blocking experiments resulting in even more pronounced decreases in radiotracer binding (nonspecific binding; 16% in cortex, 14% in the striatum, 11% in the thalamus,

10% in the hippocampus and 12% in the cerebellum compared to the control experiment). Expectedly, significant binding of [^{18}F]**10b** was observed when the concentration of the co-incubated BDNF (0.1 nM) was under the affinity constant of the cognate ligand toward TrkB. Combined, these results strongly support the hypothesis that **10b** and 4'-subsitutued 7,8-DHF derivatives directly bind to the TrkB ECD. The small differences (~5-10%) in nonspecific binding between the homologous and heterologous blocking experiments which are present in all ROIs except in the cortex may be indicative of a secondary binding in those regions.

3.4.7 Small-Animal PET and Biodistribution Studies in Rats

Radioactivity distribution in whole brain and body in rats was monitored for 60 min following intravenous injection of [^{18}F]**10b**. Figure 7 shows the time activity curves (TACs) for [^{18}F]**10b**. Respective peak SUV_{BW} data from three rats for [^{18}F]**10b** (mean ± SE) are listed for each organ in Table 2.

Table 2. Average maximum SUV_{BW} for different tissues with standard error (SE) from three rats for [^{18}F]**10b**

Compartment	**Max SUV_{BW} ± SE**	**Time after injection [s]**
Aorta/heart	6.62 ± 0.542	30
Liver	6.80 ± 0.666	120
Kidney	4.38 ± 0.239	60
Brain	0.64 ± 0.148	30

The tracer is rapidly eliminated from plasma by hepatic secretion (estimated plasma half-life ≈ 4 min for [^{18}F]**10b**) through the bile and kidneys in approximately equal parts (TACs in Figure 7). These observations are consistent with the well-characterized rapid and extensive phase II metabolism associated with flavonoids, specifically hydroxyflavones (e.g. sulfonation, methylation, glucuronidation). [55-56]

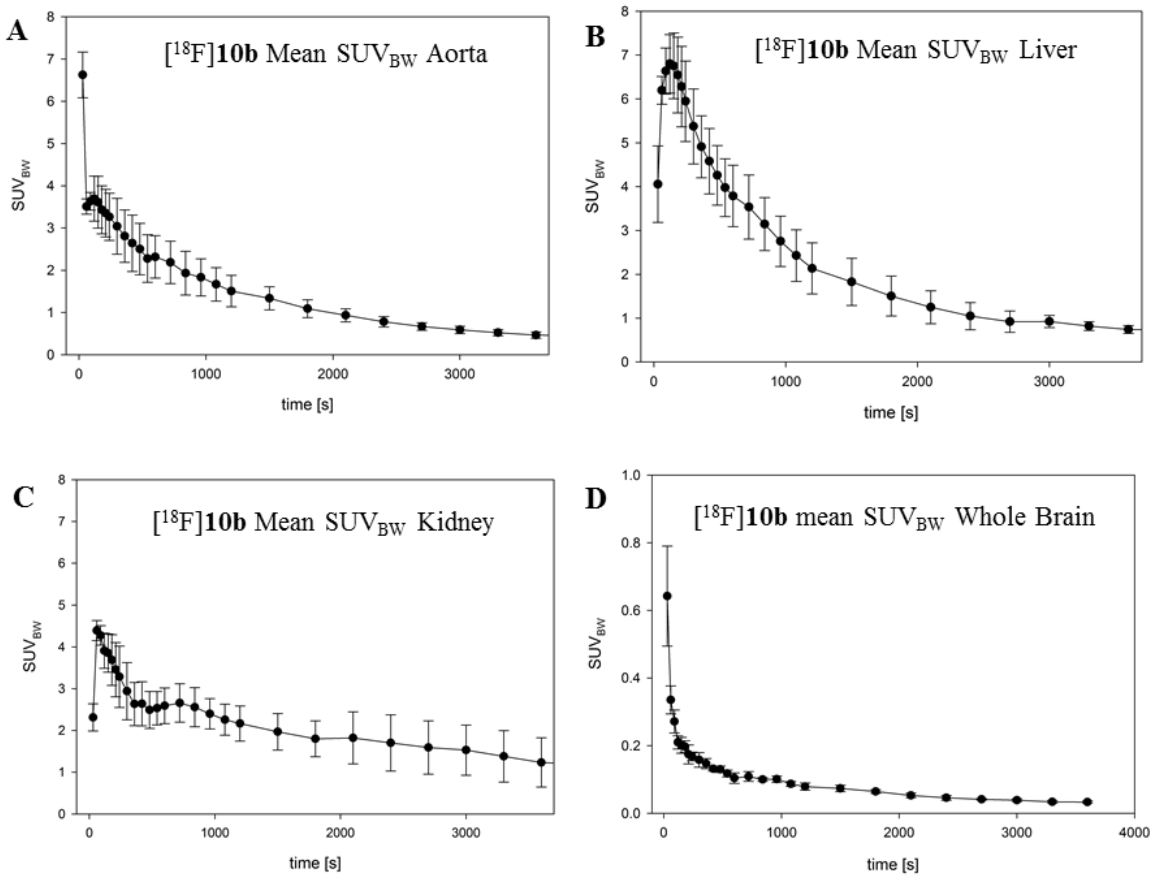

Figure 7. Time-activity curves following intravenous administration of [^{18}F]**10b** in rats. A. Aorta; B. Liver; C. Kidney and D. Whole brain

We also determined that [^{18}F]**10b** exhibits low initial BBB penetration and low brain uptake over the scanning time (max SUV_{BW} = 0.64 ± 0.148). TAC of whole brain activity was comparable to TAC from the blood pool indicating minimal but rapid delivery of the tracer to the brain and elimination following blood compartment kinetics. This minimal brain uptake is likely due to very limited crossing of the BBB and rapid

elimination from the plasma because the results of the *in vitro* binding studies indicate excellent specific binding to the TrkB receptor (*vide supra*). Cerebral time activity curves for [^{11}C]**10c** were similar to the ones for [^{18}F]**10b** with a small maximum SUV_{BW} of 0.70 and a comparably rapid elimination kinetics (Figure 8). Although the compounds are small molecules with a logD of 2.2±0.2 and 2.8±0.2 respectively, significant penetration of the BBB was not observed. Moreover, the low uptake in our studies may have been caused by trans-endothelial transport mechanisms with a longer time-constant than the tracer elimination from the plasma in combination with efflux transporter interaction, since many flavonoids derivatives are known to be P-glycoprotein substrates. [57-59] The observations derived from the *in vivo* PET experiments does not support the observation that 7,8-dihydroxyflavone derivatives significantly penetrate the BBB and challenges the hypothesis that those compounds modulate TrkB receptor in the CNS *in vivo*. [27-29, 33-37] These observations could support the assumption that *in vivo* TrkB modulation following 7,8-DHF derivatives treatment may be the indirect consequence of metabolites-TrkB interations, likely *O*-methylated metabolites from the 7- or 8-position with higher relative metabolic stability and brain permeation properties compared to the chemically unaltered catechol-bearing 7,8-DHF compounds. [71]

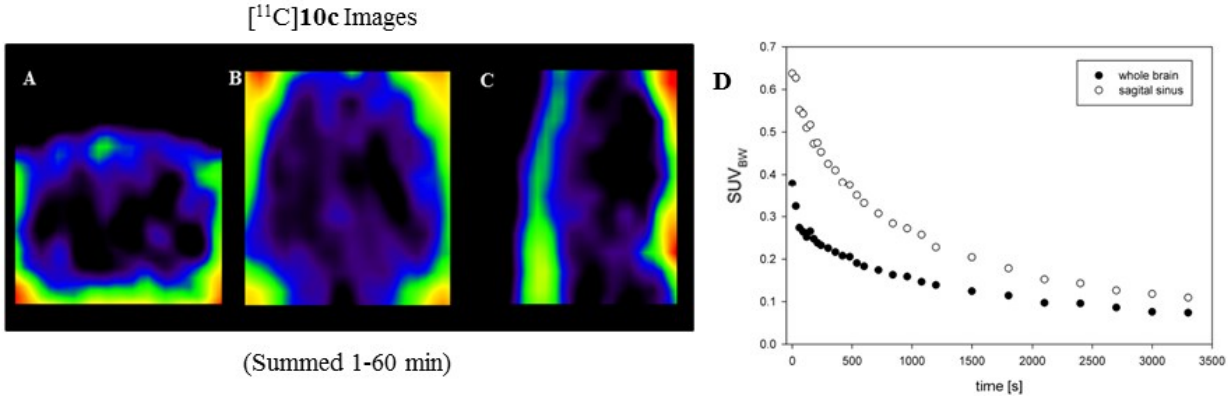

Figure 8. Coronal (**A**), horizontal (**B**) and sagittal (**C**) PET images of rat brain following intravenous injection of [^{11}C]**10c** (summed 1-60 min) D. Time-activity curve following intravenous administration of [^{11}C]**10c**.

3.5 Conclusion

The synthesis of ^{18}F- and ^{11}C-labeled 4'-substituted 7,8-dihydroxyflavone derivatives for micro-PET imaging in rats was successfully carried out. Radiolabeling of the nitro precursor followed by BBr_3-mediated double dimethoxy deprotection afforded [^{18}F]**10b** in high RCYs and demonstrated for the first time the feasibility of direct S_NAr radiofluorination involving a *para*-Michael acceptor substituted aryl system. [^{11}C]**10c** was synthesized via *N*-selective carbon-11 methylation in the presence of the free catechol fragment. Remarkably, *in vitro* autoradiography with [^{18}F]**10b** concomitant with blocking experiments involving the homologous compounds 7,8-DHF (**1a**) and BDNF showed that [^{18}F]**10b** binds TrkB-ECD with high specificity and selectivity. The ECD binding nature of this radioligand to TrkB in a BDNF displaceable manner represents a striking outcome regarding radiotracer development to image protein kinases. [^{18}F]**10b** and [^{11}C]**10c** micro-PET imaging in rats showed that those compounds are rapidly eliminated by hepatobilliary and renal excretion. The tracers were also associated with low initial brain penetration and brain uptake. However, taking into account the remarkable *in vitro* profile regarding TrkB selectivity and specificity, our results suggest that the carbon framework with 4'-radiolabelled substituents constitutes a promising scaffold for the further development of TrkB radioligands for PET.

3.6 Experimental Section

General Remarks. All moisture sensitive reactions were carried out in oven-dried flasks under nitrogen atmosphere with dry solvents. Reagents and solvents were purchased at the highest commercial quality from Sigma-Aldrich, Acros or Alfa-Aesar, and were used without further purification unless specified otherwise. Organic solutions were concentrated under reduced pressure on a Heidolph rotary evaporator. In general, reactions were magnetically stirred and monitored by TLC performed on pre-coated glass-backed TLC plates (Analtech, 250 microns) and chromatographic purification of products was accomplished using flash chromatography on Alfa-Aesar silica gel (230-450 mesh). TLC visualization was performed by fluorescence quenching, $KMnO_4$ or ninhydrin. ^{1}H NMR and ^{13}C NMR spectra were recorded on a 300 Varian Mercury spectrometer in $CDCl_3$ or d_6-DMSO and peak positions are given in parts per million using TMS as internal standard. ^{19}F NMR spectra were recorded on a 200 Varian Mercury in $CDCl_3$ or d_6-DMSO and peak positions are given in parts per million using $CFCl_3$ as internal standard. Peaks are reported as: s = singlet, d = doublet, t = triplet, q = quartet, p = quintet, m = multiplet, b = broad; coupling constant(s) in Hz; integration. High Resolution Mass Spectra (HRMS) were obtained from the Regional Center for Mass Spectrometry of The Chemistry Department of the Université de Montréal. Radio TLCs were monitored using Mini Gita (Raytest). Analytical and radio-preparative HPLC was performed on an Agilent 1200 system (Agilent Technologies, Santa Clara, CA, USA; running on Agilent ChemSattion software) equipped with a Raytest Gabi Star radioactivity detector (Raytest Isotopenmessgeräte GmbH, Straubenhardt, Germany) and a Chromolith Performance column (RP-18e, 100 x 4.6 mm; Merck, Germany). Gamma counting was performed using a CRC-25PET Dose Calibrator (Capintec, Ramsey, NJ, USA).

[^{11}C]MeI for radiolabeling was prepared by reducing cyclotron-produced [^{11}C]carbon dioxide ([^{11}C]CO_2); prepared by the $^{14}N(p,\alpha)^{11}C$ reaction with 0,5% O_2) with lithium aluminum hydride ($LiAlH_4$), followed by iodination with 57% hydroiodic acid. For the production of [^{11}C]MeOTf, a short glass column (4 mm ID, 95 mm) was partially filled (approximately one-third its volume) with a mixture of AgOTf (200 mg, 0.49 mmol)

and graphitized carbon (200 mg). The prepared column was placed in a commercially available synthesis unit (MEI plus by Bioscan, $[^{11}C]CH_3I$ is produced by conversion of $[^{11}C]CO_2$ with $LiAlH_4$ and HI) and heated up to 170°C in a stream of nitrogen for 5 min. $[^{11}C]CH_3I$ from the module, which was previously passed over a short drying column (5.0 g NaOH), was streamed through the AgOTf/C column and was bubbled (N_2 sweep flow of 10 mL/min) into a solution of precursor. No-carrier-added (n.c.a) aqueous $[^{18}F]$fluoride was prepared by the $^{18}O(p,n)^{18}F$ nuclear reaction on an enriched $[^{18}O]$water (95 %) target.

Regulatory Notice

All manipulations involving radioactive material have been performed in full accordance with Canadian Nuclear Safety Commission (CNSC) regulations.

Chemical Synthesis.

***General procedure for the synthesis of 6-acetyl-2,3-dimethoxyphenyl benzoate compounds* (6a-d).** To a solution of gallacetophenone 3',4'-dimethyl ether (1-(2-hydroxy-3,4-dimethoxyphenyl)ethanone) (589 mg, 3 mmol) in dry pyridine (3 mL) was added a solution of 4-subtituted benzoyl chloride (3.15 mmol, 1.05 equiv.) in dichloromethane (10 mL) dropwise over 15 minutes. The reaction mixture was stirred at room temperature until completion as monitored by TLC (typically 2-4 h). The reaction mixture was acidified with 1 N HCl (20 mL) and the phases were separated and the aqueous phase was extracted with dichloromethane (2 × 20 mL). The combined organic phases were washed with brine and dried over Na_2SO_4 and concentrated *in vacuo*. The crude products were purified by flash chromatography with a mixture of methanol and dichloromethane.

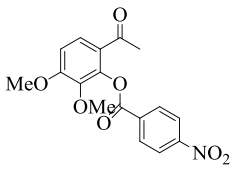

6-acetyl-2,3-dimethoxyphenyl 4-nitrobenzoate (6a). Following the general procedure described below, the title compound was obtained from 4-nitrobenzoyl chloride as an off-white solid (93 %).

^{1}H NMR (300 MHz, DMSO-d_6) δ 8.42 (d, J = 9.0 Hz, 2H), 8.35 (d, J = 8.7 Hz, 2H), 7.82 (d, J = 9.0 Hz, 1H), 7.16 (d, J = 8.7 Hz, 2H), 3.94 (s, 3H), 3.69 (s, 3H), 2.46 (s, 3H) ppm. ^{13}C NMR (75 MHz, DMSO-d_6) δ 196.0, 163.2, 157.3, 151.1, 143.3, 141.4, 134.5, 131.8, 127.4, 124.6, 123.5, 110.5, 61.1, 56.9, 29.4 ppm. HRMS (ESI) calcd for $C_{17}H_{16}NO_7$ $(M+H)^+$ 346.0921, found 346.0925.

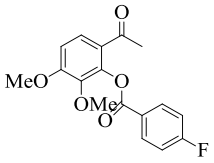

6-acetyl-2,3-dimethoxyphenyl 4-fluorobenzoate (6b). Following the general procedure described below, the title compound was obtained from 4-fluorobenzoyl chloride as a light brown solid (68 %).

^{1}H NMR (300 MHz, $CDCl_3$) δ 8.24 (m, 2H), 7.63 (d, *J* = 9.0 Hz, 2H), 7.18 (m, 2H), 6.87 (d, *J* = 9.0 Hz, 2H), 3.91 (s, 3H), 3.80 (s, 3H), 2.46 (s, 3H) ppm. ^{13}C NMR (75 MHz, $CDCl_3$) δ 195.7, 166.2 (d, *J* = 253 Hz), 163.8, 157.2, 144.2, 141.5, 133.0 (d, *J* = 9.5 Hz), 126.2, 125.5, 124.3, 115.9 (d, *J* = 22.0 Hz), 109.1, 61.0, 56.1, 29.5 ppm. ^{19}F NMR (188 MHz, $CDCl_3$) δ -104.3 ppm. HRMS (ESI) calcd for $C_{17}H_{15}FNaO_5$ $(M+Na)^+$ 341.0796, found 341.0799.

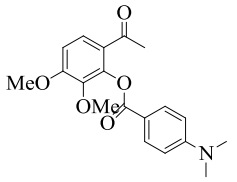

6-acetyl-2,3-dimethoxyphenyl 4-(dimethylamino)benzoate (6c). Following the general procedure described below, the title compound was obtained from 4-(dimethylamino)benzoyl chloride as a yellow solid (87 %).

^{1}H NMR (300 MHz, $CDCl_3$) δ 8.10 (d, *J* = 9.0 Hz, 2H), 7.68 (d, *J* = 8.7 Hz, 1H), 6.87 (d, *J* = 9.0 Hz, 1H), 6.71 (d, *J* = 9.0 Hz, 2H), 3.93 (s, 3H), 3.80 (s, 3H), 3.08 (s, 6H), 2.49 (s, 1H) ppm. ^{13}C NMR (75 MHz, $CDCl_3$) δ 196.2, 164.7, 157.2, 153.9, 145.1, 141.5, 132.3, 125.6, 125.4, 115.3, 110.9, 109.0, 60.8, 56.1, 40.1, 30.3 ppm. HRMS (ESI) calcd for $C_{19}H_{22}NNaO_5$ $(M+Na)^+$ 366.1312, found 366.1315.

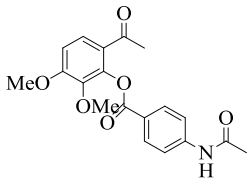

6-acetyl-2,3-dimethoxyphenyl 4-acetamidobenzoate (6d). Following the general procedure described below, the title compound was obtained from 4-acetamidobenzoyl chloride as a light brown solid (34 %).

^{1}H NMR (300 MHz, $CDCl_3$) δ 8.13 (d, *J* = 8.4 Hz, 2H), 7.98 (bs, 1H), 7.67 (d, *J* = 9.0 Hz, 1H), 7.63 (d, *J* = 8.7 Hz, 2H), 6.88 (d, *J* = 9.0 Hz, 1H), 3.94 (s, 3H), 3.80 (s, 3H), 2.94 (s, 3H), 2.16 (s, 3H) ppm. ^{13}C NMR (75 MHz, $CDCl_3$) δ 196.2, 168.8, 164.3, 157.3, 144.4, 143.1, 141.5, 131.6, 126.1, 124.6, 124.0, 118.9, 109.1, 61.0, 56.2, 29.8, 24.7 ppm. HRMS (ESI) calcd for $C_{19}H_{19}NNaO_6$ $(M+Na)^+$ 380.1105, found 380.1103.

***General procedure for the synthesis of 1-(2-hydroxy-3,4-dimethoxyphenyl)-3-phenylpropane-1,3-dione compounds* (7a-d).** To a solution of 6-acetyl-2,3-dimethoxyphenyl benzoate intermediate (3.0 mmol) in pyridine (5-10 mL) was added anhydrous powdered potassium hydroxide (254 mg, 4.5 mmol, 1.5 equiv.) and the reaction mixture was stirred at 50°C for 12 h. The reaction mixture was cooled at room temperature and quenched with 1M HCl, extracted with ethyl acetate (3 × 30 mL). The combined organic phases were washed with brine and dried over Na_2SO_4 and concentrated *in vacuo*. The crude products were purified by flash chromatography with a mixture of methanol and dichloromethane.

The 1-(4-(dimethylamino)phenyl)-3-(2-hydroxy-3,4-dimethoxyphenyl)propane-1,3-dione **(7c)** and N-(4-(3-(2-hydroxy-3,4-dimethoxyphenyl)-3-oxopropanoyl)phenyl)acetamide **(7d)** were purified by flash chromatography and carried forward without characterisation. The 1-(2-hydroxy-3,4-dimethoxyphenyl)-3-(4-nitrophenyl)propane-1,3-dione **(7a)** and the 1-(4-fluorophenyl)-3-(2-hydroxy-3,4-dimethoxyphenyl)propane-1,3-dione **(7b)** were purified and characterized as follow.

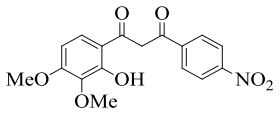

1-(2-hydroxy-3,4-dimethoxyphenyl)-3-(4-nitrophenyl)propane-1,3-dione (7a). Following the general procedure described below, the title compound was obtained from 6-acetyl-2,3-dimethoxyphenyl 4-nitrobenzoate **(6a)** as a yellow solid (95 %).

^{1}H NMR (300 MHz, $CDCl_3$; diketo/enol = 3:97) δ 12.56 (s, 1H), 12.11 (s, 1H), 8.32 (d, *J* = 9.0 Hz, 2H), 8.07 (d, *J* = 8.7 Hz, 2H), 7.57 (d, *J* = 9.3 Hz, 1H), 6.81 (s, 1H), 6.55 (d,

J = 9.3 Hz, 1H), 4.63 (*minor diketo*; s, 2H, COC*H*$_2$CO) 3.96 (s, 3H), 3.91 (s, 3H), 3.87 (*minor diketo*; s, 3H, Ar-OC*H*$_3$), 3.83 (*minor diketo*; s, 3H, Ar-OC*H*$_3$) ppm. ^{13}C NMR (75 MHz, $CDCl_3$) δ 195.0, 172.7, 158.8, 157.3, 149.6, 139.7, 136.9, 127.6, 125.1, 123.9, 114.1, 103.5, 94.2, 60.7, 56.2, 56.1 (*minor diketo*; CO*C*H$_2$CO) ppm. HRMS (ESI) calcd for $C_{17}H_{16}NO_7$ $(M+H)^+$ 346.0923, found 346.0921.

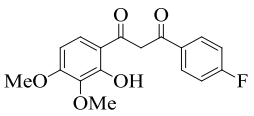

1-(4-fluorophenyl)-3-(2-hydroxy-3,4-dimethoxyphenyl)propane-1,3-dione (7b). Following the general procedure described below, the title compound was obtained from 6-acetyl-2,3-dimethoxyphenyl 4-fluorobenzoate **(6b)** as a yellow solid (90 %).

^{1}H NMR (300 MHz, $CDCl_3$; diketo/enol = 10:90) δ 12.80 (s, 1H), 12.13 (s, 1H), 8.05 (*minor diketo*; m, 2H, *m*-Ar-F), 7.92 (m, 2H), 7.58 (*minor diketo*; d, *J* = 9.3 Hz, 1H, 5-C*H*), 7.52 (d, *J* = 9.0 Hz, 1H), 7.14 (t, *J* = 8.7 Hz, 2H), 6.67 (s, 1H), 6.50 (d, *J* = 9.3 Hz, 1H), 4.54 (*minor diketo*; s, 2H, COC*H*$_2$CO), 3.93 (s, 3H), 3.92 (*minor diketo*; s, 3H, Ar-OC*H*$_3$), 3.90 (s, 3H), 3.86 (*minor diketo*; s, 3H, Ar-OC*H*$_3$) ppm. ^{13}C NMR (75 MHz, $CDCl_3$) δ 194.5, 192.0 (*minor diketo*; OCH$_2$*C*OArF), 175.3, 165.2 (d, *J* = 252 Hz), 158.2, 157.0, 136.8, 131.7 (*minor diketo*; d, *J* = 9.5 Hz, *m*-ArF), 129.9 (d, *J* = 3.1 Hz), 129.0 (d, *J* = 9.0 Hz), 127.6 (*minor diketo*; 5-*C*H*)*, 124.7, 116.0 (*minor diketo*; d, *J* = 21.8 Hz, *o*-ArF), 115.9 (d, *J* = 21.8 Hz), 114.0, 103.4 (*minor diketo*; 4-*C*H), 103.2, 91.9, 60.7, 56.1, 50.1 (*minor diketo*; CO*C*H$_2$CO) ppm. ^{19}F NMR (188 MHz, $CDCl_3$) δ -106.6, -103.4 83 (*minor diketo*) ppm. HRMS (ESI) calcd for $C_{17}H_{15}FNaO_5$ $(M+Na)^+$ 341.0796, found 341.0812.

General procedures for the synthesis of 7,8-dimethoxy-2-phenyl-4H-chromen-4-one compounds **(8a-d) Procedure A**. To a solution of 1-(2-hydroxy-3,4-dimethoxyphenyl)-3-phenylpropane-1,3-dione intermediate (3.0 mmol) in glacial acetic acid (10.0 mL) was added concentrated sulfuric acid (0.1 mL) and the reaction mixture was refluxed for 1 – 3 h. The reaction mixture was cooled and poured into ice and extracted with ethyl

acetate. The combined organic phases were washed with brine, dried over Na_2SO_4 and concentrated *in vacuo*. The crude products were purified by flash chromatography with a mixture of methanol and dichloromethane. **Procedure B**. A solution of (*E*)-1-(2-hydroxy-3,4-dimethoxyphenyl)-3-phenylprop-2-en-1-one intermediate (3.0 mmol) and iodine (0.01 equiv.) in DMSO (3.0 mL) stirred at 130°C for 5 - 6 h. The reaction mixture was cooled diluted with water extracted with dichloromethane and washed with aqueous saturated $Na_2S_2O_3$. The combined organic phases were dried over Na_2SO_4 and concentrated *in vacuo*. The crude products were purified by recrystallization with a mixture of dichloromethane and hexane or by flash chromatography with a mixture of methanol and dichloromethane.

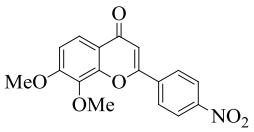

7,8-dimethoxy-2-(4-nitrophenyl)-4H-chromen-4-one (8a). Following the general procedure A described below, the title compound was obtained from 1-(2-hydroxy-3,4-dimethoxyphenyl)-3-(4-nitrophenyl)propane-1,3-dione as an amorphous pale yellow solid (41 %). Following procedure B, the title compound was isolated as an amorphous pale yellow solid (50 %).

^{1}H NMR (300 MHz, DMSO-d_6) δ 8.37 (d, J = 9.0 Hz, 2H), 8.29 (d, J = 9.0 Hz, 2H), 7.76 (d, J = 9.0 Hz, 1H), 7.28 (d, J = 9.0 Hz, 1H), 7.13 (s, 1H), 3.94 (s, 6H) ppm. ^{13}C NMR (75 MHz, DMSO-d_6) δ 177.0, 160.2, 157.2, 150.3, 149.4, 137.7, 136.8, 128.0, 124.6, 120.7, 118.3, 111.5, 109.1, 61.7, 56.9 ppm. HRMS (ESI) calcd for $C_{17}H_{14}NO_6$ $(M+H)^+$ 328.0816, found 328.0810.

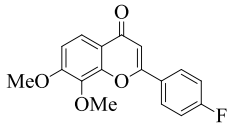

2-(4-fluorophenyl)-7,8-dimethoxy-4H-chromen-4-one (8b). Following the general procedure A described below, the title compound was obtained from 1-(4-fluorophenyl)-3-(2-hydroxy-3,4-dimethoxyphenyl)propane-1,3-dione as an amorphous off-white solid

(40 %). Following procedure B, the title compound was isolated as off-white needles (75 %).

^{1}H NMR (300 MHz, DMSO-d_6) δ 8.11 (m, 2H), 7.75 (d, J = 9.0 Hz, 1H), 7.43 (d, J = 8.7 Hz, 2H), 7.26 (d, J = 9.0 Hz, 1H), 6.95 (s, 1H), 3.94 (s, 3H), 3.93 (s, 3H) ppm. ^{13}C NMR (75 MHz, DMSO-d_6) δ 177.1, 164.65 (d, J = 249 Hz), 161.6, 156.9, 150.2, 136.8, 129.2 (d, J = 9.1 Hz), 128.3 (d, J = 2.9 Hz), 120.7, 118.2, 116.7 (d, J = 42.2 Hz), 111.2, 106.7, 61.6, 56.9 ppm. ^{19}F NMR (188 MHz, $CDCl_3$) δ -108.25 ppm. HRMS (ESI) calcd for $C_{17}H_{14}FO_4$ $(M+H)^+$ 197.0808, found 197.0807.

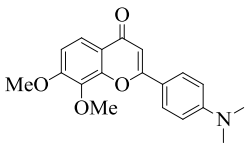

2-(4-(dimethylamino)phenyl)-7,8-dimethoxy-4H-chromen-4-one (8c). Following the general procedure A described below, the title compound was obtained from 1-(4-(dimethylamino)phenyl)-3-(2-hydroxy-3,4-dimethoxyphenyl)propane-1,3-dione (not isolated) as an amorphous orange solid (44 %, 2 steps). Following procedure B, the title compound was isolated as orange needles (78 %).

^{1}H NMR (300 MHz, DMSO-d_6) δ 7.87 (d, J = 8.7 Hz, 2H), 7.72 (d, J = 8.7 Hz, 1H), 7.20 (d, J = 9.0 Hz, 1H), 6.81 (d, J = 9.0 Hz, 2H), 6.70 (s, 1H), 3.93 (s, 3H), 3.92 (s, 3H), 3.00 (s, 6H) ppm. ^{13}C NMR (75 MHz, DMSO-d_6) δ 176.7, 163.5, 156.5, 152.8, 150.1, 136.7, 127.9, 120.5, 118.5, 117.6, 112.2, 110.7, 103.1, 61.5, 56.8, 55.3 ppm. HRMS (ESI) calcd for $C_{19}H_{20}NO_4$ $(M+H)^+$ 326.1387, found 326.1390.

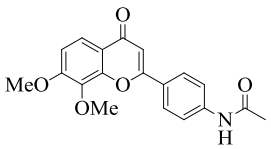

***N*-(4-(7,8-dimethoxy-4-oxo-4H-chromen-2-yl)phenyl)acetamide (8d).** Following the general procedure A described below, the title compound was obtained from *N*-(4-(3-(2-hydroxy-3,4-dimethoxyphenyl)-3-oxopropanoyl)phenyl)acetamide (not isolated) as an amorphous orange solid (31 %, 2 steps).

^{1}H NMR (300 MHz, DMSO-d_6) δ 10.51 (s, 1H), 7.99 (d, J = 8.4 Hz, 2H), 7.81 (d, J = 8.4 Hz, 2H), 7.74 (d, J = 9.3 Hz, 1H), 7.24 (d, J = 9.0 Hz, 1H), 6.86 (s, 1H), 3.93 (s, 6H), 2.09 (s, 3H) ppm. ^{13}C NMR (75 MHz, DMSO-d_6) δ 177.0, 169.5, 162.5, 156.8, 150.2, 143.1, 136.8, 127.4, 125.7, 120.6, 119.4, 118.4, 111.1, 105.5, 61.6, 56.8, 24.6 ppm. HRMS (ESI) calcd for $C_{19}H_{18}NO_5$ $(M+H)^+$ 340.1180, found 340.1185.

General procedure for the synthesis of (E)-1-(2-hydroxy-3,4-dimethoxyphenyl)-3-phenylprop-2-en-1-one compounds **(9a-c).** To a solution of gallacetophenone 3',4'-dimethyl ether (1-(2-hydroxy-3,4-dimethoxyphenyl)ethanone) (491 mg, 2.5 mmol) and arylaldehyde (1 equiv.) in methanol (10 mL) was added $Ba(OH)_2$ (428 mg, 2.5 mmol, 1 equiv.) at room temperature. The temperature was raised to 40°C and the reaction mixture was stirred at this temperature for 24h. The volatiles were removed under reduced pressure and the residue was diluted with 1N HCl and extracted with ethyl acetate. The combined organic phases were washed with brine and dried over Na_2SO_4 and concentrated *in vacuo*. The crude solids were either purified by recrystallization from ethyl acetate/hexane or by flash chromatography with a mixture of methanol and dichloromethane.

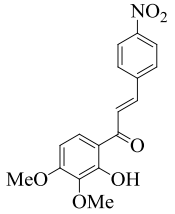

(*E*)-1-(2-hydroxy-3,4-dimethoxyphenyl)-3-(4-nitrophenyl)prop-2-en-1-one (9a). Following the general procedure described below, the title compound was obtained from 4-nitrobenzaldehyde as an amorphous orange solid (82 %).

^{1}H NMR (300 MHz, DMSO-d_6) δ 12.86 (s, 1H), 8.24 – 8.07 (m, 6H), 7.82 (d, J = 15.3 Hz, 1H), 6.70 (d, J = 9.3 Hz, 1H), 3.88 (s, 3H), 3.69 (s, 3H) ppm. ^{13}C NMR (75 MHz, DMSO-d_6) δ 192.5, 159.3, 157.5, 148.5, 141.6, 141.4, 136.2, 130.5, 128.1, 125.9, 124.3,

115.7, 104.3, 60.3, 56.6 ppm. HRMS (ESI) calcd for $C_{17}H_{16}NO_6$ $(M+H)^+$ 330.0973, found 330.0972.

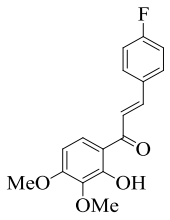

(*E*)-3-(4-fluorophenyl)-1-(2-hydroxy-3,4-dimethoxyphenyl)prop-2-en-1-one (9b). Following the general procedure described below, the title compound was obtained from 4-dimethylaminobenzaldehyde as bright yellow needles (75 %).

^{1}H NMR (300 MHz, $CDCl_3$) δ 13.2 (d, J = 1.8 Hz, 1H), 7.85 (d, J = 15.3 Hz, 1H), 7.69 – 7.62 (m, 3H), 7.50 (d, J = 15.3 Hz, 1H), 7.11 (td, J_2 = 8.7 Hz, J_1 = 1.8 Hz, 2H), 6.53 (d, J_2 = 9.0 Hz, J_1 = 1.8 Hz, 1H), 3.95 (d, J = 1.8 Hz, 3H), 3.92 (d, J = 1.8 Hz, 3H) ppm. ^{13}C NMR (75 MHz, $CDCl_3$) δ 192.2, 164.2 (d, J = 251 Hz), 158.5 (d, J = 25.1 Hz), 143.4, 136.7, 130.9 (d, J = 3.0 Hz), 130.5 (d, J = 8.6 Hz), 126.0, 119.9 (d, J = 2.3 Hz), 116.2 (d, J = 21.8 Hz), 115.5, 105.0, 102.9, 60.7, 56.2 ppm. ^{19}F NMR (188 MHz, $CDCl_3$) δ -108.58 ppm. HRMS (ESI) calcd for $C_{17}H_{16}FO_4$ $(M+H)^+$ 303.1027, found 303.1024.

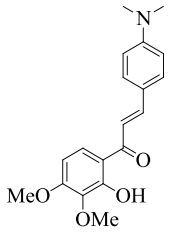

(*E*)-3-(4-(dimethylamino)phenyl)-1-(2-hydroxy-3,4-dimethoxyphenyl)prop-2-en-1-one (9c). Following the general procedure described below, the title compound was obtained from 4-dimethylaminobenzaldehyde as bright orange flat crystals (80 %).

^{1}H NMR (300 MHz, $CDCl_3$) δ 13.61 (s, 1H), 7.88 (d, J = 15.3 Hz, 1H), 7.69 (d, J = 9.3 Hz, 1H), 7.55 (d, J = 8.7 Hz, 2H), 7.36 (d, J = 15.3 Hz, 1H), 6.68 (d, J = 8.7 Hz, 2H), 6 .51 (d, J = 9.3 Hz, 1H), 3.94 (s, 1H), 3.92 (s, 1H), 3.05 (s, 6H) ppm. ^{13}C NMR (75 MHz,

$CDCl_3$) δ 192.4, 158.2, 158.0, 152.2, 145.8, 135.9, 130.7, 125.6, 122.4, 115.9, 114.3, 111.8, 102.5, 60.7, 56.1, 40.1 ppm. HRMS (ESI) calcd for $C_{19}H_{22}NO_4$ $(M+H)^+$ 327.1549, found 328.1547.

General procedure for the synthesis of the 7,8-dihydroxy-2-phenyl-4H-chromen-4-one compounds **(10a-c)**. To an ice-cold solution of 7,8-dimethoxy-2-phenyl-4H-chromen-4-one intermediate (0.5 mmol) in dichloromethane (10 mL) was added boron tribromide (1 M in dichloromethane, 4 equiv.). The reaction mixture was stirred at room temperature overnight. The reaction was quenched with water and extracted with ethyl acetate several times, dried over Na_2SO_4 and concentrated *in vacuo*. The crude product was purified by flash chromatography with a mixture of methanol and dichloromethane.

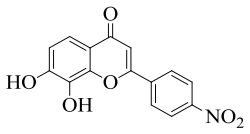

7,8-dihydroxy-2-(4-nitrophenyl)-4H-chromen-4-one (10a). Following the general procedure described below, the title compound was obtained from 7,8-dimethoxy-2-(4-nitrophenyl)-4H-chromen-4-one as an orange amorphous solid (70 %).

^{1}H NMR (300 MHz, DMSO-d_6) δ 8.40 (d, J = 9.0 Hz, 2H), 8.35 (d, J = 9.0 Hz, 2H), 7.39 (d, J = 8.7 Hz, 1H), 7.06 (s, 1H), 6.95 (d, J = 8.7 Hz, 1H) ppm. ^{13}C NMR (75 MHz, DMSO-d_6) δ 177.2, 159.7, 151.3, 149.3, 147.0, 137.9, 133.6, 128.1, 124.4, 117.3, 115.6, 114.8, 108.8 ppm HRMS (ESI) calcd for $C_{15}H_{10}NO_6$ $(M+H)^+$ 300.0503, found 300.0512.

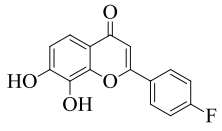

2-(4-fluorophenyl)-7,8-dihydroxy-4H-chromen-4-one (10b). Following the general procedure described below, the title compound was obtained from 2-(4-fluorophenyl)-7,8-dimethoxy-4H-chromen-4-one as white amorphous solid (98 %).

^{1}H NMR (300 MHz, DMSO-d_6) δ 10.30 (s, 1H), 9.50 (s, 1H), 8.21(m, 2H), 7.39 (m, 3H), 6.93 (d, J = 8.7 Hz, 1H), 6.88 (s, 1H) ppm. ^{13}C NMR (75 MHz, DMSO-d_6) δ 177.3, 161.2, 151.0, 147.0, 1335, 129.4 (d, J = 8.8 Hz), 128.5, 117.3, 116.7, 116.4, 115.1 (d, J = 77.9 Hz), 106.4 ppm. ^{19}F NMR (188 MHz, $CDCl_3$) δ -108.75 ppm. HRMS (ESI) calcd for $C_{15}H_{10}FO_4$ $(M+H)^+$ 273.0558, found 273.0554.

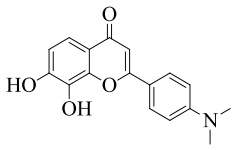

2-(4-(dimethylamino)phenyl)-7,8-dihydroxy-4H-chromen-4-one (10c). Following the general procedure described below, the title compound was obtained from 2-(4-(dimethylamino)phenyl)-7,8-dimethoxy-4H-chromen-4-one as a red amorphous solid (66 %).

^{1}H NMR (300 MHz, DMSO-d_6) δ 10.21 (s, 1H), 9.34 (s, 1H), 7.95 (d, J = 9.0 Hz, 2H), 7.33 (d, J = 8.7 Hz, 1H), 6.89 (d, J = 8.7 Hz, 1H), 6.80 (d, J = 9.3 Hz, 2H), 6.63 (s, 1H), 3.01 (s, 6H) ppm. ^{13}C NMR (75 MHz, DMSO-d_6) δ 177.0, 163.2, 152.7, 150.6, 146.9, 133.4, 128.1, 118.0, 117.4, 115.4, 114.0, 112.0, 103.0, 55.4 ppm. HRMS (ESI) calcd for $C_{17}H_{16}NO_4$ $(M+H)^+$ 298.1074, found 298.1072.

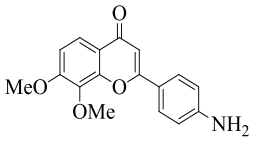

2-(4-aminophenyl)-7,8-dimethoxy-4H-chromen-4-one (11). A mixture of 7,8-dimethoxy-2-(4-nitrophenyl)-4H-chromen-4-one (1.96 g, 6 mmol), $SnCl_2.2H_2O$ (6.76 g, 30 mmol, 5 equiv.) and ethanol (60 mL) was stirred under reflux for 8 h. The reaction mixture was cooled at room temperature and concentrated *in vacuo*. Water was added to the mixture and the pH was adjusted to pH = 8-9 with $NaHCO_3$ saturated solution and extracted several times with ethyl acetate. The combined organic phases were dried over Na_2SO_4 and concentrated *in vacuo* to afford 844 mg of the title compound as bright orange solid (47 %).

^{1}H NMR (300 MHz, DMSO-d_6) δ 7.74 (d, J = 9.0 Hz, 2H), 7.71 (d, J = 8.7 Hz, 1H), 7.19 (d, J = 9.0 Hz, 1H), 6.67 (d, J = 8.7 Hz, 2H), 6.62 (s, 1H), 6.01 (s, 2H), 3.92 (s, 3H), 3.91 (s, 3H) ppm. ^{13}C NMR (75 MHz, DMSO-d_6) δ 176.7, 163.8, 156.5, 153.0, 150.1, 136.7, 128.2, 120.4, 118.5, 117.5, 114.0, 110.6, 102.7, 61.6, 56.8 ppm. HRMS (ESI) calcd for $C_{17}H_{16}NO_4$ $(M+Na)^+$ 320.0893, found 320.0894.

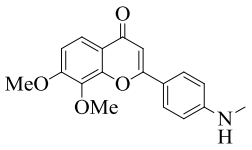

7,8-dimethoxy-2-(4-(methylamino)phenyl)-4H-chromen-4-one (12). To a solution of *N*-(4-(7,8-dimethoxy-4-oxo-4H-chromen-2-yl)phenyl)acetamide (20 mg, 0.058 mmol) at 0°C in THF (1 mL) was added sodium hydride in one portion (7.0 mg, 2 equiv., 60% dispersion in mineral oil). The reaction mixture was stirred for 15 min at this temperature and methyl iodide (25.5 μL, 15 equiv.) was added. The reaction mixture was brought at room temperature and stirred for 4 h and then quenched with water and extracted with dichloromethane. The organic phases were washed with brine and dried over Na_2SO_4 and concentrated *in vacuo.* The crude residue was then dissolved in ethylene glycol (1 mL) and stirred at room temperature and conc. HCl (333 μL) was added. The reaction mixture was refluxed for 2 h. The reaction was diluted with water and extracted with dichloromethane. The organics were washed with brine and dried over Na_2SO_4 and concentrated *in vacuo* to afford 18 mg of the title compound as a yellow solid (81 %, 2 steps). Alternatively, to a solution of 2-(4-aminophenyl)-7,8-dimethoxy-4H-chromen-4-one (297 mg, 1 mmol) and paraformaldehyde (150 mg, 5 mmol, 5 equiv.) in methanol (15 mL), was added sodium methoxide (0.3 mL, 25 wt. % in methanol, ≈ 1.4 mmol, ≈ 1.4 equiv.) dropwise. The reaction mixture was refluxed for 1 h and cooled at room temperature and sodium borohydride (170 mg, 4.5 mmol, 4.5 equiv.) was added in one portion and the reaction mixture was refluxed for 2 h. The reaction mixture was cooled at room temperature and quenched with 1M NaOH and extracted with ethyl acetate. The combined organic phases were dried over Na_2SO_4 and concentrated *in vacuo*. The crude residue was purified by flash chromatography

(methanol/dichloromethane) to afford 266 mg of the title compound as a yellow solid (86 %, 2 steps).

^{1}H NMR (300 MHz, $CDCl_3$) δ 7.93 (d, *J* = 9.0 Hz, 1H), 7.81 (d, *J* = 8.7 Hz, 2H), 7.01 (d, *J* = 8.7 Hz, 1H), 6.67 (d, *J* = 8.7 Hz, 2H), 6.62 (s, 1H), 4.03 (s, 3H), 3.99 (s, 3H), 2.90 (s, 3H) ppm. ^{13}C NMR (75 MHz, $CDCl_3$) δ 178.1, 163.9, 156.3, 152.0, 150.4, 136.8, 127.9, 120.9, 119.6, 118.8, 112.0, 109.4, 103.8, 61.6, 56.4, 30.2 ppm. HRMS (ESI) calcd for $C_{18}H_{18}NO_4$ $(M+H)^+$ 312.1230, found 312.1229.

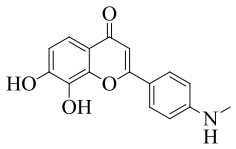

7,8-dihydroxy-2-(4-(methylamino)phenyl)-4H-chromen-4-one (13). Following the general procedure described the synthesis of **10a-c**, the title compound was obtained from 7,8-dimethoxy-2-(4-(methylamino)phenyl)-4H-chromen-4-one as a yellow amorphous solid (92 %).

^{1}H NMR (300 MHz, DMSO-d_6) δ 10.17 (s, 1H), 9.29 (s, 1H), 7.86 (d, *J* = 9.0 Hz, 2H), 7.32 (d, *J* = 8.7 Hz, 1H), 6.87 (d, *J* = 8.7 Hz, 1H), 6.62 (d, *J* = 8.7 Hz, 2H), 6.51 (s, 1H), 6.49 (m, 1H), 2.72 (d, *J* = 4.5 Hz, 3H), ppm. ^{13}C NMR (75 MHz, DMSO-d_6) δ 176.9, 163.4, 153.0, 150.5, 146.8, 133.3, 128.3, 117.8, 117.4, 115.4, 113.9, 111.7, 102.5, 29.7 ppm. HRMS (ESI) calcd for $C_{16}H_{13}NNaO_4$ $(M+H)^+$ 306.0737, found 306.0737.

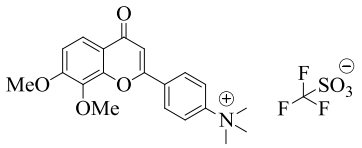

4-(7,8-dimethoxy-4-oxo-4H-chromen-2-yl)-*N,N,N*-trimethylbenzenaminium triflate (14). To a solution of 2-(4-(dimethylamino)phenyl)-7,8-dimethoxy-4H-chromen-4-one (70 mg, 0.22 mmol) in dichloromethane (2 mL) at room temperature was added methyl trifluoromethanesulfonate (30 μL, 0.26 mmol, 1.2 equiv.) dropwise. The reaction mixture was stirred at this temperature for 4 h and the volatiles were removed *in vacuo*

and taken in diethyl ether and filtrated. 90 mg of the tiltle compound was obtained as a red amorphous solid (84 %).

^{1}H NMR (300 MHz, DMSO-d_6) δ 7.86 d, J = 9.0 Hz, 2H), 7.50 (d, J = 9.0 Hz, 2H), 7.29 (d, J = 8.7 Hz, 1H), 7.15 (s 1H), 6.97 (d, J = 8.7 Hz, 2H), 3.98 (s, 3H), 3.95 (s, 1H), 3.65 (s, 9H) ppm. ^{13}C NMR (75 MHz, DMSO-d_6) δ 172.2, 171.6, 158.7, 155.9, 146.5, 136.3, 132.2, 128.2, 122.1, 119.1, 114.7, 113.9, 113.0, 111.6, 60.3, 57.5, 56.8 ppm. HRMS (ESI) calcd for $C_{20}H_{22}NO_4$ $(M^*)^+$ 340.1543, found 340.1557.

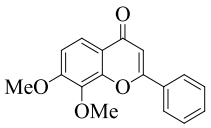

7,8-dimethoxy-2-phenyl-4H-chromen-4-one (15). To a solution of 7,8-dihydroxy-2-phenyl-4H-chromen-4-one (7,8-dihydroxyflavone) (254 mg, 1 mmol) in DMF (5.0 mL) was added methyl iodide (0.25 mL, 4 mmol, 4 equiv.) and K_2CO_3 (1.11 g, 8 mmol, 8 equiv.). The reaction mixture was stirred at room temperature for 2 h. DMF was evaporated *in vacuo* and water (30 mL) was added to the crude mixture followed by extraction with ethyl acetate (3 × 30 mL). The combined organic phases were washed with brine and dried over Na_2SO_4 and concentrated *in vacuo*. The title compound was obtained after recrystallization from ethyl acetate as greenish needles (264 mg, 94 %).

^{1}H NMR (300 MHz, DMSO-d_6) δ 8.03 (m, 2H), 7.48 (d, J = 9.0 Hz, 1H), 7.54 (m, 3H), 7.25 (d, J = 9.0 Hz, 1H), 6.94 (s, 1H), 3.93 (s, 3H), 3.92 (s, 3H) ppm. ^{13}C NMR (75 MHz, DMSO-d_6) δ 177.1, 162.5, 156.9, 150.3, 136.8, 132.2, 131.7, 129.7, 126.6, 120.6, 118.4, 111.2, 106.8, 61.6, 56.9 ppm. HRMS (ESI) calcd for $C_{17}H_{14}NaO_4$ $(M+Na)^+$ 305.0790, found 305.0784.

Radiochemistry.

2-(4-[^{18}F]fluorophenyl)-7,8-dimethoxy-4H-chromen-4-one ([^{18}F]8b). Procedure for the Labeling of 8b (a similar procedure was used for the labeling 14 during

optimization conditions). [^{18}F]Fluoride was produced using an IBA cyclotron (Cyclon 18/9) by the ^{18}O(p,n)^{18}F nuclear reaction on an enriched [^{18}O]water target and passed through a Sep-Pak Light QMA cartridge (Waters) as an aqueous solution in ^{18}O-enriched water. The cartridge was then dried by airflow, and the ^{18}F activity was eluted with 1.0 mL (from a 10.0 mL stock solution) of a Kryptofix 222/K_2CO_3 solution (22.6 mg of Kryptofix 222 and 4.2 mg of K_2CO_3 in acetonitrile/water (95/5)) in a 5.0 mL conical vial with a stirring bar. The solvent was removed at 100°C under reduced pressure, agitation and a stream of argon gas. The residue was azeotropically dried with 1.0 mL of anhydrous acetonitrile twice at 100°C under a stream of argon gas and dissolved in 300 µL of DMF solution containing 2.0 mg of **8b** and the reaction mixture was heated at 150°C for 25 min. Subsequently, the vial was rapidly cooled to room temperature in a dry-ice/acetone bath and the reaction mixture was diluted with 10 mL of water and passed through a preconditioned (10 mL EtOH followed by 10 mL water) Sep-Pak C18 Plus Cartridge and the labeled compound **[^{18}F]8b** was eluted with 2.0 mL of acetonitrile into a 5.0 mL conical vial. Radiofluorination was confirmed by HPLC on a Chromolith® HPLC RP-18a performance column (100X4.6 mm) using a H_2O+0.1% TFA (A)/MeCN +0.1% TFA (B) gradient (t = 0 min: 100% A to t = 10 min A = 0%) at 4.0 mL/min (t_r = 5.05 min) with typical yields of about 80-90% (HPLC determination).

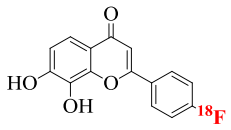

2-(4-[^{18}F]fluorophenyl)-7,8-dihydroxy-4H-chromen-4-one ([^{18}F]10b). Procedure for the deprotection of [^{18}F]8b. The acetonitrile (2.0 mL), from the collected [^{18}F]**8b** as previously described, was then removed at 100°C under reduced pressure, agitation and a stream of argon gas. The residue was maintained under argon and dissolved in a mixture of BBr_3 (0.5 mL of a 1.0M solution in CH_2Cl_2) and CH_2Cl_2 (0.5 mL) and the reaction mixture was heated at 70°C for 15 min. The stream of argon was removed during the reaction. After 15 min, the reaction was cooled to room temperature in a dry-ice/acetone bath and carefully depressurized (HBr evolution) with a needle through the

septum. Subsequently, the mixture was quenched by addition of 200 µL of DMF and 10 mL of water and passed through a preconditioned (10 mL EtOH followed by 10 mL water) Sep-Pak C18 Plus Cartridge. The labeled compound [^{18}F]**10b** was eluted with 1.0 mL of acetonitrile into a 5.0 mL conical vial. The volume was reduced to ~ 200 µL under reduced pressure at 70°Cand dilute with 800 µL of HPLC eluent and purified by preparative HPLC on a Chromolith® HPLC RP-18a performance colomn (100X4.6 mm) using an isocratic eluent (85% H_2O+0.1% TFA/ 15% MeCN +0.1%) at 4.0 mL/min (t_r = 3.65 min). [^{18}F]**10b** was obtained in radiochemical purities of >99% with a specific activity of 1.3 – 5.7 Ci/ µmol. When used for PET animal studies, the collected [^{18}F]**10b** was passed through a preconditioned (10 mL EtOH followed by 10 mL water) Sep-Pak C18 Light Cartridge and eluted with 1.0 mL EtOH and diluted with sterile saline prior to injection.

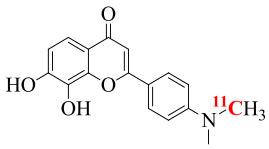

2-(4-[^{11}C](dimethylamino)phenyl)-7,8-dihydroxy-4H-chromen-4-one ([^{11}C]10c). Procedure for the labeling 13. Precursor **13** (1.0 mg) was placed in a 1.0 mL conical vial and dissolved in butanone (300µL). [^{11}C]MeOTf was transported by a stream of argon into the reaction vial for 5 minutes and the reaction mixture directly purified by preparative HPLC on a Chromolith® HPLC RP-18a performance colomn (100X4.6 mm) using a H_2O+0.1% TFA (A)/MeCN +0.1% TFA (B) gradient (t = 0 min: 100% A to t = 10 min A = 0%) at 4.0 mL/min (t_r = 3.5 min). [^{11}C]**10c** was obtained in radiochemical purities of >99% with a specific activity of of 0.7-1.0 Ci/µmol. When used for PET animal studies, the collected [^{11}C]**10c** was passed through a preconditioned (10 mL EtOH followed by 10 mL water) Sep-Pak C18 Light Cartridge and eluted with 1.0 mL EtOH and diluted with sterile saline prior to injection.

Quality Control of [^{18}F]10b and [^{11}C]10c. The determination of specific activity was achieved by comparison of the 254 nm UV absorbance peak (integration) of the carrier

products with standard calibration curves of the corresponding non-radioactive standards. Radiochemical purity was determined by HPLC injection of samples from the final ethanolic solutions.

Cell culture.

Primary CGNs. Rat Cerebellar granule neurons were prepared from post-natal day 7-8 rat brain, dissociated with trypsin and mechanical trituration, and cultured on poly-L-lysine-coated substrates for 24 h in Sato medium (Dulbecco's modified Eagle's medium with 10% fetal bovine serum, 1% penicillin/streptomycin, 1% N2 supplement, 100 ng/ml L-thyroxine and 80 ng/ml tri-iodothyronine) prior to treatment with BDNF. All cell culture reagents were obtained from Hyclone (Logan, UT).

Western Blot.

Treatments and Reagents. Cells were incubated in serum-free DME supplemented with 0.1% bovine serum albumin (BSA) (DMEB) and 2 mM L-glutamine for 1 h prior to treatment. Pre-incubation of different compound were done 30 min before. The concentration used was 25ng/ml for BDNF (Alomone); 50 μM, 250 μM and 500 μM for **8b**, **8c**, **10b**, **10c**, **1a** and **15** diluted in DMSO. Control was performed by treatment with 2% DMSO. Cells were stimulated for 10 min, 20 min, 30 min, 60 min and 120 min regarding the different compounds. Final concentrations of inhibitor treatments were 200 nM for K252A (VWR) pre-incubated 30 min prior to the treatments.

Immunoblotting. Samples were lysed directly in Laemmli sample buffer analyzed by SDS-PAGE. For immunoblotting, samples were separated by SDS-PAGE, transferred onto nitrocellulose membrane, which were then blocked in Tris-buffered saline/Tween (10 mmol/liter Tris (pH 8.0), 150 mmol/liter NaCl, 0.2% Tween 20) containing 5% (w/v) dried skim milk powder or 2% bovine serum albumin for phospho-specific antibodies. Membranes were then immunoblotted in blocking solution using anti-phospho-Trk (Tyr490) (New England Biolabs), anti-TrkB (Millipore), anti-phospho-Erk

(Thr-202/Tyr-204), anti-Erk (3A7) (New England Biolabs). Secondary antibodies were obtained from Jackson Laboratories (West Grove, PA), and incubations with them were performed in blocking solution. Immunoreactive bands were detected using the enhanced chemiluminescence solution kit (Perkin-Elmer Life Sciences, Norwalk, CT).

Computation and Measured Lipophilicity.

cLogP and cLogD (at pH = 7.4) values for 9 were computed with the program Pallas 3.0 for Windows (CompuDrug; San Francisco, CA). Experimental logD of [^{18}F]**10b** and [^{11}C]**10c** were measured by mixing ~25 μL of each radioligand formulation with 1.0 g each of 1-octanol and freshly prepared PBS buffer (pH = 7.4) in a culture tube. The culture tube was vortexed for 5 min followed by centrifugation for another 5 min. Radioactivity per 100 μL for the 1-octanol phase and the aqueous layer was measured using a well counter. The partition coefficient was determined as the ratio of counts per gram of 1-octanol to that of PBS buffer. All measurements were performed in triplicate. For plasma protein binding assessment, ~25 μL of the formulation of the tracers were incubated in rat plasma (500μL) at 37°C for 15 min, mixed with acetonitrile (50 μL) and separated by centrifugation for another 5 min. Ratios of activities were then measured.

In vitro Plasma Stabilities.

Compound [^{18}F]**10b** and [^{11}C]**10c** (radiochemical purity > 99%) were incubated in rat plasma (500μL) at 37°C and the amount of intact tracer was determined by HPLC analysis at different time points. All measurements were performed in triplicate. See Radiochemistry section for HPLC conditions.

Animal Experiments.

The MicroPET imaging protocol was approved by the Animal Care Committee of McGill University (Montreal, Canada).

In Vitro Autoradiography.

A rat was decapitated, the brain rapidly removed, frozen in 2-methylbutane (−40°C), and stored at −80°C. Brain sections (20 μm thick) were thaw mounted onto Superfrost Plus slides and stored at −80°C. After a preincubation in PBS buffer (30 mmol/L; pH 7.4 containing 137 mmol/L NaCl, 27 mmol/L) for 10 minutes at room temperature, rat sections were incubated (65 minutes; room temperature) in buffer containing [^{18}F]**10b**. Compound **1a** (10μM) and BDNF (10 nM, 1.0 nM and 0.1 nM) were used to determine the specific binding of [^{18}F]**10b** for TrkB. After three washes in incubation buffer (5 minutes, 4°C) and a rapid rinse in ice-cold water (15 seconds), the sections were dried with a stream of air (room temperature). Sections were then dried further in a vacuum container with formaldehyde powder for mild fixation. Specific binding was calculated as the difference of total and nonspecific binding. Labeled sections were placed on phosphor-imaging plates (BAS 2025; Fuji, Japan), with industrial tritium activity standards (Amersham Biosciences, Piscataway, NJ, USA). On exposure, the plates were scanned with a plate reader (spatial resolution of 50 μm; BAS 5000; Fuji).

PET and Biodistribution Study in Rat

PET imaging studies were performed in 7 sprague dawley type rats during 2% isoflurane anaesthesia. Between 230 and 876 uCi [^{11}C]**10c** or [^{18}F]**10b** were injected into a tail vein at scan start. Dynamic scans with 27 frames (8x30s, 6x60s, 5x120s, 8x300s) were acquired on a MicroPET RODENT R4 Concorde microsystem over 60 minutes. A 10 minute transmission scan was performed prior to the emission scans. After correction for attenuation, scatter and random coincidences PET images were reconstructed in a 128x128x62 matrix with a voxel size of 0.6mm x 0.6mm x 1.2 mm using a filtered back projection algorithm with a Hanning filter. Animal experiments were approved by the McGill Animal Care Committee (07106).

For analysis, decay corrected brain PET images of radioactivity concentrations [Bq/cc] were coregistered to a standard brain MRI using VINCI 4.07 (Max-Planck-Institute for neurological research, Cologne, http://www.nf.mpg.de/vinci3/). Whole brain time-

activity curves (TAC) were derived from a standard whole brain mask comprising gray and white matter. Time-activity curves for whole body scans were derived directly from the PET images by placing 3D ellipsoid VOIs into aorta (frame 1), liver (frame 3) and kidney (frame 4) on those frames where each organ showed the best contrast. Regional radioactivity concentrations [Bq/cc] were converted to standard uptake values relative to bodyweight (SUV_{BW}).

Associated Content.

Supporting information available. Supplementary biological evaluation figures, selected RadioHPLC chromatograms from the radiosynthesis of [^{18}F]**10b** and [^{11}C]**10c** and crystallographic data for **8b**, **8c**, **9c** and **15**. This material is available free of charge via the Internet at http://pubs.acs.org.

Author Information.

* To whom the correspondence should be addressed. Prof. R. Schirrmacher.

Acknowledgement.

This work was financially supported by Canada Foundation for Innovation (CFI) project no. 203639 to R.S.

We are grateful to Dean Jolly and Miriam M. Kovacevic for radioisotope production and assistance for radiochemistry, Antonio Aliaga for small animal PET imaging and Arturo Aliaga for autoradiography experiments.

3.7 References

1. Chao, M. V. Neurotrophins and their receptors: a convergence point for many signaling pathways. *Nat. Rev. Neurosci.* **2003**, *4(4)*, 299-309.
2. Huang, E. J.; Reichardt, L. F. Neurotrophins: roles in neuronal development and function. *Annu. Rev. Neurosci.* **2001**, *24*, 677-736.
3. Huang, E. J.; Reichardt, L. F. Trk receptors: roles in neuronal signal transduction. *Annu. Rev. Neurosci.* **2003**, *72*, 609-642.
4. (a) Pattarawarapan, M.; Burgess, K. Molecular basis of neurotrophin-receptor interaction. *J. Med. Chem*. **2003**, *46*, 5277-5291. (b) Hempstead, B. L.; Martin-Zanca, D.; Kaplan, D. R.; Parada, L. F.; Chao, M.V. High-affinity NGF binding requires coexpression of the Trk proto-oncogene and the low affinity NGF receptor. *Nature*, **1991**, *350*, 678-683.
5. Ichim, G.; Tauszig-Delamasure, S.; Mehlen P. Neurotrophins and cell death. *Exp. Cell. Res*. **2012**, *318*, 1221-1228.
6. Arévalo, J. C.; Wu, S. H. Neurotrophin signaling: many exciting surprises! *Cell. Mol. Life Sci.* **2006**, *63*, 1523-1537.
7. Nagappan, G.; Woo, N. H.; Lu, B. Ama ‘’zinc’’ link between TrkB transactivation and synaptic plasticity. *Neuron* **2008**, *57*, 477-479.
8. Lee, F. S.; Rajagopal, R. Chao, M. V. Distinctive features of Trk neurotrophin receptor transactivation by G protein-coupled receptor. *Cytokine Growth F. R.* **2002**, *13*, 11-17.
9. Teng, K. K.; Hempstead, B. L. Neutrophins and their receptors: signaling trios in complex biological systems. *Cell. Mol. Life Sci.* **2004**, *61*, 35-48.
10. Haapasalo, A.; Koponen, E.; Hoppe, E.; Wong, G.; Castren, E. Truncated trkB.T1 Is Dominant Negative Inhibitor of trkB.TK+-Mediated Cell Survival. *Biochem. Biophys. Res. Comm.* **2001**, *280*, 1352-1358.
11. Vesa, J.; Kruttgen, A.; Shooter, E.M. p75 Reduces TrkB tyrosine Autophosphorylation in response to brain-derived neurotrophic factor and neurtrophin 4/5. *J. Biol. Chem.* **2000**, *275*, 24414-24420.
12. Muragaki, Y.; Timothy, N.; Leight, S.; Hempstead, B. L.; Chao, M. V., Trojanowsaki, J. Q.; Lee, V. M. Expression of trk receptor in the developing and

adult human central and peripheral nervous system. *J. Comp. Neurol*. **1995**, *356*, 387-397.

13. Murer, M. G.; Yan, Q.; Raisman-Vozari, R. Brain-derived neurotrophic factor in the control human brain, and in Alzheimer's disease and Parkinson's disease. *Prog. Neurobiol*. **2001**, *63*, 71–124.
14. Schindowski, K.; Belarbi, K.; Buee, L. Neutrophic factors in Alzheimer's disease: role of axonal transport. *Genes Brain Behav.* **2008**, *7 (suppl 1)*, 43-56.
15. (a) Deng, V.; Matagne, V.; Banine, F.; Frerking, M.; Ohliger, P.; Budden, S.; Pevsner, J.; Dissen, G. A.; Sherman, L. S.; Ojeda, S. R. FXYD1 is an MeCP2 target gene overexpressed in the brains of Rett syndrome patients and *Mecp2*-null mice. *Hum. Mol. Genet*. **2007**, *16*, 640-650. (b) Ogier, M.; Wang, H.; Hong, E.; Wang, Q.; Greenberg, M. E.; Katz, D. M. Brain-derived neurotrophic factor expression and respiratory function improve after ampakine treatment in a mouse model of Rett syndrome. *J. Neurosci*. **2007**, *27(40)*, 10912-10917.
16. Fumagalli, F.; Racagni, G.; Riva, M. A. Shedding light into the role of BDNF in the pharmacotherapy of Parkinson's disease. *Pharmacogenomics* **2006**, *6(2)*, 95-104.
17. Zuccato, C.; Cuttaneo, E. Role of brain-derived neurotrophic factor in Huntington's disease. *Prog. Neurobiol*. **2007**, *81(5-6)*, 294-330.
18. Pillai, A. Brain-derived neurotrophic factor/TrkB signaling in the pathogenesis and novel pharmacotherapy of schizophrenia, *Neurosignals*. **2008**, *16*, 183-193.
19. Griesbach, G. S.; Hovda, D. A.; Gomez-Pinilla, F. Exercise-induced improvement in cognitive performance after traumatic brain injury in rats is dependent on BDNF activation. *Brain Res.* **2009**, *1288*, 105-115.
20. Li, Y.; Luikart, B. W.; Birnbaum, S.; Chen, J. ;l Kwon, C. H.; Kernie, S.; G.; Bassel-Duby, R.; Parada, L. F. TrkB regulates hippocampal neurogenesis and governs sensitivity to antidepressive treatment. *Neuron* **2008**, *59*, 399-412.
21. Brodeur, G. M.; Minturn, J. E.; Ho, R.; Simpson, A. M.; Iyer, R.; Varela, C. R.; Light, J. E.; Kolla, V.; Evans, A. E. Trk receptor expression and inhibition in neuroblastomas. *Clin Cancer Res* **2009**, *15*, 3244-3250.

22. Sclabas, G. M.; Fujioka, S.; Schmidt, C.; Li, Z.; Frederick, W. A.; Yang, W.; Yokoi, K.; Evans, D. B.; Abbruzzese, J. L.; Hess, K. R.; Zhang, W.; Fidler, I. J.; Chiao, P.J. Overexpression of tropomysin-related kinase B in metastatic human pancreatic cancer cells. *Clin. Cancer Res*. **2005**, *11*, 440–9.
23. Okamura, K.; Harada, T.; Wang, S.; Ijichi, K.; Furuyama, K.; Koga, T.; Okamoto, T.; Takayama, K.; Yano, T.; Nakanishi, Y. Expression or TrkB and BDNF is associated with poor prognostic in non-small cell lung cancer. *Lung Cancer*, **2012**, *78*, 100-106.
24. Douma, S.; Van, Laar, T.; Zevenhoven, J.; Meuwissen, R.; Van Garderen, E.; Peeper, D. S. Suppression of anoikis and induction of metastasis by the neurotrophic receptor TrkB. *Nature* **2004**, *430*, 1034-1039.
25. (a) Price, R. D.; Milne, S. A.; Sharkey, J.; Matsuoka, N. Advances in small molecules promoting neurotrophic function. *Pharmacology and Therapeutics* **2007**, *115*, 292-306. (b) Weissmiller, A. M.; Wu, C. Current advances in using neurotrophic factors to treat neurodegenerative disorders. *Translational Neurodegeneration* **2012**, *1*, 14.
26. Zhang, Y.; Chi, X. X.; Nicol, G. D. BDNF enhances the excitability of rat sensory neurons through activation of the p75 neurotrophin receptor and the spingomyelin pathway. *J. Physiol.* **2008***, 586(13)*, 3113-3127.
27. Jang, S.-W.; Liu, X.; Yepes, M.; Shepherd, K. R.; Miller, G. W.; Liu, Y.; Wilson, W. D.; Xiao, G.; Blanchi, B.; Sun, Y.; Ye, K. A selective TrkB agonist with potent neurotrophic activities by 7,8-dihydroxyflavone. *Proc. Natl. Acad. Sci. U.S.A*. **2010**, *107*, 2687-2692.
28. Liu, X.; Chan, C.-B.; Jang, S.-W.; Pradoldej, S.; Huang, J.; He, K.; Phun, L. H.; France, S.; Xiao, G.; Jia, Y.; Luo, H. R.; Ye, K. A synthetic 7,8-dihydroxyflavone derivative promotes neurogenesis and exhibits potent antidepressant effect. *J. Med. Chem*. **2010**, *53*, 8274-8286.
29. Liu, X.; Chan, C.-B.; Qi, Q.; Xiao, G.; Luo, H. R.; He, X.; Ye, K. Optimization of a small tropomyosin-related kinase B (TrkB) agonist 7,8-dihydroxyflavone active in mouse models of depression. *J. Med. Chem*. **2012**, *55*, 8524-8537.

30. Cazorla, M.; Prémont, J.; Mann, A.; Girard, N.; Kellendonk, C.; Rognan, D. Identification of a low-molecular weight TrkB antagonist with anxiolytic and antidepressant activity in mice. *J.Clin. Invest*. **2011**, *121*, 1846-1857.
31. Massa, S. M.; Yang, T.; Xie, Y.; Shi, J.; Bilgen,M.; Joyce, J. N.; Nehama, D.; Rajadas, J.; Longo, F. M. Small molecule BDNF mimetics activate TrkB signaling and prevent neuronal degeneration in rodents. *J.Clin. Invest*. **2010**, *120*, 1774-1785.
32. Ververidis, F.; Trantas, E.; Douglas, C.; Vollmer, G.; Kretzschmar, G.; Panopoulos, N. Biotechnology of flavonoid and other phenylpropanoid-derived natural products. Part 1: Chemical diversity, impacts on plant biology and human health, *Biotechnol. J.* **2007**, *2*, 1214-1234.
33. Andero, R.; Daviu, N.; Escorihuela, R. M.; Nadal, M.; Armario, A. 7,8-Dihydroxyflavone, a TrkB receptor agonist, blocks long-term spatial memory impairment caused by immobilization stress in rat. *Hippocampus*, **2010**, *23*, 399-408.
34. Andero, R.; Heldt, S. A. Ye, K.; Liu, X.; Armario, A.; Ressler, K. J. Effect of 7,8-dihydroxyflavone, a small-molecule TrkB agonist, on emotional learning. *Am. J. Psychiatry*, **2011**, *168*, 163-172.
35. Devi, L.; Ohno, M. 7,8-Dihydroxyflavone, a small-molecule TrkB agonist, reverse memory deficits and BACE1 elevation in a mouse model of Alzheimer's disease. *Neuropsychopharmacology*, **2012**, *37*, 434-444.
36. Jonhson, R. A.; Lam, M.; Punzo, A. M.; Li, H.; Lin, B. R.; Ye, K.; Mitchell, G. S.; Chang, Q. 7,8-Dihydroxyflavone exhibits therapeutic efficacy in a mouse model of Rett syndrome. *J. Appl. Physiol.* **2012**, *112*, 704-710.
37. Zeng, Y.; Lv, F.; Li, L.; Yu, H.; Dong, M.; Fu, Q. 7,8-Dihydroxyflavone rescues spatial memory and synaptic plasticity in cognitively impaired aged rats. *J. Neurochem*. **2012**, *122*, 800-811.
38. Maiti, A.; Cuendet, M.; Kondratyuk, T.; Croy, V. L.; Pezzuto, J. M.; Cushman, M. Synthesis and cancer chemopreventive activity of zapotin, a natural product from casimiroa edulis. *J. Med. Chem*. **2007**, *50*, 350-355.

39. Menichincheri, M.; Ballinari, D.; Bargiotto, A. Bonomoni, L.; Ceccarelli, W.; D'Alession, R.; Fretta, A.; Moll, J.; Polucci, P.; Soncini, C.; Tibolla, M.; Trosset, J.-Y.; Vanotti, E. Catecholic flavonoids acting as telomerase inhibitors. *J. Med. Chem*. **2004**, *47*, 6466-6475.
40. Chiruta, C.; Schubert, D.; Dargusch, R.; Maher, P. *J. Med. Chem*. **2012**, *55*, 378-389.
41. Peng, Y.; Liu, H.; Tang, M.; Cai, L.; Pike, V. Highly efficient *N*-monomethylation of primary aryl amines. *Chinese J. Chem*. **2009**, *27*, 1339-1344.
42. Zhang, W.; Oya, S.; Kung, M.-P.; Hou, C.; Maier, D. L.; Kung, H. F. F-18 Stilbenes as PET imaging agents for detecting β-amyloid plaques in the brain. *J. Med. Chem*. **2005**, *48*, 5980-5988.
43. Haka, M. S.; Kilbourn, M. R.; Watkins, L.; Toorongian, S. A. Aryltrimethylammonium trifluoromethanesulfonates as precusors to aryl [^{18}F]fluoride: improved synthesis of [^{18}F]GBR-13119. *J. Lab. Comp. Radiopharm.* **1988**, *27*, 823-833.
44. Gupta, V.K.; You, Y.; Li, J. C.; Klistorner, A.; Graham, S. L. Protective effect of 7,8-dihydroxiflavone on retinal ganglion and RGC-5 cells against excitotoxic and oxidative stress. *J. Mol. Neurosci.* **2013**, *49*, 96-104.
45. Tsai, T.; Klausmeyer, A.; Conrad, R.; Gottschling, C.; Leo, M.; Faissner, A.; Wiese, S. 7,8-Dihydroxyflavone leads to survival of cultured embryonic motoneurons by activating intracellular signaling pathways. *Mol. Cell. Neurosci.* **2013**, http://dx.doi.org/10.1016/j.mcn.2013.02.007.
46. Park, H.Y.; Kim, G.Y.; Hyun, J.W.; Hwang, H.J.; Kim, B. W.; Choi, Y.H.; 7,8-Dihydroxyflavone exhibits anti-inflammatory properties by downregulating the NF-kappaB and MAPK signaling pathways in lipopolysaccharide-treated RAW264.7 cells. *Int. J. Mol. Med.* **2012**, *29*, 1146-1152.
47. Minichiello, L.; Klein, R. TrkB and TrkC neurotrophin receptor cooperate in promoting survival of hippocampal and cerebellar granule neurons. *Genes Dev*. **1996**, *10*, 2849-2858.

48. Courtney, M. J.; Akerman, K. E. O.; Coffey, E. T. Neurotrophins protect cultured cerebellar granule neurons against the early phase of cell death by a two-component mechanism. *The Journal of Neuroscience* **1997**, 11, 4201-4211.
49. Zirrgiebel, U.; Ohga, Y.; Berninger, B.; Inagaki, N.; Thoenen, H.; Lindholm, H. Characterization of TrkB receptor-mediated signaling parthways in rat cerebellar granule neurons: involvement of protein kinase C in neuronal survival. *J. Neurochem*. **1995,** *65*, 2241-2250.
50. Michaelsen, K.; Zagrebelsky, M.; Berndt-Huch, J.; Polack, M.; Buschler, A.; Sendtner, M.; Korte, M. Neurotrophin receptors TrkB.T1 and p75NTR cooperate in modulating both functional and structural plasticity in the mature hippocampal neurons. *Eur. J. Neurosci.* **2010**, *32*, 1854-1865.
51. Zaccaro, M. C.; Ivanisevic, L.; Perez, P.; Meakin, S. O.; Saragovi, H. U. p75 Co-receptors regulate ligand-dependant and ligand-independant Trk receptor activation, in part by altering Trk docking subdomains. *J. Biol. Chem*. **2001**, *276*, 31023-31029.
52. (a) Ono, M.; Yoshida, N.; Ishibashi, K.; Haratake, M.; Arano, Y.; Mori, H.; Nakayama, M. Radioiodinated flavones for in vivo imaging of β-amyloid plaques in the brain. *J. Med. Chem.* **2005**, *48*, 7253–7260. (b) Ono, M.; Watanabe, R.; Kawashima, H.; Kawai, T.; Watanabe, H.; Haratake, M.; Saji, H.; Nakayama, M. 18F-Labeled flavones for in vivo imaging of β-amyloid plaques in Alzheimer's brains. *Bioorg. Med. Chem*. **2009**, *17*, 2069–2076. (c) Ono, M.; Haratake, M.; Mori, H.; Nakayama, M. Novel chalcones as probes for in vivo imaging of β-amyloid plaques in Alzheimer's brains. *Bioorg. Med. Chem*. **2007**, *15*, 6802–6809. (d) Ono, M.; Watanabe, R.; Kawashima, H.; Cheng, Y.; Kimura, H.; Watanabe, H.; Haratake, M.; Saji, H.; Nakayama, M. Fluoro-pegylated chalcones as positron emission tomography probes for in vivo imaging of β-amyloid plaques in Alzheimer's disease. *J. Med. Chem.* **2009**, *52*, 6394–6401. (e) Ono, M.; Maya, Y.; Haratake, M.; Ito, K.; Mori, H.; Nakayama, M. Aurones serve as probes of β-amyloid plaques in Alzheimer's disease. *Biochem. Biophys. Res. Commun.* **2007**, *361*, 116–121. (f) Maya, Y.; Ono, M.; Watanabe, H.; Haratake, M.; Saji, H.; Nakayama, M. Novel radioiodinated aurones as probes

for SPECT imaging of β-amyloid plaques in the brain. *Bioconjugate Chem*. **2009**, *20*, 95–101. (g) Ryu, E. K.; Choe, Y. S.; Lee, K. H.; Choi, Y.; Kim, B. T. Curcumin and dehydrozingerone derivatives: Synthesis, radiolabeling, and evaluation for β-amyloid plaque imaging. *J. Med. Chem*. **2006**, *49*, 6111–6119.

53. Walle, T. Methylation of dietary flavones increases their metabolic stability and chemopreventive effect. *Int. J. Mol. Sci.* **2009**, *10*, 5002-5019.
54. Masana, Y.; Wanaka, A.; Kato, H.; Asai, T.; Tohyama, M. Localization of TrkB mRNA in postnatal brain development. *J. Neurosci*. *Res*. **1993**, *35*, 468-479.
55. Shia, C,-S.; Tsai, S.-Y.; Kuo, Y.-C.; Chao, P.-D. L. Metabolism and Pharmacokinetics of 3,3′,4′,7-Tetrahydroxyflavone (Fisetin), 5-Hydroxyflavone, and 7-Hydroxyflavone and Antihemolysis Effects of Fisetin and Its Serum Metabolites. *J. Agric. Food Chem*. **2009**, *57*, 83-89.
56. Jager, A. K.; Saaby, L. Flavonoids and the CNS. *Molecules*, **2011**, *16*, 1471-1485.
57. Morris, M. E. and Zhang, S. Flavonoid–drug interactions: Effects of flavonoids on ABC transporters. *Life Sci*. **2006**, *78*, 2116-2130.
58. Alvarez, A. I.; Real, R.; Perez, M.; Mendoza, G.; Prieto, J. G.; Merino, G. Modulation of the Activity of ABC Transporters (P-Glycoprotein, MRP2, BCRP) by Flavonoids and Drug Response. *J. Pharma. Sci*. **2010**, *99*, 598-617.
59. Boumendjel, A.; DiPietro, A..; Dumontet, C.; Barron, D. Recent Advances in the Discovery of Flavonoids and Analogs with High-Affnity Binding to P-Glycoprotein Responsible for Cancer Cell Multidrug Resistance. *Med. Res. Rev*. **2002**, *22*, 512-529.

3.8 Contribution des co-auteurs pour l'article

J'ai réalisé la conception et la gestion du projet de recherche sous la supervision de mon directeur, le Prof. Ralf Schirrmacher. J'ai aussi effectué les réactions non-radioactives, dont certaines avec Mehdi Boudjemeline, alors stagiaire d'été sous ma supervision au sein de notre groupe de recherche. L'ensemble des expériences de radiochimie de même que les charactérisations physico-chimiques des radiotraceurs a été effecué par moi-même. Les expériences d'autoradiographie *in vitro* ont été menées par Arturo Aliaga (groupe de recherché du Prof. Pedro Rosa-Neto) et moi-même. Les expériences de caractérisation biologique (Western blot) ont été effectuées par Dr. Perrine Gaud (groupe de recherché du Prof. Philip A. Barker).

J'ai réalisé l'ensemble de l'analyse des données: chimie, radiochimie, évaluation biologique de même que l'évaluation des traceurs à l'exception de la section concernant l'analyse des données de TEP et la biodistribution réalisée de pair avec Dr. Alexander Thiel. Les analyses (calcul des SUV) des données de TEP et de la biodistribution proprement dite ont été réalisées par Dr. Alexander Thiel. J'ai aussi rédigé la totalité du manuscript. Le manuscript à été corrigé par le Prof. Ralf Schirrmacher et revu et approuvé par les co-auteurs. Le Dr. Esther Schirrmacher et Joshua Chin ont tous les deux apporté une aide précieuse quand à la finalisation du manuscript vis-à-vis des corrections associées à la langue.

Chapter 4

Derivatization of flavone-based TrkB radioligands for PET imaging; Structural investigation and optimization

4.1 Introduction

PET imaging analysis of our first-generation TrkB probes demonstrate poor *in vivo* properties as imaging agents despite a promising *in vitro* profile (Figure 4.1). Indeed, many polyhydroxylated flavonoids showing promising biological activities suffer from limited *in vivo* applicability due to poor metabolic stability, bioavailability, and/or absorption.[1] This is usually a consequence of the extensive conjugation of free hydroxyl functionalities, which are also essential to the binding of their molecular target.[2]

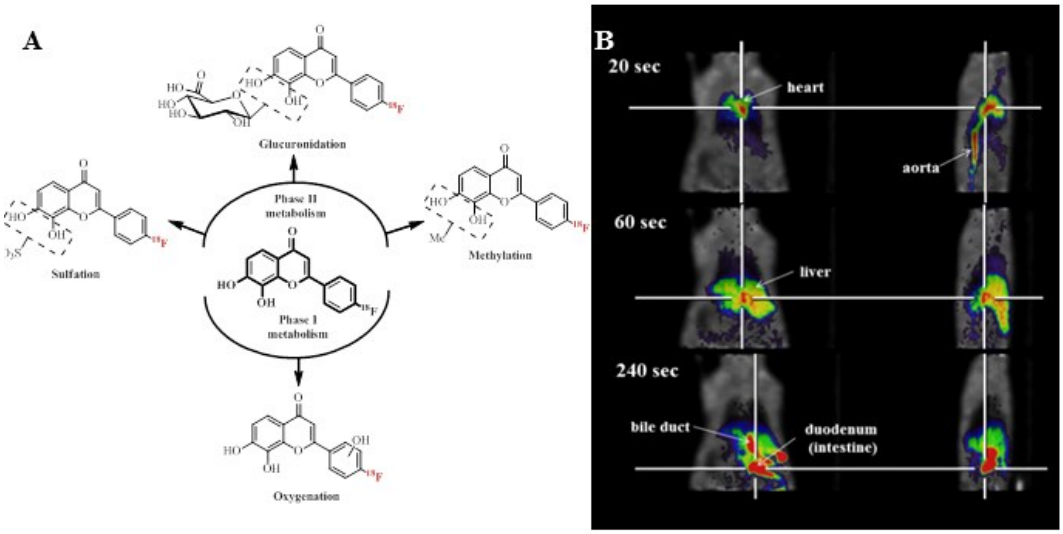

Figure 4.1. Radiolabeled 7,8-dihydroxyflavones metabolism **(**A) Possible metabolism of catechol-bearing compound; example of 2-(4-[^{18}F]fluorophenyl)-7,8-dihydroxy-4*H*-chromen-4-one. (A) Methylation, sulfation, glucuronidation and oxygenation. (B) PET images illustrating the fast hepatobiliary clearance of the radiotracer.

For the development of a PET radioligand, metabolic criteria are even more restrictive. Indeed, poorly stable but non-toxic therapeutics, or therapeutics acting as efflux transporter substrates, may still act upon their intended targets and exert their biological effects *in vivo* at high doses, either as the intact molecule or in the form of its metabolites. However, the use of radiotracers in trace quantities, an intrinsic aspect of PET imaging, implies that enzymatic degradation or transporter protein interactions are parameters that cannot be overcome by scaling up tracer amounts administered.

Moreover, numerous flavonoids, including flavones, are P-glycoprotein inhibitors, which may significantly limit their ability to bind a CNS target, especially at trace levels.[3] Yet, PET imaging agents displaying sufficient *in vivo* stability but are susceptible to P-glycoprotein at the BBB may readily enter the brain following pre-saturation of P-glycoprotein with an additional substrate or inhibitor.[4]

With regards to bioactivity, our results show that the introduction of a strong electron-donating substituent on the flavonoid 4'-position, such as a dimethylamino group at the B ring, enhances the potency of BDNF-induced TrkB phosphorylation and downstream signaling inhibition in CGNs at micomolar concentrations. These observations are in agreement with previous studies whereby either a 4'-dimethylamino, a 4'-pyrrolidino, or a 4'-morpholino moiety enhances agonistic activity of 7,8-dihydroxyflavone derivatives towards p-TrkB and the downstream signaling cascade in embryonic hippocampal or cortical primary cell assays in nanomolar concentrations.[5]

Taken together, these observations suggest that structure-activity relationship (SAR) studies and investigation of bioisoteric modifications are necessary in order to resolve enzymatic instability and to better understand the structural requirements necessary for activity of the 7,8-dihydroxyflavone analogues.

4.2 Structure-activity relationship

In terms of SAR and bioisosteric modifications, the challenges encountered in the development of a PET tracer are similar to ones associated with the medicinal chemistry optimization of leads for drug discovery. However, an additional requirement is necessary when radiolabeled imaging probes are considered, namely that functional mimicry with a suitable bioisostere has to be compatible with radiolabeling conditions. For example, the bioisosteric modification suggested by Liu and colleagues for the conversion of the 4'-dimethylamino to the 4'-pyrrolidino fragment, such as in compound **1.61**, may be favourable in a therapeutic perspective but would not be compatible with the envisioned radiolabeling at the 4'-position.[5] Consequently, structure optimization and labeling position planning must be envisioned together.

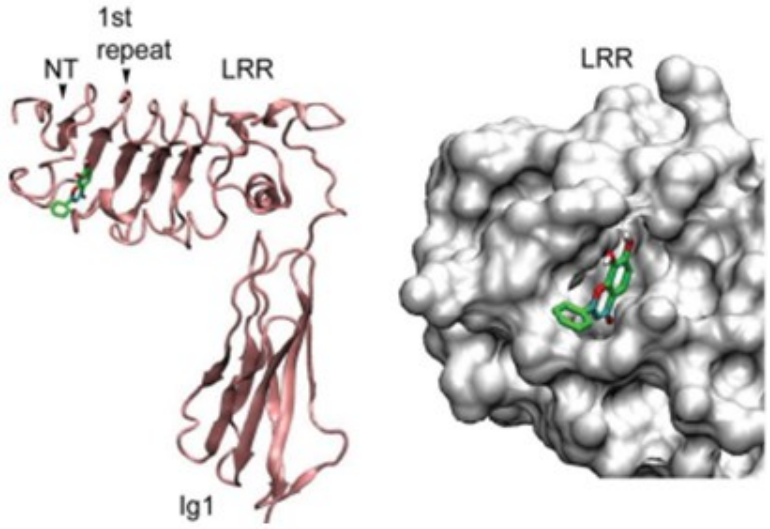

Figure 4.2. Homology model of the TrkB extracellular domain (ECD) and the docking of 7,8-dihydroxyflavone to TrkB ECD in leucine-rich repeat (from Ref. 5)

Liu and colleagues have also suggested a molecular modeling for the docking of 7,8-dihydroxyflavone to TrkB obtained via comparative modeling from the homologous TrkA structure.[5] This model is, at best, approximative as it has been derived from an homology model of the TrkB receptor. Nevertheless, it supports our observations that various unrelated structural modifications at the 4'-position may be tolerated since this site is solvent-exposed and distal to the binding pocket of TrkB. It also suggests that the north part of the ligand, from the carbonyl group of the benzopyran ring and the 5- and 6-positions at the A-ring, must be kept intact. Moreover, suitable bioisosteric modification of the 7- and 8-positions may be tolerated as they are positioned at the mouth of the pocket.

4.2.1 The *B*-ring

4.2.1.1 Conformational analysis and biological activity

Firstly, we were interested in investigating the parameters behind the marked differences in the potencies, either agonistic or antagonistic, of 4'-substituated dihydroxyflavone ligands (4'-NMe_2 >> 4'-F ≈ 4'-H). Due to the structural diversity tolerated at this position, and considering the docking model presented, we hypothesized that the ~8-fold increase in inhibitory activity of the dimethylamino-substituted lead compound could be a consequence of stereoelectronic effects rather than direct interaction with the binding site. More specifically, we intended to validate that the activation of the carbonyl group of the benzopyranone ring via electron delocalization, and concomitant influence on conformation, could explain the enhanced activity of this ligand compared to ligands bearing electron withdrawing or neutral substituents.

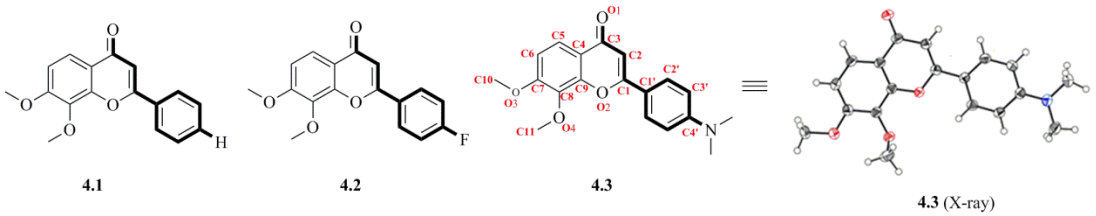

Figure 4.3. Structures of the series of 4'-subsituted 7,8-dimethoxyflavone and ORTEP view of the $C_{19}H_{19}NO_4$ compound (**4.3**). Ellipsoids drawn at 50% probability level. Hydrogen atoms are represented by sphere of arbitrary size.

To evaluate the above hypothesis, we compared the crystal structures of compounds **4.1**, **4.2** (*vide supra*), and **4.3** (Figure 4.3). Even if the highly hygroscopic 7,8-dihydroxyflavones could not be recrystallized, we could extrapolate the above 7,8-dimethoxyflavone compared to other 7,8-disubstituated ligands, such as the 7,8-dihydroxyl analogue, sharing the same benzylideneacetone moiety.

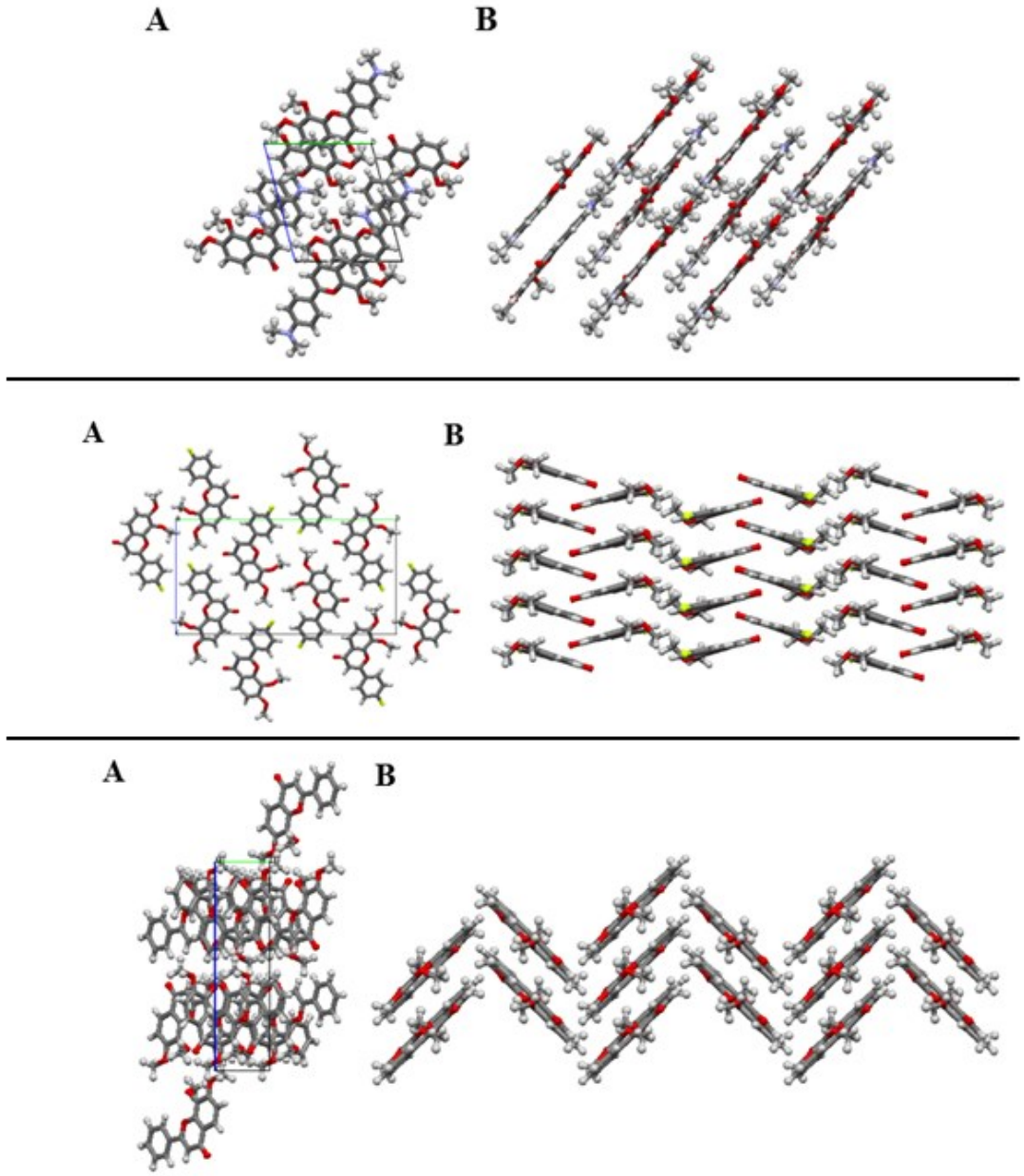

Figure 4.4. The crystal packing of compounds **4.3** (higher panel), **4.2** (central panel) and **4.1** (lower panel) viewed along (A) the *a*-axis. (B) All 3 compounds are nearly coplanar with respect to *B* and *AC* rings; representation of the π- π stacking.

In solution, the lowest-energy conformation of flavones result from the balance of the following opposing factors: (1) conjugation factors between rings *B* (phenyl) and *AC* (benzopyranone), and intramolecular hydrogen bonding favoring molecular planarity,

versus (2) steric repulsion of *ortho*-hydrogen atoms and substituents in the *B*-ring as demonstrated *in silico* and experimentally.[6] Flavones are typically observed in the *syn-gauche* conformation, as the calculated lowest-energy torsion angle in flavone and 7,8-dihydroxyflavone is approximately $\theta = 30°$.[6c,7] In the solid-state, however, the conformation of those highly aromatic molecules is often dominated by π- π stacking.[6,8] Data on solid-state conformation provided by the crystal structures of **4.1**, **4.2**, and **4.3** (Figure 4.4) may not translate well towards their behavior in solution or in a protein-bound state. Nevertheless, the analysis of the different bond lengths based on these results, especially in the benzylideneacetone system, may be highly informative.

Compound **4.3** exhibits an unusually short C(1')-C(1) bond length of 1.456 (2) Å, which is significantly different from that observed in compounds **4.2** (1.474 (2) Å) and **4.1** (1.473 (3) Å), and in the typical flavone. The C(1')-C(1) partial double-bond character, linking rings *B* and *C*, extensive electron delocalization, evidence of molecular planarity in the flavone. The effect of electron delocalization in compound **4.3** can be observed as far as the C(3)-O(1) bond, which is elongated (1.242 (1) Å) compared to **4.2** (1.237 (2) Å) and **4.1** (1.229 (2) Å). Those differences suggest that compound **4.3** has a different low energy-state (likely near-planar) in contrast to flavone **4.2** and **4.1** which may favour a pronounced torsion angle typical in solution-phase flavones. Since compound **4.3** presents distinct electronic properties, leading to preferential planar conformation *and* distinct favourable potency, as compared to compounds **4.1** and **4.2**, it follows that the binding site of TrkB for those ligands may preferentially accommodate planar 7,8-disubsituted flavones.

Further modification of the *B*-ring includes addition of substituents on the 2'- and 3'-positions. Whereas substitution at the 3'-position may be of interest in a future SAR study, introduction of substituents at the 2'-position will likely generate conformationally-distorted ligands or even atropisomers, which may be detrimental to TrkB binding.

4.2.1.2 Radiolabeled bioisosteres

In conclusion, the electron-donating character of the 4'-fragment is an important stereoelectronic requirement. Also, the structural flexibility allowed at this position suggests the use of this site for radiolabel incorporation. Ideally, given the above ideas, introduction of an ^{18}F-labeled electron-donating fragment is highly desirable. In consequence, we are currently synthesizing various fluoroazetidines and fluoropyrrolidines as fluorinated bioisosteres. The ^{18}F-labeled equivalents of these ligands will be obtained via nucleophilic (S_N2) radiofluorination from their respective tosylates.

4.2.2 The *A*-ring

4.2.2.1 Biological evaluation of methylated analogues

The next step involves modification of the catechol fragment. The methylated analogues **4.2** and **4.3** were investigated for BDNF-induced TrkB activation (Figure 4.5, A and B). Masking the catechol fragment of bioactive flavones via methylation was previously shown to significantly enhance metabolic stability and transport through biological membrane.[9] However, methylation of flavonoids was also shown to suppress biological activity.[10] For 7,8-dimethoxyflavone derivatives, Liu and colleagues[11] have demonstrated that methylation progressively reduces the agonistic activity in cortical neurons from the 7,8-dihydroxy (**1.59**), to the 7-methoxy (**4.4**), and finally, to the 7,8-dimethoxy (**4.3**) ligands at 500 nM compared to BDNF. Our results regarding inhibitory activity in CGN support those findings, showing that compound **4.3** and **4.2** do not significantly antagonise BDNF-induced TrkB activity under 500 μM. Nevertheless, inhibition was observed at higher concentration in CGN and compound **4.3** was also recently shown to be more potent than the initial lead compound **1.58** in cortical neurons.[12]

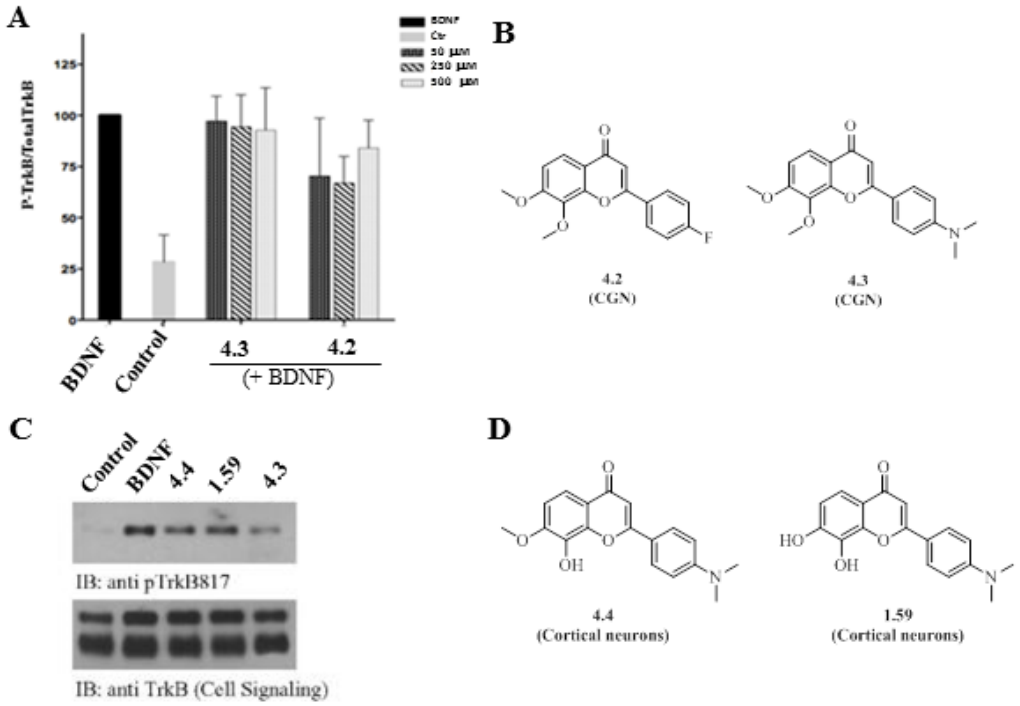

Figure 4.5. Biological evaluation of methylated derivatives. (A) Quantification of p-TrkB concentrations from a densitometry analysis of the western blots for 7,8-DMF (**4.2** and **4.3**) derivatives on BDNF-induced TrkB phosphorylation normalized to the maximum BDNF response at different antagonist concentrations. Primary cerebellar granule neurons were treated with BDNF (1.8 nM) and different antagonists concentrations (50 μM, 250 μM, 500 μM) for 30 min. Control corresponds to TrkB basal activity. Data are mean ± s.d. (n = 3) of ratio of p-TrkB/Total TrkB. (B) Structure of **4.2** and **4.3**. (C) Immunoblotting assays on primary cortical neurons of **4.3**, **4.4** and **1.59** at 500 nM (adapted from Ref. 11). (D) Structure of **4.4** and **1.59**.

Despite being associated with suboptimal affinity as PET imaging probes, we hypothesized that the radiochemical analogue of **4.3** could provide a tool for the assessment of BBB permeation and P-glycoprotein susceptibility of flavone-based TrkB ligands bearing a modified catechol fragment.

*4.2.2.2 Radiosynthesis of [N-methyl-^{11}C]**4.3***

Radiosynthesis of [*N*-methyl-^{11}C]**4.3** was optimal when reacting the *N*-normethyl precursor **4.5** with [^{11}C]MeOTf in the presence of aqueous NaOH (Table 4.1, entry 6). Methylation attempts with [^{11}C]MeI and base were inefficient even at high temperatures due to the deactivated nature of the *N*-methylaniline precursor.

Table 4.1. Optimization of the radiosynthesis of [*N*-methyl-^{11}C]4.3

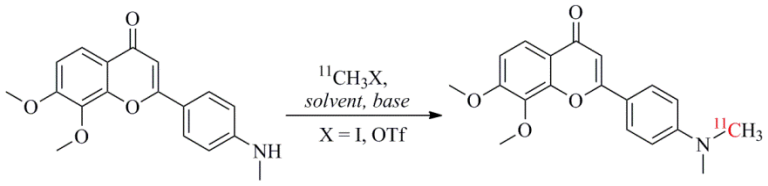

4.5 **[*N*-methyl-^{11}C]4.3**

Entry	Conditions[1]	RCY[2]
1	DMSO (300 µL), rt, $^{11}CH_3I$	*trace* [3]
2	DMSO (300 µL), NaOH (solid), 60°C, $^{11}CH_3I$	<5%
3	$(CH_3)_2CO$ (300 µL), 50°C, $^{11}CH_3I$	*trace* [3]
4	DMSO (300 µL), rt, $^{11}CH_3OTf$	5-10%
5	DMSO (300 µL), 3.0 µL NaOH (4.0M), rt, $^{11}CH_3OTf$	41%
6	DMSO (300 µL), 3.0 µL NaOH (4.0M), 50°C, $^{11}CH_3OTf$	35-45%
7	THF (300 µL), 100 µL DBU, 50°C, $^{11}CH_3OTf$	0% [4]

[1] 2.0 mg of **4.5**. [2] Radio-HPLC RCY, n.d.c. [3] No side product. [4] Major radiolabeld side product.

Likewise, methylation efforts with [^{11}C]MeOTf, in the absence of base or with mild bases in various solvents, were insufficient to deliver [*N*-methyl-^{11}C]**4.3**. Indeed, deactivated *N*-methylanilines represent challenging ^{11}C-methylation targets normally associated with low RCYs.[13] Interestingly, further optimization demonstrated very little temperature-dependence (Table 4.1, entry 5-6), but RCYs greatly fluctuated with starting quantities of base, as shown by the 70% RCY (n.d.c.) of [*N*-methyl-^{11}C]**4.3**

obtained after 2 minutes of reaction in DMSO with 6.0 μL of aqueous NaOH (4.0 M) at room temperature (Figure 4.6). This outcome was rather unexpected and it was initially suspected that the precursor **4.5** could have been isolated as its corresponding hydrochloric salt which, upon treatment with various amounts of NaOH, would have simply liberated the free base form. However, characterization of compound **4.5** unambiguously demonstrated that the precursor was present in its free base form, suggesting that the reaction proceeded differently via a more reactive species.

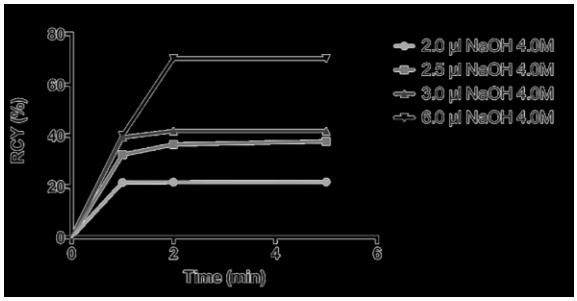

Figure 4.6. Optimization of the amount of base (NaOH) in the radiosynthesis of [*N*-methyl-^{11}C]**4.3**.

We then hypothesized that ^{11}C-methylation proceeded via an anilinide anion. Despite being implausible when considering non-radioactive, macroscopic chemistry, even trace quantities of the highly nucleophilic anilinide anion generated upon reaction with NaOH could represent an important excess over the ^{11}C-methylation agent present in picomolar, radiochemical scales. In fact, Cai and colleagues[14] already demonstrated that ^{11}C-*N*-methylation of deactivated arylamines proceeded through this type of intermediate in the presence of bases such as KOH.

Although an experimental pK_a value for precursor **4.5** was not determined, a qualitative approximation can be attempted by considering the ability of the conjugated system to stabilize an anionic intermediate. The pK_a of 4-nitroaniline (pK_a = 16.9) is substantially lower than unsubstituted aniline, which has a pK_a of 30.7 (DMSO).[14,15] Electron delocalization via the nitro-substituent is the major contributor in explaining this remarkable difference, i.e. the ability of the *para*-subsituent to stabilize the anilide anion (Figure 4.7). Nucleophilic aromatic radiofluorination yields also reflect the ability of the

precursor to stabilize the anionic intermediate generated, i.e. the Meisenheimer complex (Figure 4.7). Radiofluorination performed with the nitro-precursor **4.6** (*vide supra*) reflects the anion stabilization properties of the benzylideneacetone system – also encountered in precursor **4.5** – with >80% RCY at 150°C in DMF.

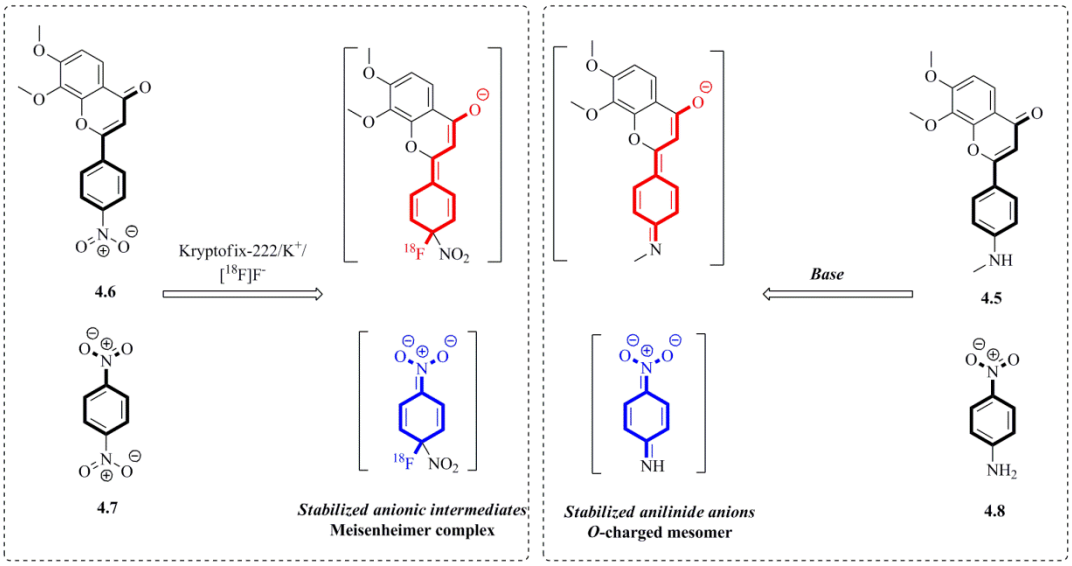

Figure 4.7. Comparison between the structures of the stabilized anilinide anions and the Meisenheimer complexes of 1,4-dinitrobenzene (**4.7**) and compounds **4.5** and **4.6**.

In comparison, radiofluorination of the highly activated 1,4-dinitrobenzene proceeds with 60-80% RCYs under analogous conditions.[16] Although purely qualitative, this comparison suggests that the benzylideneacetone system in compounds **4.5** and **4.6** has similar anion-stabilizing behavior compared to the nitrobenzene moiety. This supports the hypothesis that the pK_a of **4.5** should deviate significantly from the pK_a of unsubstituted aniline and lie closer to that of 4-nitroaniline. In turn, ^{11}C-methylation of **4.5** could likely proceed *via* the formation of a reactive anilinide species generated in trace amount.

4.2.2.3 PET imaging

In vitro stability of the tracer [*N*-methyl-^{11}C]**4.3** was assessed by incubation in rat plasma at 25°C. The radioligand was intact even beyond 30 minutes of incubation, and no significant metabolite (polar or non-polar) were observed (Figure 4.8, C). *In vivo* PET imaging evaluation of [*N*-methyl-^{11}C]**4.3** revealed that the tracer readily crosses the BBB (Figure 4.8, B-D). This result was in stark contrast to the *in vivo* profile of the corresponding 7,8-dihydroxyl radiotracer evaluated previously. Unfortunately, no notable retention was observed and time-activity curves for the whole brain closely matched elimination kinetics.

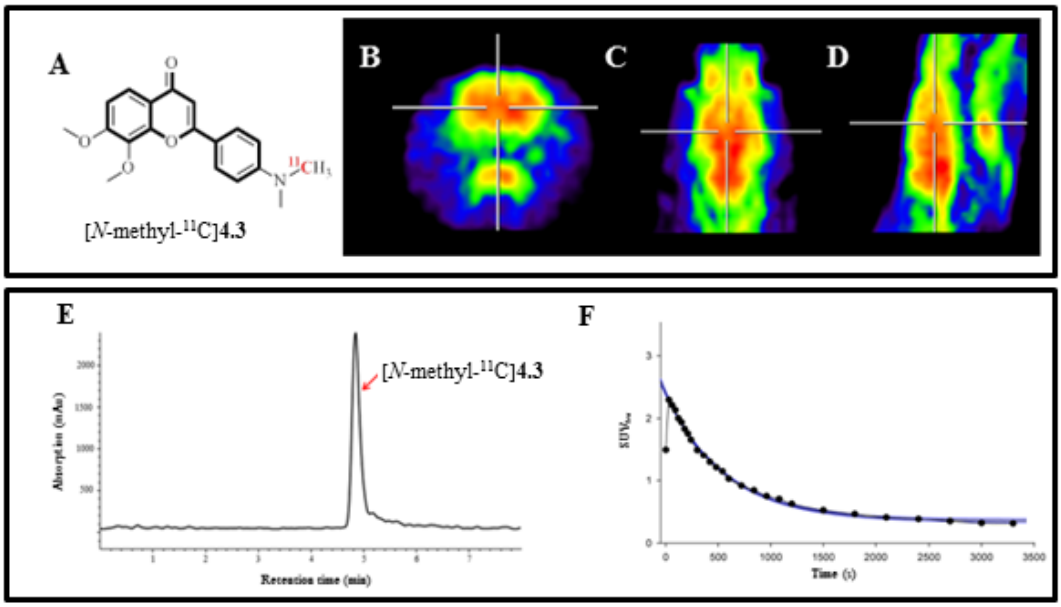

Figure 4.8. PET evaluation of [*N*-methyl-^{11}C]**4.3**. Coronal (B), horizontal (C) and sagittal (D) PET images of rat brain following intravenous injection of [*N*-methyl-^{11}C]**4.3** (summed 1-20 min). (E) The tracer is stable in rat plasma *in vitro* after 30 min. (F) Time-activity curve following intravenous administration of [*N*-methyl-^{11}C]**4.3** in rats (whole brain).

These results support the biological data presented previously, and suggest that the affinity of **4.3** may simply be too low to serve as a PET radioligand. However, modifications along positions 7 and 8 were shown to significantly enhance brain

penetration of the TrkB radioligand. This in turn supports the hypothesis that adequate bioisosterism may generate a brain-penetrating flavone-based TrkB radioligand.

4.2.2.4 Synthesis of the 7,8-methylenedioxy derivative

In order to evaluate whether a decrease in potency of the methylated ligands compared to catechol-bearing compounds was caused by steric factors, or strictly by donor H-bonding properties of its dihydroxyl substituents, the 7,8-methylenedioxy derivative **4.9** was synthesized and evaluated.

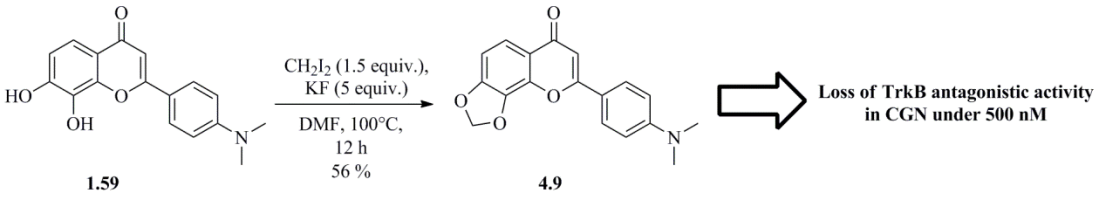

Scheme 4.1. Synthesis of the 7,8-methylenedioxy derivative **4.9**.

Reaction of **1.59** with diiodomethane in the presence of potassium fluoride at 100°C afforded the bridged methylene compound **4.9** in a 56% yield. Thereafter, the inhibitory activity of this ligand was evaluated in CGNs. The introduction of the methylenedioxy fragment resulted in complete loss of activity at the concentrations evaluated (up to 500 nM). This supports the assumption that donor H-bonding at position 7 and/or 8 is a structural feature necessary for the biological activity of functionalized flavone TrkB ligands.

4.3 Conclusion

In order to circumvent the poor *in vivo* properties of the first-generation catechol-bearing TrkB radioligand, the limited potency of methylated analogues, and to rationalize differences in the biological activities of derivatives of the non-cognate small molecule TrkB ligand 7,8-dihydroxyflavone, we conducted a structural investigation of a series of crystallized analogues and an *in vivo* evaluation of the ligand [*N*-methyl-^{11}C]**4.3**.

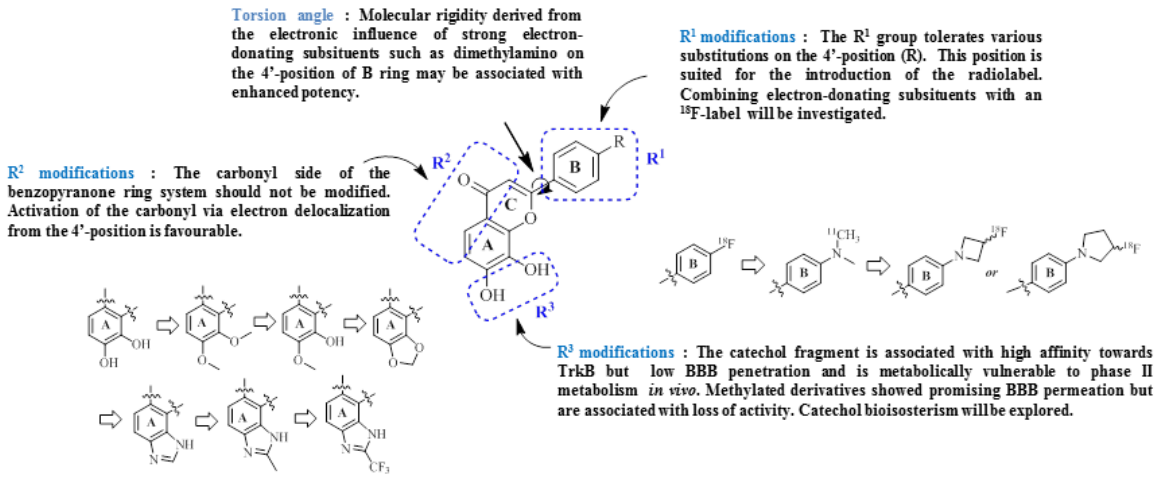

Figure 4.9. Structural requirements for the development of a second generation of TrkB radioligands for PET imaging.

Given our current results, in combination with the work of Liu and colleagues, development of second-generation tracers for PET evaluation of TrkB receptor should benefit from a radiolabel at the 4'-position in combination with a strong electron-donating substituent such as the [^{18}F]-fluoroazetidine and [^{18}F]-fluoropyrrolidine (Figure 4.9). In addition, the synthesis of H-bonding nitrogen-containing catechol bioisosteres – currently in progress – may generate a highly potent, stable, and brain-penetrating class of TrkB radioligands.

4.4 Experimental Section

General Remarks. See experimental section of chapter 3.

Regulatory Notice. See experimental section of chapter 3.

Biological evaluation. See experimental section of chapter 3.

Chemical Synthesis

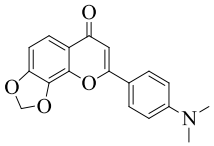

8-(4-(dimethylamino)phenyl)-6*H*-[1,3]dioxolo[4,5-*h*]chromen-6-one (4.9). To a solution of **1.59** (297 mg, 1 mmol) and KF (290 mg, 5 mmol, 5 equiv.) in DMF (10 mL) CH_2I_2 (0.12 mL, 1.5 mmol, 1.5 equiv.). The reaction was stirred at 100°C for 16 h and the DMF was evaporated and the crude mixture was purified vy flash chromatography (3% MeOH/CH_2Cl_2) to afford a red amorphous solid (174 mg, 56 %).

^{1}H NMR (300 MHz, $CDCl_3$) δ 7.77 (m, 3H), 6.90 (d, J = 8.4 Hz, 1H), 6.72 (d, J = 9.0 Hz, 2H), 6.59 (s, 1H), 6.19 (s, 2H), 3.05 (s, 6H) ppm. ^{13}C NMR (75 MHz, $CDCl_3$) δ 177.4, 163.5, 152.4, 151.9, 141.0, 134.6, 127.6, 120.1, 119.8, 117.8, 111.6, 106.6, 103.6, 103.0, 40.1 ppm. HRMS (ESI) calcd for $C_{18}H_{16}NO_4$ $(M+H)^+$ 310.1074, found 310.1081.

Radiochemistry

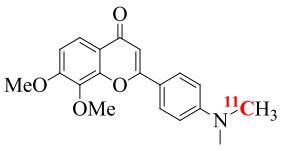

2-(4-[^{11}C](dimethylamino)phenyl)-7,8-dimethoxy-4H-chromen-4-one ([^{11}C]4.3). Procedure for the labeling 4.5. Precursor **4.5** (1.0 mg) was charged in a 1.0 mL conical vial and dissolved in DMSO (300μL). 6.0 μL of NaOH 4.0M was added and [^{11}C]MeOTf was transport by a stream of argon into the reaction vial for 2 minutes and the reaction mixture directly purified by preparative HPLC on a Chromolith® HPLC

RP-18a performance colomn (100X4.6 mm) using a H_2O+0.1% TFA (A)/MeCN +0.1% TFA (B) gradient (t = 0 min: 100% A to t = 10 min A = 0%) at 4.0 mL/min (t_r = 4.92 min) and the tracer was obtained in ~ 30% RCY (n.d.c.). When use for PET animal studies, the collected [^{11}C]**4.11** was passed on a preconditioned (10 mL EtOH followed by 10 mL water) Sep-Pak C18 Light Cartridge and eluted with 1.0 mL EtOH and dilute in sterile normal saline prior to injection.

4.5 References

1. (a) Walle, T. *Free Radical Biol. Med*. **2004**, *36*, 829-837. (b) Manach, C.; Donavan, J. L.; Free Rad. Res. 2004, 38, 771-785. (b) Jager, A. K.; Saaby, L. *Molecule* **2011**, *16*, 1471-1485.
2. Huang, E. J.; Reichardt, L. F. *Annu. Rev. Neurosci.* **2001**, *24*, 677-736.
3. (a) Morris, M. E.; Zhang, S. *Life Sci*. **2006**, *78*, 2116-2130. (b) Bansal, T.; Jaggi, M.; Khar, R. K.; Talegaonkar, S. *J. Pharm. Phram. Sci.* **2009**, *12*, 46-78.
4. For example: Liow, J. S.; McCarron, J. A.; Hong, J.; Musachio, J. L.; Pike, V. W.; Innis, R. B.; Zoghbi, S. S. *Synapse*, **2007**, *61*, 96-105.
5. Liu, X.; Chan, C.-B.; Qi, Q.; Xiao, G.; Luo, H. R.; He, X.; Ye, K. *J. Med. Chem*. **2012**, *55*, 8524-8537.
6. See for example: (a) Hori, A.; Naganuma, K. *Acta Cryst*. **2010**, C66, o256-o259. (b) Neuman, A.; Becquart, J.; Gillier, H.; Leroux, Y.; Queval, P. *Acta Cryst*. **1989**, C45, 1966-1970. (c) Ishiki, H. M.; Aleman, C.; Galembeck, S. E. *Chem. Phys. Lett.* **1998**, *287*, 579-584. (d) Mantas, A.; Deretey, E.; Ferretti, F. H.; Estrada, M. R.; Csiamadia, I. G. *J. Mol. Structure* **2000**, *504*, 171-179.
7. Lau, K. S.; Mantas, A.; Chass, G. A.; Ferretti, F. H.; Estrada, M.; Zamarbide, G.;. Csizmadia, I. G. *Can. J. Chem*. **2002**, *80*, 845–855.
8. Glowka, M. L.; Martynowski, D.; Kozlowska, K. *J. Mol. Structure* **1999**, *474*, 81-89.
9. (a) Walle, T. *Int. J. Mol. Sci.* **2009**, *10*, 5002-5019. (b) Walle, T.; Walle, U. K. *DMD* **2007**, *35*, 1985-1989.
10. (a) Landis-Piwowar, K. R.; Wan, S. B.; Wiegand, R. A.; Kuhn, D. J.; Chan, T. K.; Dou, Q. P. *J. Cell. Physiol*. **2006**, 252-260. (b) Menichincheri, M.; Ballinari, D.; Bargiotto, A. Bonomoni, L.; Ceccarelli, W.; D'Alession, R.; Fretta, A.; Moll, J.; Polucci, P.; Soncini, C.; Tibolla, M.; Trosset, J.-Y.; Vanotti, E. *J. Med. Chem*. **2004**, *47*, 6466-6475.
11. Liu, X.; Chan, C.-B.; Jang, S.-W.; Pradoldej, S.; Hang, J.; He, K.; Phun, L. H.; France, S.; Xiao, G.; Jia, Y.; Luo, H. R.; Ye, K. *J. Med. Chem*. **2010**, *53*, 8274-8286.

12. Liu, X.; Qi, Q.; Xiao, G.; Li, J.; Luo, H. R.; Ye, K. *Pharmacology* **2013**, *91*, 185-200.
13. Ono, M.; Watanabe, R.; Kawashima, H.; Cheng, Y.; Kimura, H.; Watanabe, H.; Haratake, M.; Saji, H.; Nakayama, M. *J. Med. Chem.* **2009**, *52*, 6394–6401.
14. Cai, L.; Xu, R.; Guo, X.; Pike, V. W. *Eur. J. Org. Chem.* **2012**, 1303–1310.
15. Vlasov, V. M.; Os'kina *Russ. J. Org. Chem.* **2002**, *38*, 1705-1718.
16. (a) Hendricks, J. A.; Keliher, E. J.; Marinelli, B.; Reiner, T.; Weissleder, R.; Mazitschek, R. *J. Med. Chem*. **2011**, *54*, 5576-5582. (b) Feliu, A. *J. Label. Compd. Radiopharm*. **1988**, *11*, 1245-1254.

Chapitre 5

Conclusion générale

Le système TrkB/BDNF représente une cible thérapeutique et d'imagerie prometteuses pour une multitude de maladies neurodégénératives de même que pour différents cancers neuroendocriniens. Le développement d'une toute première génération de radioligands du récepteur TrkB marqués de radionucléides à courtes vies, fluor-18 ($t_{1/2}$ = 110 min) et carbone-11 ($t_{1/2}$ = 20.4 min), pour l'imagerie TEP dérivée du ligand de haute affinité 7,8-dihydroxyflavone (K_d = 320 nM) récemment identifié à été mise de l'avant et détaillé.

Une investigation radiosynthétique détaillée a ensuite permis d'obtenir deux radiotraceurs TEP de haute affinité pour TrkB, l'un marqué au fluor-18, l'autre au carbone-11. En particulier, cette étude à mise en lumière une réaction de ^{18}F-radiofluorination nucléophile aromatique d'un système benzylidèneacétone hautement efficace. Cette approche radiosynthétique pourrait s'avérer potentiellement utile pour la radiosynthèse de futurs radiotraceurs marqués au fluor-18 dérivés de flavonoïdes bioactifs.

L'évaluation *in vitro* par autoradiographie de cette première génération de radiotraceurs a révélée que ces radioligands étaient hautement sélectifs au récepteur visé. Les propriétés en tant que traceurs TEP *in vivo* se sont néanmoins avérées hautement limités, principalement en raison d'une faible perméation de la barrière hémato-encéphalique et d'un métabolisme rapide et significatif associé au pharmacophore catéchol malgré des propriétés physico-chimiques favorables par ailleurs. La synthèse d'un troisième radiotraceur présentant une fonction catéchol méthylée à été analysé. Ce traceur a été démontré traverser la barrière hémato-encéphalique sans pour autant se lier au récepteur TrkB *in vivo*, possiblement en raison d'une trop faible affinité ou d'une cinétique de liaison trop lente (k_{on}). Collectivement, l'étude des radioligands obtenus et analysés jusqu'à présent, de pair avec une étude de relation structure-affinité menée partant de la struture cristalline de dérivés flavones ont permis d'identifier des modifications bioisostériques pouvant potentiellement mener à une seconde génération de radioligands de TrkB aux propriétés *in vivo* favorables pour la TEP.

Annexes 1

***Supporting Information for*:**

Radiosynthesis and Evaluation of ^{18}F- and ^{11}C-Labeled 7,8-Dihydroxyflavones as Tropomyosin-Related Kinase B (TrkB) Receptor Antagonists for Brain Imaging with Positron Emission Tomography

***Supporting Information for*:**

Radiosynthesis and Evaluation of ^{18}F- and ^{11}C-Labeled 7,8-Dihydroxyflavones as Tropomyosin-Related Kinase B (TrkB) Receptor Antagonists for Brain Imaging with Positron Emission Tomography

Bernard-Gauthier, Vadim[1,2]; Gaub, Perrine[3]; Boudjemeline, Mehdi[1]; Rosa-Neto, Pedro[4]; Barker, Philip A.[3]; Thiel, Alexander[5] and Schirrmacher, Ralf[1,2]*

1. Département de Chimie, Université de Montréal, P.O. Box 6128, Station Downtown, QC, Canada H3C 3J7
2. McConnell Brain Imaging Centre, Montreal Neurological Institute, McGill University, 3801 University Street, Montreal, QC, Canada, H3A 2B4,
3. Department of Neurology and Neurosurgery, Montreal Neurological Institute, McGill University, 3801 University St., Montreal, QC, Canada, H3A 2B4
4. Translational Neuroimaging Laboratory, McGill Centre for studies in Aging, Douglas Mental Health University Institute, Canada
5. Department of Neurology and Neurosurgery, McGill University, Jewish General Hospital, 3755 Cote St. Catherine Rd., Montreal, QC, Canada, H2T 1E2

* Corresponding author:

Prof. R. Schirrmacher.

Contents.

1. Biological evaluation: supplementary figure.

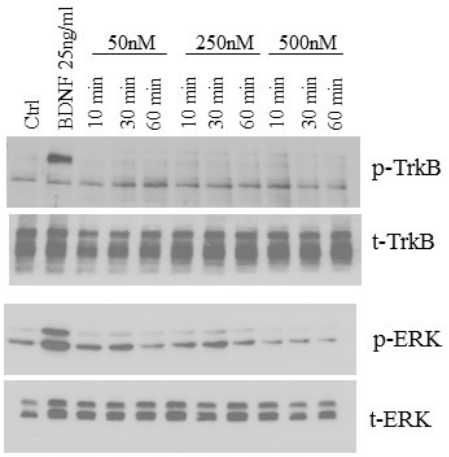

Figure S1. Immunoblotting experiments demonstrate that 7,8-DMF derivatives do not induce TrkB tyrosine phosphorylation in CGN upon 10 min, 30 min or 60 min treatement. Here, compound **15**.

1. Selected RadioHPLC chromatograms from the radiosynthesis of [^{18}F]**10b**, [^{11}C]**8c** and [^{11}C]**10c** (see Experimental Section for the chromatographic conditions)

Isolation of [^{18}F]**10b**

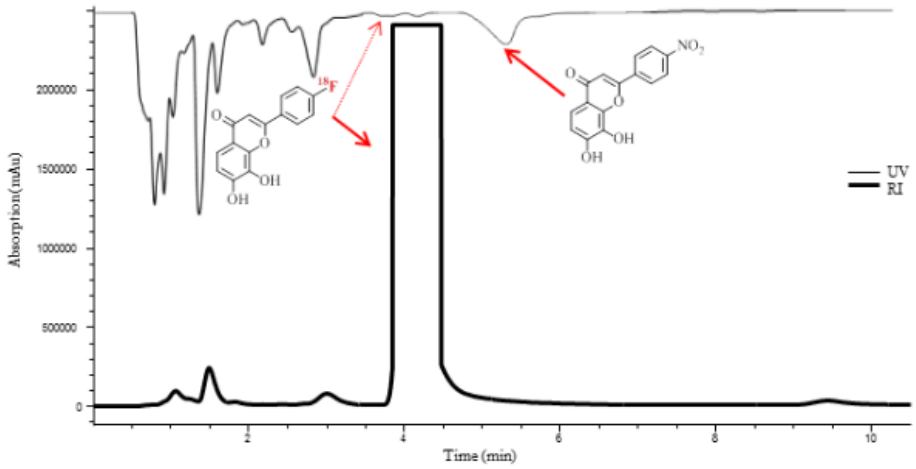

Isolation of [^{11}C]**10c**

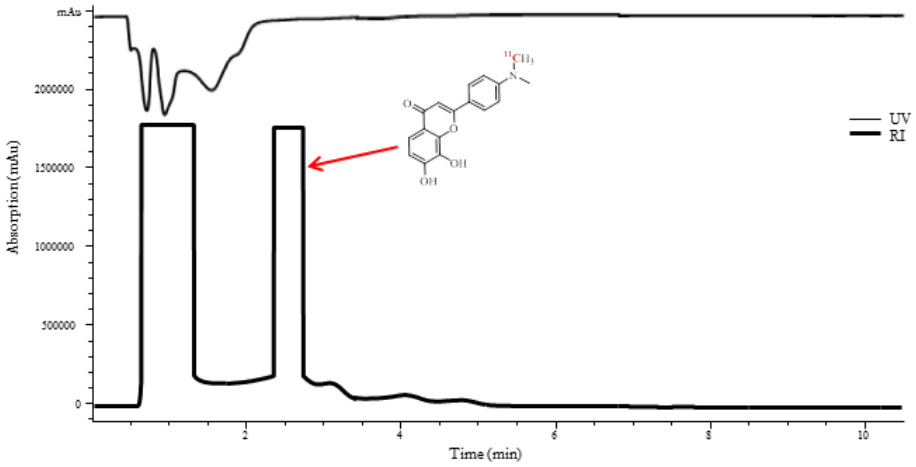

Université de Montréal

CRYSTAL AND MOLECULAR STRUCTURE OF

C19 H21 N O4 COMPOUND (INSNE1)

Equipe Vadim

Montreal Neurological Institute and Hospital

3801 University Street, Montreal, Quebec, Canada H3A 2B4

Structure solved and refined in the laboratory of X-ray diffraction Université de Montréal by Michel Simard.

Table 1. Crystal data and structure refinement for C19 H21 N O4.

Identification code	INSNE1
Empirical formula	C19 H21 N O4
Formula weight	327.37
Temperature	150K
Wavelength	1.54178 Å
Crystal system	Monoclinic
Space group	P21/c
Unit cell dimensions	a = 13.7459(6) Å α = 90°
	b = 9.5631(4) Å β = 99.905(2)°
	c = 12.5445(5) Å γ = 90°
Volume	1624.44(12)Å^3
Z	4
Density (calculated)	1.339 g/cm^3
Absorption coefficient	0.766 mm^{-1}
F(000)	696
Crystal size	0.15 x 0.08 x 0.02 mm
Theta range for data collection	3.26 to 69.88°
Index ranges	$-16 \leq h \leq 16$, $-11 \leq k \leq 9$, $-15 \leq \ell \leq 15$
Reflections collected	44380
Independent reflections	3071 [R_{int} = 0.041]
Absorption correction	Semi-empirical from equivalents
Max. and min. transmission	0.9848 and 0.8535
Refinement method	Full-matrix least-squares on F^2
Data / restraints / parameters	3071 / 0 / 225
Goodness-of-fit on F^2	1.037

Final R indices [I>2sigma(I)]	R_1 = 0.0403, wR_2 = 0.1133
R indices (all data)	R_1 = 0.0416, wR_2 = 0.1155
Extinction coefficient	0.0092(9)
Largest diff. peak and hole	0.206 and -0.144 e/Å^3

Table 2. Atomic coordinates (x 10^4) and equivalent isotropic displacement parameters (Å^2 x 10^3) for C19 H21 N O4.

U_{eq} is defined as one third of the trace of the orthogonalized Uij tensor.

	x	y	z	U_{eq}
O(1)	6392(1)	654(1)	5371(1)	57(1)
O(2)	7799(1)	921(1)	6911(1)	55(1)
O(3)	9786(1)	1193(1)	7586(1)	52(1)
O(4)	10974(1)	1767(1)	6180(1)	52(1)
N	3086(1)	1134(1)	-898(1)	55(1)
C(1)	6895(1)	1104(1)	4698(1)	50(1)
C(2)	6438(1)	1266(1)	3566(1)	51(1)
C(3)	5557(1)	668(1)	3190(1)	52(1)
C(4)	4975(1)	772(1)	2117(1)	50(1)
C(5)	4135(1)	-66(1)	1839(1)	52(1)
C(6)	3527(1)	13(1)	850(1)	53(1)
C(7)	3717(1)	988(1)	68(1)	49(1)
C(8)	4568(1)	1831(1)	334(1)	51(1)
C(9)	5176(1)	1708(1)	1320(1)	50(1)
C(10)	7947(1)	1423(1)	5055(1)	48(1)
C(11)	8366(1)	1234(1)	6161(1)	47(1)
C(12)	9381(1)	1355(1)	6510(1)	47(1)
C(13)	9994(1)	1708(1)	5772(1)	47(1)
C(14)	9586(1)	1982(1)	4694(1)	51(1)
C(15)	8584(1)	1824(1)	4349(1)	50(1)
C(16)	9729(1)	-198(1)	7989(1)	62(1)
C(17)	11622(1)	2165(2)	5454(1)	57(1)
C(18)	3264(1)	2186(2)	-1677(1)	61(1)
C(19)	2356(1)	65(2)	-1266(1)	60(1)

Table 3. Hydrogen coordinates (x 10^4) and isotropic displacement parameters ($Å^2$ x 10^3) for C19 H21 N O4.

	x	y	z	U_{eq}
H(2)	7140(14)	720(20)	6483(15)	83
H(2A)	6763	1796	3090	61
H(3)	5285	110	3692	62
H(5)	3979	-717	2356	63
H(6)	2974	-594	692	63
H(8)	4722	2492	-177	61
H(9)	5750	2276	1469	60
H(14)	9998	2277	4201	61
H(15)	8317	1993	3610	61
H(16A)	9038	-499	7878	93
H(16B)	10003	-218	8763	93
H(16C)	10108	-831	7601	93
H(17A)	11530	1530	4831	86
H(17B)	12308	2115	5829	86
H(17C)	11471	3124	5203	86
H(18A)	3436	3075	-1303	92
H(18B)	2667	2310	-2221	92
H(18C)	3810	1884	-2033	92
H(19A)	2690	-828	-1332	91
H(19B)	1979	332	-1971	91
H(19C)	1907	-31	-742	91

Table 4. Anisotropic parameters ($Å^2$ x 10^3) for C19 H21 N O4.

The anisotropic displacement factor exponent takes the form:

$$-2\pi^2 [h^2 a^{*2} U_{11} + ... + 2 h k a^* b^* U_{12}]$$

	U11	U22	U33	U23	U13	U12
O(1)	56(1)	66(1)	50(1)	3(1)	11(1)	1(1)
O(2)	57(1)	65(1)	45(1)	2(1)	14(1)	-3(1)
O(3)	64(1)	51(1)	40(1)	2(1)	6(1)	-8(1)
O(4)	53(1)	56(1)	48(1)	1(1)	8(1)	-7(1)
N	55(1)	58(1)	50(1)	2(1)	4(1)	-2(1)
C(1)	57(1)	46(1)	48(1)	0(1)	11(1)	5(1)
C(2)	55(1)	50(1)	47(1)	1(1)	8(1)	4(1)
C(3)	56(1)	48(1)	51(1)	1(1)	10(1)	4(1)
C(4)	52(1)	48(1)	49(1)	-1(1)	10(1)	3(1)
C(5)	56(1)	49(1)	52(1)	3(1)	12(1)	-1(1)
C(6)	51(1)	52(1)	55(1)	0(1)	9(1)	-3(1)
C(7)	50(1)	49(1)	48(1)	-2(1)	9(1)	4(1)
C(8)	54(1)	48(1)	50(1)	2(1)	11(1)	-1(1)
C(9)	50(1)	49(1)	52(1)	-1(1)	8(1)	-2(1)
C(10)	55(1)	44(1)	44(1)	0(1)	8(1)	2(1)
C(11)	57(1)	43(1)	43(1)	0(1)	12(1)	0(1)
C(12)	59(1)	42(1)	40(1)	-1(1)	7(1)	-2(1)
C(13)	54(1)	40(1)	47(1)	-1(1)	9(1)	-2(1)
C(14)	60(1)	48(1)	44(1)	2(1)	12(1)	-2(1)
C(15)	59(1)	49(1)	43(1)	2(1)	8(1)	2(1)

C(16)	73(1)	55(1)	54(1)	11(1)	0(1)	-8(1)
C(17)	57(1)	63(1)	54(1)	0(1)	16(1)	-7(1)
C(18)	70(1)	60(1)	51(1)	4(1)	5(1)	1(1)
C(19)	58(1)	67(1)	55(1)	-7(1)	5(1)	-5(1)

Table 5. Bond lengths [Å] and angles [°] for C19 H21 N O4

O(1)-C(1)	1.2559(15)	O(1)-C(1)-C(2)	119.73(11)
O(2)-C(11)	1.3536(14)	O(1)-C(1)-C(10)	119.54(11)
O(3)-C(12)	1.3775(13)	C(2)-C(1)-C(10)	120.71(11)
O(3)-C(16)	1.4300(15)	C(3)-C(2)-C(1)	120.34(12)
O(4)-C(13)	1.3581(14)	C(2)-C(3)-C(4)	128.00(12)
O(4)-C(17)	1.4308(14)	C(5)-C(4)-C(9)	116.24(11)
N-C(7)	1.3707(15)	C(5)-C(4)-C(3)	119.56(11)
N-C(19)	1.4507(16)	C(9)-C(4)-C(3)	124.16(11)
N-C(18)	1.4527(17)	C(6)-C(5)-C(4)	122.77(11)
C(1)-C(2)	1.4597(16)	C(5)-C(6)-C(7)	120.54(11)
C(1)-C(10)	1.4694(18)	N-C(7)-C(6)	121.20(11)
C(2)-C(3)	1.3493(18)	N-C(7)-C(8)	121.51(11)
C(3)-C(4)	1.4455(16)	C(6)-C(7)-C(8)	117.27(11)
C(4)-C(5)	1.3999(17)	C(9)-C(8)-C(7)	120.96(11)
C(4)-C(9)	1.4040(17)	C(8)-C(9)-C(4)	122.16(11)
C(5)-C(6)	1.3738(17)	C(15)-C(10)-C(11)	117.38(11)
C(6)-C(7)	1.4095(17)	C(15)-C(10)-C(1)	123.56(11)
C(7)-C(8)	1.4129(17)	C(11)-C(10)-C(1)	118.94(11)
C(8)-C(9)	1.3737(16)	O(2)-C(11)-C(12)	117.68(10)
C(10)-C(15)	1.4025(17)	O(2)-C(11)-C(10)	121.50(11)
C(10)-C(11)	1.4188(16)	C(12)-C(11)-C(10)	120.82(11)
C(11)-C(12)	1.3939(17)	O(3)-C(12)-C(11)	120.82(10)
C(12)-C(13)	1.3954(16)	O(3)-C(12)-C(13)	119.24(10)
C(13)-C(14)	1.3968(16)	C(11)-C(12)-C(13)	119.87(10)
C(14)-C(15)	1.3796(17)	O(4)-C(13)-C(12)	115.69(10)
		O(4)-C(13)-C(14)	124.29(11)
C(12)-O(3)-C(16)	114.45(9)	C(12)-C(13)-C(14)	120.02(11)
C(13)-O(4)-C(17)	117.18(9)	C(15)-C(14)-C(13)	119.71(11)
C(7)-N-C(19)	120.45(10)	C(14)-C(15)-C(10)	122.03(11)
C(7)-N-C(18)	120.74(10)		
C(19)-N-C(18)	117.50(10)		

Table 6. Torsion angles [°] for C19 H21 N O4.

O(1)-C(1)-C(2)-C(3)	-14.23(18)
C(10)-C(1)-C(2)-C(3)	164.02(11)
C(1)-C(2)-C(3)-C(4)	176.71(11)
C(2)-C(3)-C(4)-C(5)	172.05(12)
C(2)-C(3)-C(4)-C(9)	-10.2(2)
C(9)-C(4)-C(5)-C(6)	-0.44(18)
C(3)-C(4)-C(5)-C(6)	177.51(11)
C(4)-C(5)-C(6)-C(7)	-1.57(19)
C(19)-N-C(7)-C(6)	-16.25(17)
C(18)-N-C(7)-C(6)	177.14(12)
C(19)-N-C(7)-C(8)	165.48(11)
C(18)-N-C(7)-C(8)	-1.13(18)
C(5)-C(6)-C(7)-N	-176.24(11)
C(5)-C(6)-C(7)-C(8)	2.10(17)
N-C(7)-C(8)-C(9)	177.66(11)
C(6)-C(7)-C(8)-C(9)	-0.67(17)
C(7)-C(8)-C(9)-C(4)	-1.37(18)
C(5)-C(4)-C(9)-C(8)	1.91(18)
C(3)-C(4)-C(9)-C(8)	-175.93(11)
O(1)-C(1)-C(10)-C(15)	174.86(11)
C(2)-C(1)-C(10)-C(15)	-3.40(18)
O(1)-C(1)-C(10)-C(11)	-0.95(17)
C(2)-C(1)-C(10)-C(11)	-179.20(10)
C(15)-C(10)-C(11)-O(2)	176.36(11)
C(1)-C(10)-C(11)-O(2)	-7.58(17)
C(15)-C(10)-C(11)-C(12)	-4.09(17)
C(1)-C(10)-C(11)-C(12)	171.98(10)
C(16)-O(3)-C(12)-C(11)	68.15(14)
C(16)-O(3)-C(12)-C(13)	-114.76(12)
O(2)-C(11)-C(12)-O(3)	-1.43(16)
C(10)-C(11)-C(12)-O(3)	179.00(10)
O(2)-C(11)-C(12)-C(13)	-178.50(10)
C(10)-C(11)-C(12)-C(13)	1.93(17)
C(17)-O(4)-C(13)-C(12)	-178.24(10)
C(17)-O(4)-C(13)-C(14)	1.33(16)
O(3)-C(12)-C(13)-O(4)	4.51(15)
C(11)-C(12)-C(13)-O(4)	-178.37(10)
O(3)-C(12)-C(13)-C(14)	-175.08(10)
C(11)-C(12)-C(13)-C(14)	2.04(17)
O(4)-C(13)-C(14)-C(15)	176.72(11)
C(12)-C(13)-C(14)-C(15)	-3.73(17)
C(13)-C(14)-C(15)-C(10)	1.45(18)
C(11)-C(10)-C(15)-C(14)	2.40(18)
C(1)-C(10)-C(15)-C(14)	-173.46(11)

Table 7. Bond lengths [Å] and angles [°] related to the hydrogen bonding for C19 H21 N O4.

D-H	..A	d(D-H)	d(H..A)	d(D..A)	<DHA
O(2)-H(2)	O(1)	0.989(19)	1.585(19)	2.5007(12)	151.8(17)

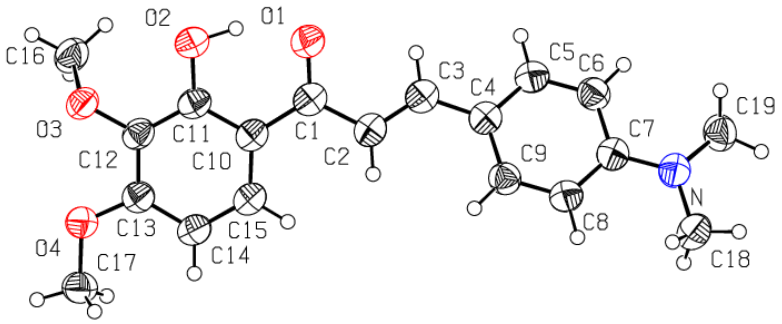

ORTEP view of the C19 H21 N O4 compound with the numbering scheme adopted. Ellipsoids drawn at 30% probability level. Hydrogen atoms are represented by sphere of arbitrary size.

REFERENCES

SAINT (2006) Release 7.34A; Integration Software for Single Crystal Data. Bruker AXS Inc., Madison, WI 53719-1173.

Sheldrick, G.M. (2008). SADABS, Bruker Area Detector Absorption Corrections. Bruker AXS Inc., Madison, WI 53719-1173.

Sheldrick, G.M. (2008). Acta Cryst. A64, 112-122.

SHELXTL (2001) version 6.12; Bruker Analytical X-ray Systems Inc., Madison, WI 53719-1173.

APEX2 (2009) ; Bruker Molecular Analysis Research Tool. Bruker AXS Inc., Madison, WI 53719-1173.

Spek, A.L. (2008). PLATON, A Multipurpose Crystallographic Tool, Utrecht University, Utrecht, The Netherlands.

Maris, T. (2004). UdMX, University of Montréal, Montréal, QC, Canada.

XPREP (2008) Version 2008/2; X-ray data Preparation and Reciprocal space Exploration Program. Bruker

Université de Montréal

CRYSTAL AND MOLECULAR STRUCTURE OF

C17 H13 F O4 COMPOUND (INSNE2)

Equipe Vadim

Montreal Neurological Institute and Hospital

3801 University Street, Montreal, Quebec, Canada H3A 2B4

Structure solved and refined in the laboratory of X-ray diffraction Université de Montréal by Michel Simard.

Table 1. Crystal data and structure refinement for C17 H13 F O4.

Identification code	INSNE2
Empirical formula	C17 H13 F O4
Formula weight	300.27
Temperature	100K
Wavelength	1.54178 Å
Crystal system	Monoclinic
Space group	P21/n
Unit cell dimensions	a = 3.9481(2) Å α = 90° b = 25.6634(11) Å β = 95.989(3)° c = 13.3689(6) Å γ = 90°
Volume	1347.17(11)Å^3
Z	4
Density (calculated)	1.480 g/cm^3
Absorption coefficient	0.965 mm^{-1}
F(000)	624
Crystal size	0.30 x 0.02 x 0.01 mm
Theta range for data collection	3.44 to 70.77°
Index ranges	$-3 \leq h \leq 4$, $-31 \leq k \leq 31$, $-16 \leq \ell \leq 16$
Reflections collected	25275
Independent reflections	2518 [R_{int} = 0.031]
Absorption correction	Semi-empirical from equivalents
Max. and min. transmission	0.9904 and 0.8319
Refinement method	Full-matrix least-squares on F^2
Data / restraints / parameters	2518 / 0 / 201
Goodness-of-fit on F^2	1.051
Final R indices [I>2sigma(I)]	R_1 = 0.0355, wR_2 = 0.0887
R indices (all data)	R_1 = 0.0416, wR_2 = 0.0932
Largest diff. peak and hole	0.221 and -0.173 e/Å^3

Table 2. Atomic coordinates (x 10^4) and equivalent isotropic displacement parameters ($Å^2$ x 10^3) for C17 H13 F O4.

U_{eq} is defined as one third of the trace of the orthogonalized Uij tensor.

	x	y	z	U_{eq}
F	-4616(3)	624(1)	3898(1)	31(1)
O(1)	7286(3)	2800(1)	7994(1)	25(1)
O(2)	3878(3)	1294(1)	7854(1)	16(1)
O(3)	4945(3)	619(1)	9383(1)	17(1)
O(4)	8828(3)	872(1)	11067(1)	19(1)
C(1)	6264(4)	2344(1)	7964(1)	18(1)
C(2)	4074(4)	2135(1)	7122(1)	18(1)
C(3)	3035(4)	1633(1)	7082(1)	16(1)
C(4)	5871(3)	1464(1)	8692(1)	15(1)
C(5)	6474(3)	1099(1)	9460(1)	15(1)
C(6)	8445(4)	1243(1)	10342(1)	16(1)
C(7)	9844(4)	1748(1)	10441(1)	17(1)
C(8)	9187(4)	2100(1)	9665(1)	18(1)
C(9)	7160(4)	1970(1)	8778(1)	16(1)
C(10)	951(4)	1374(1)	6248(1)	16(1)
C(11)	-181(4)	1644(1)	5366(1)	19(1)
C(12)	-2084(4)	1397(1)	4574(1)	22(1)
C(13)	-2796(4)	875(1)	4674(1)	21(1)
C(14)	-1751(4)	593(1)	5531(1)	22(1)
C(15)	137(4)	846(1)	6319(1)	20(1)
C(16)	6696(4)	239(1)	8838(1)	23(1)
C(17)	10802(4)	1000(1)	11997(1)	23(1)

Table 3. Hydrogen coordinates (x 10^4) and isotropic displacement parameters ($Å^2$ x 10^3) for C17 H13 F O4.

	x	y	z	U_{eq}
H(2)	3341	2360	6577	22
H(7)	11228	1844	11036	21
H(8)	10135	2440	9735	21
H(11)	364	2002	5309	23
H(12)	-2874	1582	3980	26
H(14)	-2310	235	5579	26
H(15)	885	659	6914	23
H(16A)	6590	342	8129	35
H(16B)	5611	-102	8889	35
H(16C)	9082	218	9123	35
H(17A)	13170	1064	11873	34
H(17B)	10717	710	12470	34
H(17C)	9868	1314	12282	34

Table 4. Anisotropic parameters ($Å^2$ x 10^3) for C17 H13 F O4.

The anisotropic displacement factor exponent takes the form:

$$-2\pi^2 [h^2 a^{*2} U_{11} + ... + 2 h k a^* b^* U_{12}]$$

	U11	U22	U33	U23	U13	U12
F	36(1)	34(1)	19(1)	-2(1)	-8(1)	-7(1)
O(1)	34(1)	14(1)	26(1)	2(1)	0(1)	-3(1)
O(2)	20(1)	14(1)	13(1)	0(1)	0(1)	-1(1)
O(3)	22(1)	13(1)	17(1)	-2(1)	3(1)	-3(1)
O(4)	25(1)	17(1)	14(1)	1(1)	-2(1)	0(1)
C(1)	22(1)	15(1)	19(1)	0(1)	5(1)	1(1)
C(2)	24(1)	16(1)	16(1)	3(1)	3(1)	2(1)
C(3)	16(1)	19(1)	13(1)	2(1)	4(1)	3(1)
C(4)	14(1)	17(1)	13(1)	-2(1)	2(1)	0(1)
C(5)	15(1)	14(1)	16(1)	-2(1)	4(1)	0(1)
C(6)	18(1)	16(1)	15(1)	1(1)	3(1)	3(1)
C(7)	18(1)	18(1)	17(1)	-4(1)	1(1)	1(1)
C(8)	19(1)	14(1)	20(1)	-4(1)	4(1)	-1(1)
C(9)	18(1)	14(1)	17(1)	0(1)	5(1)	2(1)
C(10)	15(1)	19(1)	15(1)	0(1)	3(1)	2(1)
C(11)	21(1)	19(1)	18(1)	2(1)	2(1)	1(1)
C(12)	23(1)	27(1)	15(1)	4(1)	1(1)	3(1)
C(13)	20(1)	28(1)	15(1)	-4(1)	-1(1)	-2(1)
C(14)	24(1)	20(1)	20(1)	0(1)	0(1)	-3(1)
C(15)	23(1)	20(1)	15(1)	3(1)	1(1)	1(1)
C(16)	26(1)	15(1)	29(1)	-4(1)	8(1)	-1(1)
C(17)	26(1)	26(1)	15(1)	0(1)	-3(1)	0(1)

Table 5. Bond lengths [Å] and angles [°] for C17 H13 F O4

F-C(13)	1.3600(17)	C(2)-C(1)-C(9)	114.41(12)
O(1)-C(1)	1.2367(18)	C(3)-C(2)-C(1)	122.47(13)
O(2)-C(3)	1.3639(16)	C(2)-C(3)-O(2)	121.97(13)
O(2)-C(4)	1.3704(16)	C(2)-C(3)-C(10)	127.04(13)
O(3)-C(5)	1.3713(16)	O(2)-C(3)-C(10)	110.99(11)
O(3)-C(16)	1.4376(17)	O(2)-C(4)-C(5)	115.43(12)
O(4)-C(6)	1.3564(17)	O(2)-C(4)-C(9)	122.41(12)
O(4)-C(17)	1.4344(17)	C(5)-C(4)-C(9)	122.14(13)
C(1)-C(2)	1.448(2)	O(3)-C(5)-C(4)	120.59(12)
C(1)-C(9)	1.4662(19)	O(3)-C(5)-C(6)	120.27(12)
C(2)-C(3)	1.352(2)	C(4)-C(5)-C(6)	118.96(12)
C(3)-C(10)	1.4740(19)	O(4)-C(6)-C(5)	115.43(12)
C(4)-C(5)	1.3913(19)	O(4)-C(6)-C(7)	124.44(13)
C(4)-C(9)	1.3969(19)	C(5)-C(6)-C(7)	120.12(13)
C(5)-C(6)	1.3931(19)	C(8)-C(7)-C(6)	119.46(13)
C(6)-C(7)	1.4083(19)	C(7)-C(8)-C(9)	121.70(13)
C(7)-C(8)	1.381(2)	C(4)-C(9)-C(8)	117.60(13)
C(8)-C(9)	1.400(2)	C(4)-C(9)-C(1)	119.34(13)
C(10)-C(15)	1.398(2)	C(8)-C(9)-C(1)	123.03(13)
C(10)-C(11)	1.3989(19)	C(15)-C(10)-C(11)	118.72(13)
C(11)-C(12)	1.386(2)	C(15)-C(10)-C(3)	119.96(12)
C(12)-C(13)	1.379(2)	C(11)-C(10)-C(3)	121.30(13)
C(13)-C(14)	1.380(2)	C(12)-C(11)-C(10)	121.23(14)
C(14)-C(15)	1.387(2)	C(13)-C(12)-C(11)	117.99(13)
		F-C(13)-C(12)	118.79(13)
C(3)-O(2)-C(4)	119.32(11)	F-C(13)-C(14)	118.30(13)
C(5)-O(3)-C(16)	114.60(11)	C(12)-C(13)-C(14)	122.91(14)
C(6)-O(4)-C(17)	117.88(11)	C(13)-C(14)-C(15)	118.37(14)
O(1)-C(1)-C(2)	122.77(13)	C(14)-C(15)-C(10)	120.78(13)
O(1)-C(1)-C(9)	122.82(13)		

Table 6. Torsion angles [°] for C17 H13 F O4.

O(1)-C(1)-C(2)-C(3)	178.31(14)
C(9)-C(1)-C(2)-C(3)	-1.8(2)
C(1)-C(2)-C(3)-O(2)	2.6(2)
C(1)-C(2)-C(3)-C(10)	-176.93(13)
C(4)-O(2)-C(3)-C(2)	-0.80(19)
C(4)-O(2)-C(3)-C(10)	178.80(11)
C(3)-O(2)-C(4)-C(5)	177.17(11)
C(3)-O(2)-C(4)-C(9)	-1.69(19)
C(16)-O(3)-C(5)-C(4)	84.43(16)
C(16)-O(3)-C(5)-C(6)	-100.56(15)
O(2)-C(4)-C(5)-O(3)	-4.16(18)
C(9)-C(4)-C(5)-O(3)	174.69(13)
O(2)-C(4)-C(5)-C(6)	-179.25(12)
C(9)-C(4)-C(5)-C(6)	-0.4(2)
C(17)-O(4)-C(6)-C(5)	-179.32(12)
C(17)-O(4)-C(6)-C(7)	-0.2(2)
O(3)-C(5)-C(6)-O(4)	2.92(19)
C(4)-C(5)-C(6)-O(4)	178.01(11)
O(3)-C(5)-C(6)-C(7)	-176.21(12)
C(4)-C(5)-C(6)-C(7)	-1.1(2)
O(4)-C(6)-C(7)-C(8)	-177.72(13)
C(5)-C(6)-C(7)-C(8)	1.3(2)
C(6)-C(7)-C(8)-C(9)	0.0(2)
O(2)-C(4)-C(9)-C(8)	-179.60(12)
C(5)-C(4)-C(9)-C(8)	1.6(2)
O(2)-C(4)-C(9)-C(1)	2.3(2)
C(5)-C(4)-C(9)-C(1)	-176.47(12)
C(7)-C(8)-C(9)-C(4)	-1.4(2)
C(7)-C(8)-C(9)-C(1)	176.61(13)
O(1)-C(1)-C(9)-C(4)	179.30(14)
C(2)-C(1)-C(9)-C(4)	-0.55(19)
O(1)-C(1)-C(9)-C(8)	1.3(2)
C(2)-C(1)-C(9)-C(8)	-178.53(13)
C(2)-C(3)-C(10)-C(15)	178.96(14)
O(2)-C(3)-C(10)-C(15)	-0.63(18)
C(2)-C(3)-C(10)-C(11)	0.4(2)
O(2)-C(3)-C(10)-C(11)	-179.15(12)
C(15)-C(10)-C(11)-C(12)	0.2(2)
C(3)-C(10)-C(11)-C(12)	178.73(14)
C(10)-C(11)-C(12)-C(13)	-0.8(2)
C(11)-C(12)-C(13)-F	-179.00(14)
C(11)-C(12)-C(13)-C(14)	1.2(2)
F-C(13)-C(14)-C(15)	179.33(13)
C(12)-C(13)-C(14)-C(15)	-0.8(2)
C(13)-C(14)-C(15)-C(10)	0.2(2)
C(11)-C(10)-C(15)-C(14)	0.2(2)
C(3)-C(10)-C(15)-C(14)	-178.40(1

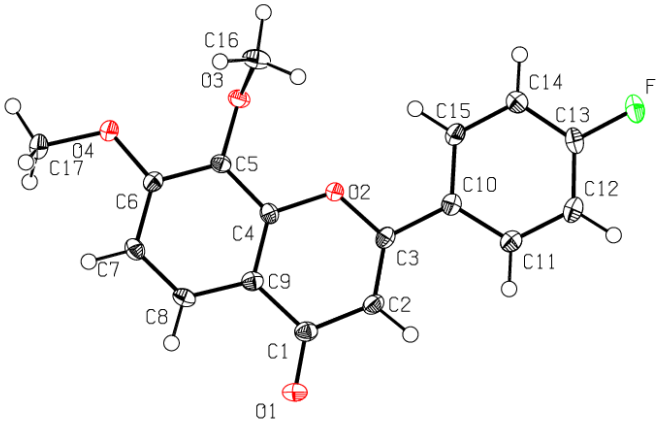

ORTEP view of the C17 H13 F O4 compound with the numbering scheme adopted. Ellipsoids drawn at 30% probability level. Hydrogen atoms are represented by sphere of arbitrary size.

REFERENCES

SAINT (2006) Release 7.34A; Integration Software for Single Crystal Data. Bruker AXS Inc., Madison, WI 53719-1173.

Sheldrick, G.M. (2008). SADABS, Bruker Area Detector Absorption Corrections. Bruker AXS Inc., Madison, WI 53719-1173.

Sheldrick, G.M. (2008). Acta Cryst. A64, 112-122.

SHELXTL (2001) version 6.12; Bruker Analytical X-ray Systems Inc., Madison, WI 53719-1173.

APEX2 (2009) ; Bruker Molecular Analysis Research Tool. Bruker AXS Inc., Madison, WI 53719-1173.

Spek, A.L. (2008). PLATON, A Multipurpose Crystallographic Tool, Utrecht University, Utrecht, The Netherlands.

Maris, T. (2004). UdMX, University of Montréal, Montréal, QC, Canada.

XPREP (2008) Version 2008/2; X-ray data Preparation and Reciprocal space Exploration Program. Bruker AXS Inc., Madison

Université de Montréal

CRYSTAL AND MOLECULAR STRUCTURE OF

C17 H14 O4 COMPOUND (INSNE7)

Equipe Schirrmacher

Montreal Neurological Institute and Hospital

3801 University Street, Montreal, Quebec, Canada H3A 2B4

Structure solved and refined in the laboratory of X-ray diffraction
Université de Montréal by Michel Simard.

Table 1. Crystal data and structure refinement for C17 H14 O4.

Identification code	INSNE7
Empirical formula	C17 H14 O4
Formula weight	282.28
Temperature	100K
Wavelength	1.54178 Å
Crystal system	Monoclinic
Space group	$P2_1/n$
Unit cell dimensions	a = 16.1739(11) Å α = 90° b = 4.6759(3) Å β = 93.213(4)° c = 17.8773(12) Å γ = 90°
Volume	1349.89(16)Å^3
Z	4
Density (calculated)	1.389 g/cm^3
Absorption coefficient	0.816 mm^{-1}
F(000)	592
Crystal size	0.20 x 0.02 x 0.01 mm
Theta range for data collection	3.59 to 70.29°
Index ranges	$-19 \leq h \leq 19$, $-5 \leq k \leq 5$, $-21 \leq \ell \leq 21$
Reflections collected	16745
Independent reflections	2539 [R_{int} = 0.038]
Absorption correction	Semi-empirical from equivalents
Max. and min. transmission	0.9919 and 0.7803
Refinement method	Full-matrix least-squares on F^2
Data / restraints / parameters	2539 / 0 / 192
Goodness-of-fit on F^2	1.051
Final R indices [I>2sigma(I)]	R_1 = 0.0493, wR_2 = 0.1339
R indices (all data)	R_1 = 0.0625, wR_2 = 0.1463
Largest diff. peak and hole	0.267 and -0.213 e/Å^3

Table 2. Atomic coordinates (x 10^4) and equivalent isotropic displacement parameters ($Å^2$ x 10^3) for C17 H14 O4.

U_{eq} is defined as one third of the trace of the orthogonalized Uij tensor.

	x	y	z	U_{eq}
O(1)	3690(1)	6453(3)	9084(1)	38(1)
O(2)	4951(1)	10604(3)	7492(1)	30(1)
O(3)	4646(1)	9879(3)	6020(1)	32(1)
O(4)	3571(1)	5882(3)	5495(1)	33(1)
C(1)	4068(1)	7680(4)	8600(1)	32(1)
C(2)	4693(1)	9855(4)	8768(1)	33(1)
C(3)	5109(1)	11159(4)	8237(1)	30(1)
C(4)	4363(1)	8617(4)	7281(1)	29(1)
C(5)	4241(1)	8214(4)	6510(1)	29(1)
C(6)	3660(1)	6162(4)	6251(1)	29(1)
C(7)	3214(1)	4590(4)	6761(1)	31(1)
C(8)	3347(1)	5058(4)	7521(1)	32(1)
C(9)	3921(1)	7094(4)	7795(1)	30(1)
C(10)	5774(1)	13295(4)	8349(1)	32(1)
C(11)	6093(1)	13989(4)	9073(1)	36(1)
C(12)	6731(1)	15962(4)	9170(1)	40(1)
C(13)	7058(1)	17255(4)	8557(1)	39(1)
C(14)	6743(1)	16602(4)	7839(1)	36(1)
C(15)	6106(1)	14628(4)	7736(1)	34(1)
C(16)	5437(1)	8764(5)	5844(1)	40(1)
C(17)	3020(1)	3678(4)	5212(1)	35(1)

Table 3. Hydrogen coordinates (x 10^4) and isotropic displacement parameters ($Å^2$ x 10^3) for C17 H14 O4.

	x	y	z	U_{eq}
H(2)	4812	10376	9276	40
H(7)	2821	3204	6584	37
H(8)	3044	3980	7863	38
H(11)	5871	13107	9497	43
H(12)	6944	16427	9661	48
H(13)	7499	18589	8627	47
H(14)	6963	17507	7418	44
H(15)	5894	14183	7243	40
H(16A)	5807	8752	6297	60
H(16B)	5674	9969	5462	60
H(16C)	5369	6809	5653	60
H(17A)	3209	1822	5411	52
H(17B)	3015	3646	4664	52
H(17C)	2460	4062	5370	52

Table 4. Anisotropic parameters ($Å^2$ x 10^3) for C17 H14 O4.

The anisotropic displacement factor exponent takes the form:

$$-2\pi^2 [h^2 a^{*2} U_{11} + ... + 2 h k a^* b^* U_{12}]$$

	U11	U22	U33	U23	U13	U12
O(1)	39(1)	44(1)	32(1)	4(1)	1(1)	-2(1)
O(2)	29(1)	31(1)	30(1)	1(1)	-4(1)	-1(1)
O(3)	30(1)	35(1)	32(1)	4(1)	-2(1)	0(1)
O(4)	33(1)	34(1)	31(1)	0(1)	-5(1)	-3(1)
C(1)	30(1)	34(1)	32(1)	2(1)	-1(1)	7(1)
C(2)	33(1)	35(1)	30(1)	-1(1)	-3(1)	3(1)
C(3)	30(1)	29(1)	31(1)	-1(1)	-6(1)	7(1)
C(4)	25(1)	27(1)	34(1)	0(1)	-5(1)	5(1)
C(5)	26(1)	30(1)	31(1)	3(1)	-2(1)	4(1)
C(6)	26(1)	29(1)	32(1)	0(1)	-4(1)	5(1)
C(7)	25(1)	30(1)	38(1)	-1(1)	-2(1)	2(1)
C(8)	28(1)	30(1)	36(1)	4(1)	0(1)	4(1)
C(9)	27(1)	30(1)	32(1)	1(1)	-2(1)	7(1)
C(10)	31(1)	29(1)	34(1)	-1(1)	-6(1)	6(1)
C(11)	40(1)	32(1)	35(1)	1(1)	-7(1)	3(1)
C(12)	43(1)	36(1)	39(1)	-4(1)	-14(1)	2(1)
C(13)	36(1)	34(1)	47(1)	-4(1)	-10(1)	-1(1)
C(14)	34(1)	34(1)	40(1)	0(1)	-3(1)	0(1)
C(15)	31(1)	34(1)	35(1)	-2(1)	-6(1)	3(1)
C(16)	32(1)	50(1)	38(1)	6(1)	2(1)	2(1)
C(17)	33(1)	36(1)	34(1)	-2(1)	-7(1)	-1(1)

Table 5. Bond lengths [Å] and **angles [°] for C17 H14 O4**

O(1)-C(1)	1.229(2)	O(1)-C(1)-C(9)	122.78(18)
O(2)-C(4)	1.366(2)	C(2)-C(1)-C(9)	113.84(16)
O(2)-C(3)	1.368(2)	C(3)-C(2)-C(1)	122.91(17)
O(3)-C(5)	1.366(2)	C(2)-C(3)-O(2)	121.95(17)
O(3)-C(16)	1.431(2)	C(2)-C(3)-C(10)	127.15(18)
O(4)-C(6)	1.358(2)	O(2)-C(3)-C(10)	110.90(16)
O(4)-C(17)	1.436(2)	O(2)-C(4)-C(9)	122.73(17)
C(1)-C(2)	1.453(3)	O(2)-C(4)-C(5)	114.97(16)
C(1)-C(9)	1.471(2)	C(9)-C(4)-C(5)	122.29(17)
C(2)-C(3)	1.341(3)	O(3)-C(5)-C(4)	120.66(16)
C(3)-C(10)	1.473(3)	O(3)-C(5)-C(6)	121.01(17)
C(4)-C(9)	1.392(3)	C(4)-C(5)-C(6)	118.25(17)
C(4)-C(5)	1.395(3)	O(4)-C(6)-C(7)	124.53(16)
C(5)-C(6)	1.403(3)	O(4)-C(6)-C(5)	115.20(16)
C(6)-C(7)	1.401(3)	C(7)-C(6)-C(5)	120.26(17)
C(7)-C(8)	1.381(3)	C(8)-C(7)-C(6)	119.95(17)
C(8)-C(9)	1.399(3)	C(7)-C(8)-C(9)	121.08(17)
C(10)-C(15)	1.394(3)	C(4)-C(9)-C(8)	118.15(17)
C(10)-C(11)	1.404(3)	C(4)-C(9)-C(1)	119.36(17)
C(11)-C(12)	1.388(3)	C(8)-C(9)-C(1)	122.49(17)
C(12)-C(13)	1.384(3)	C(15)-C(10)-C(11)	118.96(18)
C(13)-C(14)	1.387(3)	C(15)-C(10)-C(3)	120.43(17)
C(14)-C(15)	1.388(3)	C(11)-C(10)-C(3)	120.61(18)
		C(12)-C(11)-C(10)	120.0(2)
C(4)-O(2)-C(3)	119.15(15)	C(13)-C(12)-C(11)	120.43(19)
C(5)-O(3)-C(16)	113.55(14)	C(12)-C(13)-C(14)	119.94(19)
C(6)-O(4)-C(17)	116.67(14)	C(13)-C(14)-C(15)	120.1(2)
O(1)-C(1)-C(2)	123.38(17)	C(14)-C(15)-C(10)	120.53(17)

Table 6. Torsion angles [°] for C17 H14 O4.

O(1)-C(1)-C(2)-C(3)	179.26(18)
C(9)-C(1)-C(2)-C(3)	-1.4(3)
C(1)-C(2)-C(3)-O(2)	2.5(3)
C(1)-C(2)-C(3)-C(10)	-177.32(16)
C(4)-O(2)-C(3)-C(2)	-1.4(2)
C(4)-O(2)-C(3)-C(10)	178.46(14)
C(3)-O(2)-C(4)-C(9)	-0.8(2)
C(3)-O(2)-C(4)-C(5)	179.52(14)
C(16)-O(3)-C(5)-C(4)	88.8(2)
C(16)-O(3)-C(5)-C(6)	-94.54(19)
O(2)-C(4)-C(5)-O(3)	-4.6(2)
C(9)-C(4)-C(5)-O(3)	175.67(15)
O(2)-C(4)-C(5)-C(6)	178.60(14)
C(9)-C(4)-C(5)-C(6)	-1.1(3)
C(17)-O(4)-C(6)-C(7)	-4.4(2)
C(17)-O(4)-C(6)-C(5)	176.25(15)
O(3)-C(5)-C(6)-O(4)	3.1(2)
C(4)-C(5)-C(6)-O(4)	179.89(15)
O(3)-C(5)-C(6)-C(7)	-176.22(15)
C(4)-C(5)-C(6)-C(7)	0.5(2)
O(4)-C(6)-C(7)-C(8)	-179.39(16)
C(5)-C(6)-C(7)-C(8)	-0.1(3)
C(6)-C(7)-C(8)-C(9)	0.2(3)
O(2)-C(4)-C(9)-C(8)	-178.49(15)
C(5)-C(4)-C(9)-C(8)	1.2(3)
O(2)-C(4)-C(9)-C(1)	1.8(3)
C(5)-C(4)-C(9)-C(1)	-178.53(15)
C(7)-C(8)-C(9)-C(4)	-0.7(3)
C(7)-C(8)-C(9)-C(1)	178.99(16)
O(1)-C(1)-C(9)-C(4)	178.65(17)
C(2)-C(1)-C(9)-C(4)	-0.7(2)
O(1)-C(1)-C(9)-C(8)	-1.1(3)
C(2)-C(1)-C(9)-C(8)	179.59(16)
C(2)-C(3)-C(10)-C(15)	-175.02(18)
O(2)-C(3)-C(10)-C(15)	5.1(2)
C(2)-C(3)-C(10)-C(11)	5.9(3)
O(2)-C(3)-C(10)-C(11)	-173.94(16)
C(15)-C(10)-C(11)-C(12)	-0.4(3)
C(3)-C(10)-C(11)-C(12)	178.71(17)
C(10)-C(11)-C(12)-C(13)	-0.1(3)
C(11)-C(12)-C(13)-C(14)	0.6(3)
C(12)-C(13)-C(14)-C(15)	-0.8(3)
C(13)-C(14)-C(15)-C(10)	0.3(3)
C(11)-C(10)-C(15)-C(14)	0.3(3)
C(3)-C(10)-C(15)-C(14)	-178.82(17)

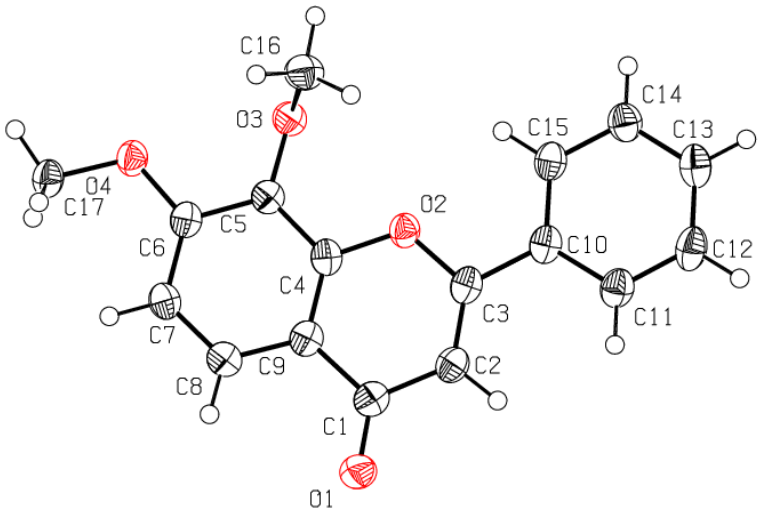

ORTEP view of the C17 H14 O4 compound with the numbering scheme adopted. Ellipsoids drawn at 30% probability level. Hydrogen atoms are represented by sphere of arbitrary size.

REFERENCES

SAINT (2006) Release 7.34A; Integration Software for Single Crystal Data. Bruker AXS Inc., Madison, WI 53719-1173.

Sheldrick, G.M. (2008). SADABS, Bruker Area Detector Absorption Corrections. Bruker AXS Inc., Madison, WI 53719-1173.

Burla, M. C., Caliandro, R., Camalli, M., Carrozzini, B., Cascarano, G. L., De Caro, L., Giacovazzo, C., Polidori, G. & Spagna, R. (2005). J. Appl. Cryst. 38, 381-388.

Sheldrick, G.M. (2008). Acta Cryst. A64, 112-122.

SHELXTL (2001) version 6.12; Bruker Analytical X-ray Systems Inc., Madison, WI 53719-1173.

APEX2 (2009) ; Bruker Molecular Analysis Research Tool. Bruker AXS Inc., Madison, WI 53719-1173.

Spek, A.L. (2008). PLATON, A Multipurpose Crystallographic Tool, Utrecht University, Utrecht, The Netherlands.

Maris, T. (2004). UdMX, University of Montréal, Montréal, QC, Canada.

XPREP (2008) Version 2008/2; X-ray data Preparation and Reciprocal space Exploration Program. Bruker

Annexes 2

Crystallographic data, Chapter 4

Université de Montréal

CRYSTAL AND MOLECULAR STRUCTURE OF

C19 H19 N O4 COMPOUND (INSNE8)

Equipe Schirrmacher

Montreal Neurological Institute and Hospital

3801 University Street, Montreal, Quebec, Canada H3A 2B4

Structure solved and refined in the laboratory of X-ray diffraction Université de Montréal by Michel Simard.

Table 1. Crystal data and structure refinement for C19 H19 N O4.

Identification code	INSNE8
Empirical formula	C19 H19 N O4
Formula weight	325.35
Temperature	150K
Wavelength	1.54178 Å
Crystal system	Triclinic
Space group	P-1
Unit cell dimensions	a = 8.1101(3) Å α = 74.717(2)° b = 9.5324(3) Å β = 84.168(2)° c = 10.8097(4) Å γ = 83.019(2)°
Volume	798.04(5)Å^3
Z	2
Density (calculated)	1.354 g/cm^3
Absorption coefficient	0.779 mm^{-1}
F(000)	344
Crystal size	0.15 x 0.07 x 0.05 mm
Theta range for data collection	4.25 to 70.00°
Index ranges	$-9 \leq h \leq 9$, $-11 \leq k \leq 11$, $-13 \leq \ell \leq 12$
Reflections collected	43324
Independent reflections	2986 [R_{int} = 0.043]
Absorption correction	Semi-empirical from equivalents
Max. and min. transmission	0.9618 and 0.7694
Refinement method	Full-matrix least-squares on F^2
Data / restraints / parameters	2986 / 0 / 221
Goodness-of-fit on F^2	1.073
Final R indices [I>2sigma(I)]	R_1 = 0.0389, wR_2 = 0.1098

R indices (all data)	R_1 = 0.0401, wR_2 = 0.1113
Largest diff. peak and hole	0.197 and -0.181 e/Å^3

Table 2. Atomic coordinates (x 10^4) and equivalent isotropic displacement parameters ($Å^2$ x 10^3) for C19 H19 N O4.

U_{eq} is defined as one third of the trace of the orthogonalized Uij tensor.

	x	y	z	U_{eq}
O(1)	3295(1)	2000(1)	-551(1)	39(1)
O(2)	4886(1)	2842(1)	2627(1)	28(1)
O(3)	3821(1)	5236(1)	3415(1)	32(1)
O(4)	1944(1)	7475(1)	1916(1)	41(1)
N	9295(1)	-2301(1)	6098(1)	37(1)
C(1)	3833(2)	2275(1)	386(1)	30(1)
C(2)	4875(1)	1238(1)	1268(1)	30(1)
C(3)	5364(1)	1536(1)	2332(1)	26(1)
C(4)	3897(1)	3890(1)	1832(1)	26(1)
C(5)	3408(1)	5159(1)	2238(1)	28(1)
C(6)	2410(2)	6277(1)	1460(1)	31(1)
C(7)	1926(2)	6108(1)	303(1)	35(1)
C(8)	2400(2)	4828(1)	-58(1)	32(1)
C(9)	3388(1)	3690(1)	699(1)	28(1)
C(10)	6394(1)	561(1)	3293(1)	27(1)
C(11)	7154(1)	-781(1)	3120(1)	30(1)
C(12)	8112(2)	-1716(1)	4030(1)	32(1)
C(13)	8368(1)	-1361(1)	5182(1)	30(1)
C(14)	7616(1)	-1(1)	5345(1)	29(1)
C(15)	6655(1)	924(1)	4428(1)	28(1)
C(16)	4986(2)	6264(2)	3375(1)	44(1)
C(17)	1040(2)	8689(2)	1094(1)	46(1)
C(18)	10159(2)	-3640(2)	5866(2)	48(1)
C(19)	9644(2)	-1888(2)	7223(1)	40(1)

Table 3. Hydrogen coordinates (x 10^4) and isotropic displacement parameters ($Å^2$ x 10^3) for C19 H19 N O4.

	x	y	z	U_{eq}
H(2)	5234	314	1104	36
H(7)	1269	6878	-234	41
H(8)	2048	4719	-836	39
H(11)	7004	-1051	2356	36
H(12)	8612	-2617	3883	39
H(14)	7777	283	6100	35
H(15)	6157	1829	4568	34
H(16A)	5971	6080	2814	66
H(16B)	5319	6157	4245	66
H(16C)	4467	7258	3040	66
H(17A)	1714	9023	286	69
H(17B)	793	9487	1520	69
H(17C)	-3	8387	912	69
H(18A)	9347	-4256	5730	73
H(18B)	10779	-4163	6612	73
H(18C)	10934	-3406	5101	73
H(19A)	10311	-1052	6968	59
H(19B)	10265	-2712	7792	59
H(19C)	8595	-1617	7678	59

Table 4. Anisotropic parameters ($Å^2$ x 10^3) for C19 H19 N O4.

The anisotropic displacement factor exponent takes the form:

$$-2\pi^2 [h^2 a^{*2} U_{11} + ... + 2 h k a^* b^* U_{12}]$$

	U11	U22	U33	U23	U13	U12
O(1)	56(1)	37(1)	29(1)	-12(1)	-14(1)	-2(1)
O(2)	35(1)	24(1)	24(1)	-6(1)	-7(1)	-2(1)
O(3)	46(1)	30(1)	22(1)	-6(1)	-7(1)	-5(1)
O(4)	55(1)	32(1)	35(1)	-12(1)	-13(1)	10(1)
N	46(1)	30(1)	34(1)	-4(1)	-13(1)	-1(1)
C(1)	36(1)	32(1)	23(1)	-7(1)	-2(1)	-7(1)
C(2)	36(1)	28(1)	26(1)	-8(1)	-4(1)	-3(1)
C(3)	29(1)	25(1)	25(1)	-6(1)	0(1)	-6(1)
C(4)	29(1)	26(1)	22(1)	-2(1)	-3(1)	-4(1)
C(5)	34(1)	29(1)	21(1)	-5(1)	-4(1)	-5(1)
C(6)	37(1)	28(1)	29(1)	-7(1)	-4(1)	0(1)
C(7)	39(1)	34(1)	29(1)	-4(1)	-10(1)	2(1)
C(8)	38(1)	35(1)	24(1)	-6(1)	-8(1)	-4(1)
C(9)	32(1)	29(1)	22(1)	-5(1)	-3(1)	-6(1)
C(10)	28(1)	27(1)	24(1)	-5(1)	-2(1)	-6(1)
C(11)	35(1)	29(1)	28(1)	-9(1)	-5(1)	-6(1)
C(12)	38(1)	26(1)	36(1)	-9(1)	-6(1)	-3(1)
C(13)	32(1)	27(1)	29(1)	-2(1)	-4(1)	-7(1)
C(14)	33(1)	33(1)	24(1)	-7(1)	-3(1)	-5(1)
C(15)	30(1)	28(1)	27(1)	-8(1)	0(1)	-3(1)
C(16)	57(1)	46(1)	33(1)	-10(1)	-11(1)	-16(1)
C(17)	60(1)	34(1)	41(1)	-9(1)	-12(1)	14(1)
C(18)	59(1)	36(1)	49(1)	-8(1)	-19(1)	9(1)
C(19)	44(1)	42(1)	32(1)	-4(1)	-9(1)	-4(1)

Table 5. Bond lengths [Å] and angles [°] for C19 H19 N O4

O(1)-C(1)	1.2423(14)	O(1)-C(1)-C(2)	123.34(11)
O(2)-C(3)	1.3666(13)	O(1)-C(1)-C(9)	121.70(11)
O(2)-C(4)	1.3680(13)	C(2)-C(1)-C(9)	114.92(10)
O(3)-C(5)	1.3705(13)	C(3)-C(2)-C(1)	122.16(11)
O(3)-C(16)	1.4315(15)	C(2)-C(3)-O(2)	121.86(10)
O(4)-C(6)	1.3583(14)	C(2)-C(3)-C(10)	126.62(10)
O(4)-C(17)	1.4323(15)	O(2)-C(3)-C(10)	111.52(9)
N-C(13)	1.3666(15)	O(2)-C(4)-C(5)	115.62(9)
N-C(19)	1.4372(16)	O(2)-C(4)-C(9)	122.19(10)
N-C(18)	1.4481(17)	C(5)-C(4)-C(9)	122.18(10)
C(1)-C(2)	1.4366(16)	O(3)-C(5)-C(4)	119.41(10)
C(1)-C(9)	1.4701(16)	O(3)-C(5)-C(6)	122.14(10)
C(2)-C(3)	1.3608(16)	C(4)-C(5)-C(6)	118.31(10)
C(3)-C(10)	1.4562(16)	O(4)-C(6)-C(5)	115.71(10)
C(4)-C(5)	1.3932(16)	O(4)-C(6)-C(7)	124.14(11)
C(4)-C(9)	1.3970(15)	C(5)-C(6)-C(7)	120.14(11)
C(5)-C(6)	1.3979(16)	C(8)-C(7)-C(6)	120.13(11)
C(6)-C(7)	1.4025(17)	C(7)-C(8)-C(9)	121.15(11)
C(7)-C(8)	1.3760(17)	C(8)-C(9)-C(4)	118.06(11)
C(8)-C(9)	1.3935(16)	C(8)-C(9)-C(1)	122.65(10)
C(10)-C(15)	1.4010(16)	C(4)-C(9)-C(1)	119.21(10)
C(10)-C(11)	1.4013(16)	C(15)-C(10)-C(11)	117.52(10)
C(11)-C(12)	1.3757(16)	C(15)-C(10)-C(3)	121.39(10)
C(12)-C(13)	1.4139(16)	C(11)-C(10)-C(3)	121.09(10)
C(13)-C(14)	1.4109(17)	C(12)-C(11)-C(10)	121.45(11)
C(14)-C(15)	1.3771(16)	C(11)-C(12)-C(13)	121.27(11)
		N-C(13)-C(14)	121.68(11)
C(3)-O(2)-C(4)	119.55(9)	N-C(13)-C(12)	121.29(11)
C(5)-O(3)-C(16)	115.05(9)	C(14)-C(13)-C(12)	117.03(11)
C(6)-O(4)-C(17)	117.06(10)	C(15)-C(14)-C(13)	121.16(10)
C(13)-N-C(19)	120.82(11)	C(14)-C(15)-C(10)	121.57(11)
C(13)-N-C(18)	120.59(11)		
C(19)-N-C(18)	117.94(10)		

Table 6. Torsion angles [°] for C19 H19 N O4.

O(1)-C(1)-C(2)-C(3)	-175.85(11)
C(9)-C(1)-C(2)-C(3)	1.93(16)
C(1)-C(2)-C(3)-O(2)	0.26(17)
C(1)-C(2)-C(3)-C(10)	179.10(10)
C(4)-O(2)-C(3)-C(2)	-0.43(16)
C(4)-O(2)-C(3)-C(10)	-179.43(8)
C(3)-O(2)-C(4)-C(5)	177.14(9)
C(3)-O(2)-C(4)-C(9)	-1.83(16)
C(16)-O(3)-C(5)-C(4)	112.89(12)
C(16)-O(3)-C(5)-C(6)	-71.54(15)
O(2)-C(4)-C(5)-O(3)	-4.92(15)
C(9)-C(4)-C(5)-O(3)	174.05(10)
O(2)-C(4)-C(5)-C(6)	179.34(9)
C(9)-C(4)-C(5)-C(6)	-1.68(17)
C(17)-O(4)-C(6)-C(5)	174.88(11)
C(17)-O(4)-C(6)-C(7)	-6.41(18)
O(3)-C(5)-C(6)-O(4)	3.12(17)
C(4)-C(5)-C(6)-O(4)	178.73(10)
O(3)-C(5)-C(6)-C(7)	-175.65(10)
C(4)-C(5)-C(6)-C(7)	-0.04(18)
O(4)-C(6)-C(7)-C(8)	-177.23(11)
C(5)-C(6)-C(7)-C(8)	1.43(19)
C(6)-C(7)-C(8)-C(9)	-1.15(19)
C(7)-C(8)-C(9)-C(4)	-0.52(18)
C(7)-C(8)-C(9)-C(1)	176.13(11)
O(2)-C(4)-C(9)-C(8)	-179.12(9)
C(5)-C(4)-C(9)-C(8)	1.97(17)
O(2)-C(4)-C(9)-C(1)	4.11(16)
C(5)-C(4)-C(9)-C(1)	-174.80(10)
O(1)-C(1)-C(9)-C(8)	-2.77(18)
C(2)-C(1)-C(9)-C(8)	179.40(10)
O(1)-C(1)-C(9)-C(4)	173.84(11)
C(2)-C(1)-C(9)-C(4)	-3.99(16)
C(2)-C(3)-C(10)-C(15)	-172.33(11)
O(2)-C(3)-C(10)-C(15)	6.61(15)
C(2)-C(3)-C(10)-C(11)	7.26(18)
O(2)-C(3)-C(10)-C(11)	-173.80(9)
C(15)-C(10)-C(11)-C(12)	0.43(17)
C(3)-C(10)-C(11)-C(12)	-179.18(10)
C(10)-C(11)-C(12)-C(13)	0.11(18)
C(19)-N-C(13)-C(14)	-4.72(18)
C(18)-N-C(13)-C(14)	-175.23(12)
C(19)-N-C(13)-C(12)	175.60(11)
C(18)-N-C(13)-C(12)	5.09(18)
C(11)-C(12)-C(13)-N	178.84(10)
C(11)-C(12)-C(13)-C(14)	-0.86(17)
N-C(13)-C(14)-C(15)	-178.60(10)
C(12)-C(13)-C(14)-C(15)	1.10(17)
C(13)-C(14)-C(15)-C(10)	-0.59(17)
C(11)-C(10)-C(15)-C(14)	-0.19(17)
C(3)-C(10)-C(15)-C(14)	179.42(10)

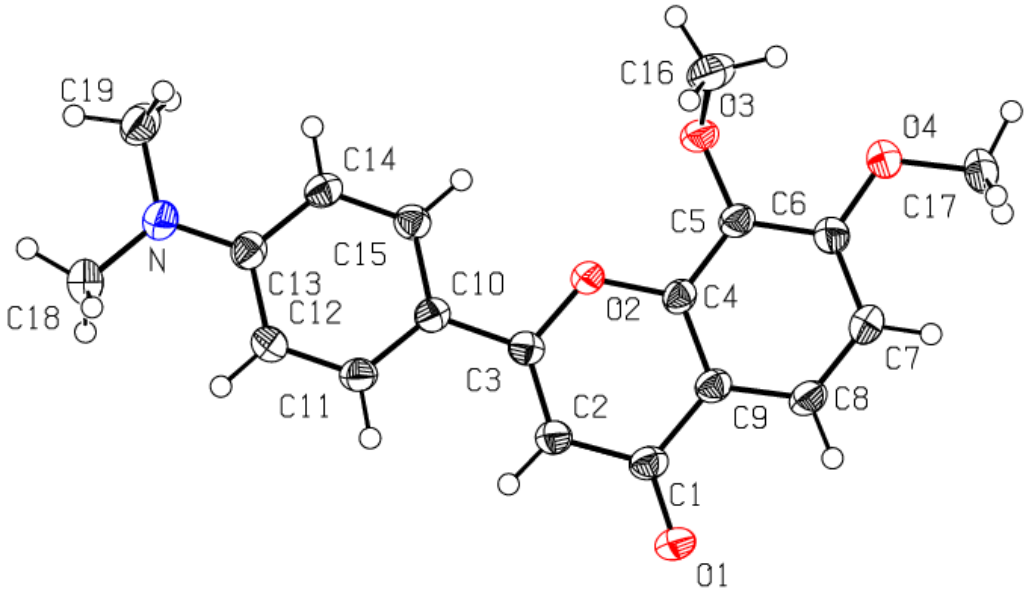

ORTEP view of the C19 H19 N O4 compound with the numbering scheme adopted. Ellipsoids drawn at 30% probability level. Hydrogen atoms are represented by sphere of arbitrary size.

REFERENCES

SAINT (2006) Release 7.34A; Integration Software for Single Crystal Data.
Bruker AXS Inc., Madison, WI 53719-1173.

Sheldrick, G.M. (2008). SADABS, Bruker Area Detector Absorption Corrections.
Bruker AXS Inc., Madison, WI 53719-1173.

Burla, M. C., Caliandro, R., Camalli, M., Carrozzini, B., Cascarano, G. L., De Caro, L., Giacovazzo, C., Polidori, G. & Spagna, R. (2005). J. Appl. Cryst. 38, 381-388.

Sheldrick, G.M. (2008). Acta Cryst. A64, 112-122.

SHELXTL (2001) version 6.12; Bruker Analytical X-ray Systems Inc., Madison, WI 53719-1173.

APEX2 (2009) ; Bruker Molecular Analysis Research Tool.
Bruker AXS Inc., Madison, WI 53719-1173.

Spek, A.L. (2008). PLATON, A Multipurpose Crystallographic Tool, Utrecht University, Utrecht, The Netherlands.

Maris, T. (2004). UdMX, University of Montréal, Montréal, QC, Canada.

XPREP (2008) Version 2008/2; X-ray data Preparation and Reciprocal space
Exploration Program. Bruker AXS Inc., Madison, WI 53719-1173.